11-4-2009

Sensitivity Analysis of Three Assembly Procedures for a Bascule Bridge Fulcrum

Luke Allen Snyder
University of South Florida

Sensitivity Analysis of Three Assembly Procedures for a Bascule Bridge Fulcrum

by

Luke Allen Snyder

A thesis submitted in partial fulfillment
of the requirements for the degree of
Master of Science in Mechanical Engineering
Department of Mechanical Engineering
College of Engineering
University of South Florida

Major Professor: Autar Kaw, Ph.D.
Glen Besterfield, Ph.D.
Muhammad Rahman, Ph.D.

Date of Approval:
November 4, 2009

Keywords: Finite Element Analysis, ANSYS, Design of Experiments, OMCCL, OMSR

DEDICATION

This thesis is dedicated to my wonderful parents, amazing sister, and to the Snyder family in its entirety. In addition, I dedicate this thesis to my advisor Dr. Autar Kaw who carries with him all the inspiration any student will ever need to succeed.

ACKNOWLEDGEMENTS

First and foremost, I would like to thank my parents. There are no finer people on the planet and it is through their sacrifice and generous nature throughout my life, that I was able to attend college and achieve an advanced degree. They inspire me to be a better man, a better person and to always achieve the absolute utmost of what I am capable of.

I would like to thank my advisor, Dr. Autar Kaw. He has been a wonderful influence on my life, both through his admirable and highly astute teaching abilities, as well as through his sense of the world and sense of humor. He is a man wise beyond most, and I am indebted to him for all his financial and academic support.

Additionally, I would like to thank all my friends who helped me along through graduate school. I would also like to specifically thank Sri Harsha Garapati whose friendship and knowledge of virtually all subjects including finite element analysis, proved invaluable in the completion of this work. I would like to thank the research computing department at USF for use of their high performance computing systems. I would like to take this opportunity to humbly thank my committee members Dr. Besterfield and Dr. Rahman for their time and efforts.

TABLE OF CONTENTS

LIST OF TABLES

LIST OF FIGURES

LIST OF EQUATIONS

Sensitivity Analysis of Three Assembly Procedures for a Bascule Bridge Fulcrum

Luke Allen Snyder

ABSTRACT

Many different hub assembly procedures have been utilized over the years in bascule bridge construction. The first assembly procedure (AP1) involves shrink fitting a trunnion component into a hub, followed by the shrink fitting of the entire trunnion-hub (TH) assembly into the girder of the bridge. The second assembly procedure (AP2) involves shrink fitting the hub component first into the girder, then shrink fitting the trunnion component into the hub-girder (HG) assembly. The final assembly procedure uses a warm shrink fitting process whereby induction coils are placed on the girder of the bridge and heat is applied until sufficient thermal expansion of the girder hole allows for insertion of the hub component. All three assembly procedures use a cooling method at some stage of the assembly procedure to contract components to allow the insertion of one part into the next. Occasionally, during these cooling and heating procedures, cracks can develop in the material due to the large thermal shock and subsequent thermal stresses.

Previous works conducted a formal design of experiments analysis on AP1 to determine the overall effect of various factors on the critical design parameters, overall minimum stress ratio (OMSR) and overall minimum critical crack length (OMCCL). This work focuses on conducting a formal design of experiments analysis on AP1, AP2 and AP3 using the same cooling methods and parameters as in previous studies with the addition of the bridge size as a factor in the experiment.

The use of the medium bridge size in AP1 yields the largest OMCCL values of any bridge and the second largest OMSR values. The large bridge size has the largest OMSR values versus all factors for AP1. The OMCCL and OMSR increases for every bridge size with an increase in the alpha ratio for AP1. The smallest bridge showed the largest OMCCL and OMSR values for every cooling method and every alpha ratio for AP2 and AP3. The OMCCL and OMSR decrease for every bridge size with an increase in the alpha ratio for AP2 and AP3.

CHAPTER 1 INTRODUCTION

1.1 Introduction to Problem

The bascule bridge has been an instrumental component to waterways around the world for many years. This bridge design operates by lifting a central section, or leaf, of its span to allow for marine traffic that would not otherwise have been able to clear the bridge height. This central span of the bascule bridge pivots on large bearings which are fit onto what is equivalently a large pin or axle. This axle is commonly referred to as the Trunnion-Hub-Girder (THG) assembly and serves as a fulcrum as the leaf is lifted. The variation in assembly procedures utilized to bring these components together is the subject of this thesis.

The two main types of bascule bridge design are the Scherzer rolling lift bascule bridge and the fixed-trunnion bascule bridge. The central focus of this work will be the fixed-trunnion bascule bridge, which is the most common bascule bridge design in use.

In the fixed-trunnion bascule bridge, the THG assembly supports the weight of the leaf of the bridge as well as a counterweight on the opposite side of the assembly that assists in the lifting of the span. Double-leaf bascule bridges are also fairly common with the most prominent example being the Tower Bridge in London as seen in Figure 1. Bascule bridges are the most popular movable bridge design as they can open and close quickly, and they require a reasonably small amount of energy to activate. This bridge

design is often much cheaper than a raised-span bridge, and in applications where marine traffic is relatively low, they are very efficient and cost effective. Bascule bridges of many different forms are very prominent along the intercoastal waterways of Florida.

The THG assembly serves as a critical component to the fixed-trunnion bascule bridge. Without proper assembly of this component, the entire bridge is in danger of failing. Common assembly procedures utilize shrink fitting procedures to create an

Figure 1 Tower bascule bridge in London, UK [4].

interference fit between components. This interference fit effectively creates a compound cylinder which provides additional strength versus components which are not shrink fit. This additional strength is due to the addition of the contact pressure, or interference stress which is developed when one component expands inside of another. This is one of the primary reasons that shrink fitting procedures are used to assemble the components of the THG assembly.

1.2 Assembly Procedures

The THG assembly consists of three components—the trunnion (inner most component), the hub (middle component), and finally the girder of the bridge itself. There are three main assembly procedures that can be used to assemble the THG assembly. The various steps for each assembly procedure are outlined below.

The first assembly procedure is characterized by the following steps:

1. The trunnion (inner most component) is shrunk by immersion in a bath, such as liquid nitrogen at $-321^{\circ}\mathrm{F}$.
2. The trunnion is inserted into the hub (middle component) and allowed to reheat to the ambient temperature creating an interference fit between the trunnion and the hub (trunnion-hub interface).
3. The entire trunnion-hub assembly is then shrunk by immersion in a bath, such as liquid nitrogen at $-321^{\circ}\mathrm{F}$.
4. The trunnion-hub assembly is inserted into the girder of the bridge and the entire assembly is allowed to reheat to the ambient temperature creating an interference fit between the trunnion-hub assembly and the girder (hub-girder interface).

The essential difference between the first two assembly procedures is the order in which the components are shrink fit and assembled. The final assembly procedure (AP3), utilizes a warm shrink fitting process in the first step that serves as a replacement to the first step of AP2.

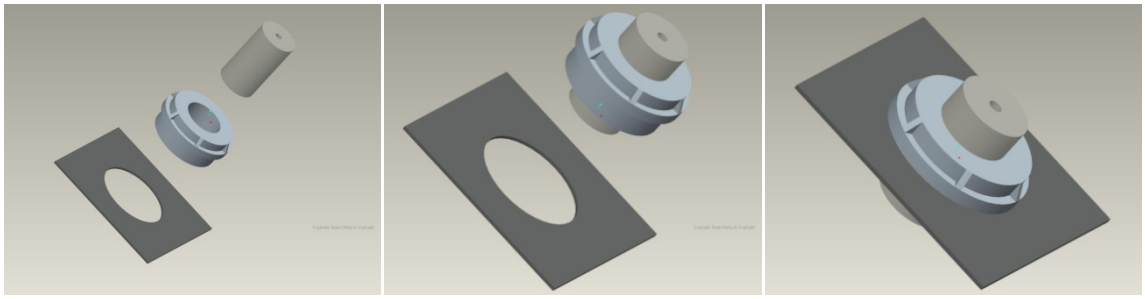

Figure 2 Assembly procedure 1 for bascule bridge fulcrum.

The second assembly procedure is characterized by the following steps:

1. The hub (middle component) is shrunk by immersion in a bath, such as liquid nitrogen at $-321^{\circ}\mathrm{F}$.
2. The hub is inserted into the girder of the bridge and allowed to reheat to the ambient temperature creating an interference fit between the girder and the hub (hub-girder interface).
3. The trunnion (inner most component) is shrunk by immersion in a bath, such as liquid nitrogen at $-321^{\circ}\mathrm{F}$.
4. The trunnion is inserted into the hub-girder assembly and allowed to reheat to the ambient temperature creating an interference fit between the trunnion and the hub (trunnion-hub interface).

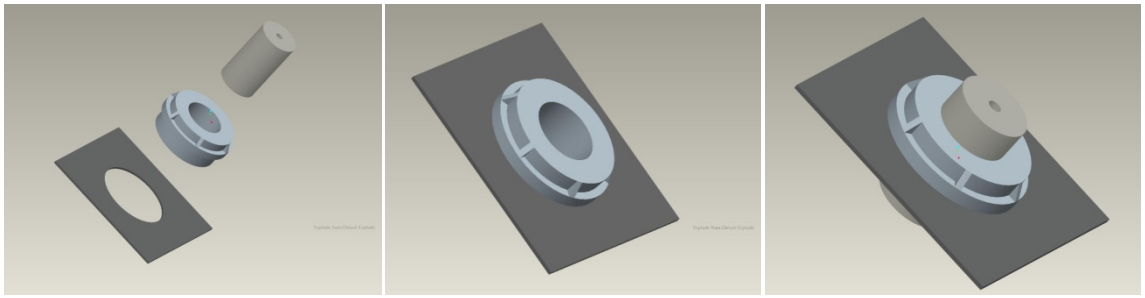

Figure 3 Assembly procedure 2 for bascule bridge fulcrum.

The third assembly procedure is characterized by the following steps:

1. Induction heating coils are placed on the girder to create sufficient thermal expansion for insertion of the hub.
2. The hub (middle component) is inserted into the girder and allowed to cool to the ambient temperature to create an interference fit between the hub and the girder (hub-girder interface).
3. The trunnion (inner most component) is shrunk by immersion in a bath, such as liquid nitrogen at $-321^{\circ}\mathrm{F}$.
4. The trunnion is inserted into the hub-girder assembly and allowed to reheat to the ambient temperature creating and interference fit between the trunnion and the hub (trunnion-hub interface).

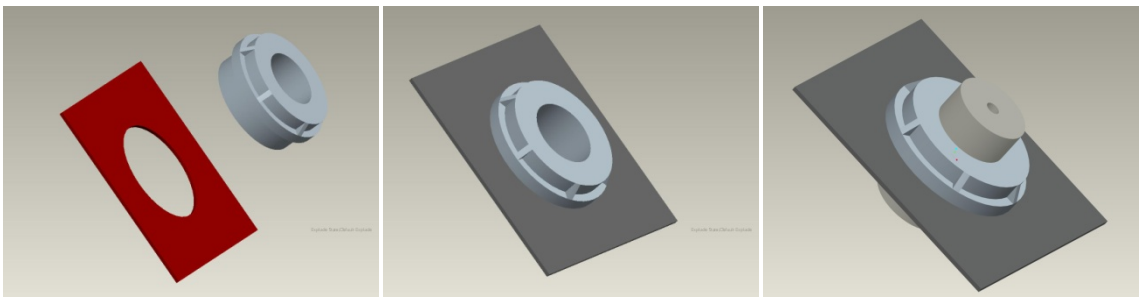

Figure 4 Assembly procedure 3 for bascule bridge fulcrum.

As mentioned previously, the Trunnion-Hub-Girder (THG) assembly is the focus of study in this paper. The current assembly procedures use liquid nitrogen ($-321^{\circ}\mathrm{F}$) to sufficiently shrink the components. During the shrink fit process, thermal stresses are developed due to the thermal shock of the cooling process, as well as interference stresses between the shrink fit components as they warm up to steady state temperature. The combination of these stresses, as well as the varying nature of the properties of steel and

the cooling mediums with a change in temperature, contributes to the possibility of failure via cracks or yielding in the components of the assembly during the assembly procedure. Due to the transient nature of this problem, stresses and failure criterion must be evaluated at each time step of the procedure. The thermal stresses developed are heavily dependent on the structural boundary conditions, but the opposite is not true. To help minimize the possibility of failure, different cooling methods, and assembly procedures are employed and such variations will be discussed in detail in this thesis.

1.3 Interference Fit Criterion

Standard interference fits used in Florida are the FN2 and FN3 fits (Shigley 1986). These fits are standard fits and are utilized all across the country in bascule bridge design. These are the standards which are used to determine exactly which type of shrink fit to employ given the loading conditions, material properties, and geometries of the parts to be shrink fit.

1. FN2 interference fit is characterized as "Medium-drive fits that are suitable for ordinary steel parts or for shrink fits on light sections. They are about the tightest fits that can be used with high-grade cast-iron external members." (Shigley 1986)
2. FN3 interference fit is characterized as "Heavy drive fits that are suitable for heavier steel parts or for shrink fits in medium sections." (Shigley 1986)

1.4 THG Problem Background

The Florida Department of Transportation (FDOT), on more than one occasion, witnessed the failure of a THG assembly in the field. In 1995, the construction of the Christa McAuliffe Bridge was brought to a standstill after the main hub component in the

assembly cracked while being shrunk in liquid nitrogen (stage 3 of AP1) [2]. In the construction of the Venetian Causeway bascule bridge in Florida, the trunnion got stuck in the hub before it reached the proper location inside the hub [2]. Both of these incidents cost the Department of Transportation hundreds of thousands of dollars in replacement materials and time lost. This prompted the FDOT to begin a study in 1998 in conjunction with the University of South Florida to determine how best to avoid these failures [1].

The complicated nature of this problem is due primarily to the fact that many of the factors affecting the possible failure of components of the assembly are not constant with temperature. Elastic modulus, fracture toughness, yield strength, thermal conductivity, specific heat, density and thermal expansion coefficient are themselves functions of temperature and so must be evaluated at each respective temperature throughout the process. The convection coefficients for the cooling media such as the dry ice-alcohol bath and the liquid nitrogen bath are also functions of temperature and thus must be evaluated with respect to time.

These considerations, when combined with varying geometries for the THG components, different cooling methods, American Association of Safety and Highway Transportation Officials (AASHTO) α ratio recommendations, and several different standards for interference fits creates a necessity for a design of experiments approach to evaluate the sensitivity of each parameter in the assembly procedure to determine which factor or combination of factors contribute most heavily to the possibility of failure in the assembly.

CHAPTER 2 LITERATURE REVIEW

2.1 Shrink Fit Literature

The use of shrink fitting as a means of assembly has been applied for many years. Shrink fitting offers many different advantages over other conventional joining processes such as welding or brazing. One such advantage is the seamless nature of the joint—no undesired changes of the material properties are necessary to join two components, as is the case in welding. These changes to the material matrix can allow unwanted imperfections to enter the lattice structure of the material at the specific points where the operations are performed, thus creating a stress concentration in those areas and increasing the likelihood for failure. These locations in an assembly are often the sight of corrosion, and as many bascule bridges are constantly exposed to the extremely corrosive coastal environment, it is necessary to minimize the possibility for failure due to corrosion.

A shrink fit design is one of the most feasible ways to create a near seamless continuity between components of an assembly. It can also be used to create a pre-stress (residual stress) state in components of an assembly [6]. Common applications often involve the transmission of rotational motion which include crank shaft-belts and shaft-bearing assemblies used in the automotive industry [23]. Other applications include cutting tool holders, wheel and bands for railway stock, and turbine disks and rotors for

electric motors [7]. Interference stresses between components effectively bind the parts together with only this interference stress and the coefficient of friction preventing translation between parts. It should be noted however, that the sudden change in the stress state going from an uncompressed to a compressed material can cause unwanted stress concentrations which can invariably cause failure if not properly planned for [7].

Many different standards are employed in shrink fit design to optimize design performance and functionality. One of the most important of these design and or production standards that must be employed is dimensional variability in the assembled components. This is an extremely important factor to consider as a large variance in the dimensions of assembled parts has been shown to dramatically alter the interference stress state of the parts which can lead to a greater likelihood of failure. Machined parts are indeed manufactured to tight tolerances, but are far from perfect. A machined shrink fit component often has an upper and lower limit by which it may vary from the nominal value [4]. These upper and lower limits are calculated using a specific interference fit criterion. For the THG assembly, a FN2 fit was deemed most desirable as it is characterized as the tightest fit possible for high grade cast-iron or steel members [8]. If the upper limit of tolerance of an inserted component is paired with a component that is at the lower limit of tolerance, a dramatic difference in the stress state can be observed [4,5].

It is often more advantageous to heat a component rather than shrink it. These procedures are often called warm shrink fitting processes. In the automotive industry, heating components is often the desired method. Commonly used procedures include heat fitting, press fitting and a combination of the two [25]. A component may be heated

and allowed to expand just enough to allow for the insertion of another component or heated such that its ductility increases enough to allow for a press to push a component part into place. Although this press-fitting method is not applicable to the THG assembly, it does offer an important perspective to shrink fitting operations as a whole as it is widely used in industry. Optimization techniques have been developed for automotive transmissions using a finite element solution considering the method of press-fitting and warm shrink fitting [25].

Methods that are based strictly on heating have been shown to create a compressive hoop stress in the inner surface of hollow cylinders [9], which may progressively close cracks near the inner surface of the cylinder. However, higher tensile hoop stresses are observed at the crack tip which would tend to open the crack further. The opposite method for shrink fit assembly, the cooling of an inserted component via immersion in a subzero liquid or some other refrigeration technique, creates tensile hoop stresses at the inner diameter of a hollow cylindrical component [9], which can lead to crack propagation. Many researchers have studied this problem. Early work by Greenberg and Clark (1968) used liquid nitrogen as a cooling medium to study the fracture mechanics and failure mechanisms of ASTM A-216-66 grade steel under varying loading conditions [15]. This work is particularly relevant to the THG problem as it represents an early characterization of the failure mechanisms of thick steel castings and includes a calculation of the critical crack length that can be observed in these castings before failure occurs. Also included in this work is an important link to the flaws inherent in steel castings and how this affects the critical crack lengths and behavior of the material in cyclic loading scenarios. Important observations were also made with regard

to the temperature dependence of both fracture toughness and yield strength of steel. This was one of the first published works to observe this trend.

Later, Nied and Erdogan (1983) used the method of superposition to analyze the transient thermal stress problem in a circumferentially cracked hollow cylinder [10]. Delale and Kolluri (1985) studied the effects of thermal shock on a radial or edge crack for a thick walled cylinder [11]. Other researchers, such as Noda (1985) studied specifically the stress intensity factor as it relates to the transient thermal loads in standard cylinders and edge plates [12,13]. Noda used a finite differencing approach to obtain a transient solution. Oliveira and Wu (1987) were able to calculate the stress intensity factors for both internal and external cracks in hollow cylinders subjected to a thermal stress gradient. This work also investigated the fracture toughness of hollow cylinders of varying geometries under the same thermal gradients [14]. To obtain these solutions, a closed-form weight function was used. In more recent work, researchers calculated stresses for various shrink fit joints using a finite element solution and then compared these results to the stresses found using elasticity theory (i.e. Lame's equation) [24]. The principle of virtual work was applied to formulate the finite element solution.

Another unique problem to consider in shrink fit design is fretting. Fretting occurs when the interference stress between assembled components is insufficient to prevent translation between these components [7]. This can occur in shrink fit components subject to high torque loads and alternating stresses, as is often the design intention for shrink fit applications. Also, in applications where an external thermal load can inadvertently be applied, such as in an overheating engine, the integrity of the shrink fit hold may be compromised as an unexpected thermal load may cause unwanted

thermal expansion. This may contribute to a greater likelihood of fretting wear in assembled components. If the relative magnitude of the slip between components is not continuous or large, premature failure may be avoided. Although the THG assembly would never encounter fretting danger due to the fact that the THG assembly would never encounter a significant torsional load, fretting damage remains as an important design consideration in shrink fit applications.

The uses of shrink fit applications can be extended to manufacturing as well. In a procedure called autofrettage, a pressure vessel is subjected to very high internal pressures which deform the material past the elastic limit into the plastic zone where yielding occurs. The result of this applied pressure is a compressive residual stress along the interior of the vessel. The ultimate goal of the process is to increase the durability of the vessel. The residual stress created during this process can be used to the advantage of the design engineer. For instance, when manufacturing large caliber gun barrels of battleships and cruisers, this residual compressive stress helps to offset the large bursts of pressure (tensile hoop stress) caused when the gun is fired.

Modeling a shrink fit process can be quite complicated and although some formulas derived from elasticity theory, e.g. Lame's equation [23], are commonly used to estimate tangential and radial stresses, often the complexity of the problem tends to lead to a finite element solution. Many characteristics such as the finite extent of contact surface area, localized variations in thermal gradient, changing material properties with temperature, non-uniform cooling, and even uncontrollable random variables such as the standard deviation of the dimensions of the assembled components must be considered

for an acceptable solution to be obtained [23]. In this work, as in many others, a finite element approach will be the method of choice to obtain solutions.

2.2 Literature—THG Assembly

Initial groundwork for this problem was laid out by Denninger (2000). In his MS thesis, he developed software which allowed the user to evaluate the torque on the THG components in a bascule bridge, as well as analyze the effect of specific interference fits on the stress state of the assembly and corresponding bolt patterns used in construction [16]. However, this work did not include the transient stresses induced in the assembly as it is heated or cooled over time. To fill this gap, Ratnam (2000) later used a finite element model constructed in ANSYS to further study the steady state and transient stress states occurring during assembly [17]. This work also concluded that in AP1, the smallest critical crack lengths were observed when hoop stress was high and temperatures were low, and that high hoop stress alone does not singularly contribute to failure. Also, this study concluded that the stresses due to interference and thermal shock never occurred together during the shrink fit process of AP2, thus lowering the likelihood for failure by increasing the critical crack lengths in that assembly procedure. Nichani (2001) later confirmed the work of Denninger and Ratnam by performing full-scale testing on the THG assembly [2,3]. Through experimentation, his results confirmed the stresses predicted by the ANSYS finite element models and the earlier suspicion that AP2 was a safer assembly procedure.

In contrast to previous works, Berlin (2004) provided a unique perspective to the THG problem by choosing to analyze a different assembly procedure entirely. He

proposed to heat the girder using heating coils which would allow for the insertion of the TH assembly [18]. This method depends critically upon the location of the heating coils in relation to the girder hole, and future studies will be conducted to determine the best coil locations for optimum thermal expansion. This work was the initial groundwork for AP3, and this thesis studies this assembly procedure in greater detail.

Collier (2004) created an axisymmetric finite element model to study the temperature dependence of material properties in a long compounded composite cylinder [18]. This work also demonstrated the first attempt at a step cooling procedure, whereby the components are first cooled in a refrigerated air chamber before being immersed in liquid nitrogen. It was shown that this decreased the likelihood of failure by as much as fifty percent. However, this work was not applied specifically to the THG geometries and so could not be directly applied.

Paul (2005) then performed a sensitivity analysis on the THG assembly by using the inside diameter of the hub and outer diameter of the trunnion as design parameters [20]. The analysis studied the effect of these parameters on the critical crack lengths and critical stresses in the assembly stages of the THG assembly. These results were limited however, as only one cooling method was employed (liquid nitrogen), and the analysis was performed for only one THG geometry.

Nguyen (2006) performed the most comprehensive analysis of the THG assembly to date. A full design of experiments analysis was performed with four different cooling methods, two radial interferences (high and low), and three current American Association of State Highway and Transportation Officials (AASHTO) α ratios (hub radial thickness/hub inner diameter) as problem parameters [4,5] These tests were performed

on three different THG geometries taken from three separate bascule bridges in the state of Florida. A one sixth axisymmetric finite element model was constructed in ANSYS and evaluated for each possible case. This analysis showed the specific contributions of each parameter on the Overall Minimum Critical Crack Length (OMCCL) and Overall Minimum Stress Ratio (OMSR) outputs for each respective bascule bridge. It was shown that varying the cooling methods contributed most to increasing the OMCCL and OMSR values. Specifically, the second cooling method employed—immersion in a dry ice-alcohol bath, followed by immersion in liquid nitrogen—was the most effective and contributed to an increase of 262 to 406 percent in the OMCCL, and 17 to 87 percent increase in OMSR. This work was performed for AP1 only, however, and may be extended into AP2 and AP3.

2.3 Problem Parameters

In his MS thesis for the University of South Florida, Nguyen (2006) used this design of experiments approach to study AP1 [5]. Two different critical design criteria were used by Nguyen in his analysis. As stated previously, the first parameter is the Overall Minimum Critical Crack Length (OMCCL) [4,5] which is defined as the minimum crack length that can exist in any step or time of the assembly procedure before catastrophic failure occurs. If a crack in the material extends beyond this minimum, catastrophic failure will likely occur instantaneously. Analytically, when the stress intensity factor K_1, is equal to than the fracture toughness $K_{Ic}(T)$ of the material, the crack length reaches the max crack length allowable before a crack propagates catastrophically [4]. Fracture toughness is a material property of steel and decreases with

a decrease in temperature. The stress intensity factor of a radial edge crack that is small in comparison to the thickness of the cylinder is given as

$$K_1 = f_e \sigma_\theta \sqrt{\pi a}$$

Equation 1 Stress intensity factor of a radial edge crack.

where a represents the crack length, f_e is the edge effect factor, and σ_θ is the tensile hoop stress. Figure 5 below shows the loading conditions and geometry used to calculate this parameter.

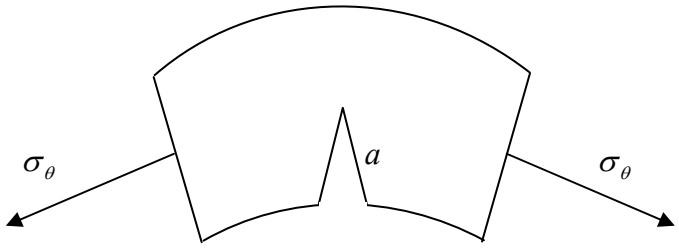

Figure 5 Edge crack in radial direction in a hollow cylinder (crack is small compared to radial thickness) [4].

The ratio of the fracture toughness to the stress intensity factor is established, solving for the crack length a, and redefine it as the OMCCL. The equation is given by

$$\text{OMCCL} = \min\left(\frac{K_{Ic}^2(T)}{f_e^2 \pi \sigma_\theta^2}\right)$$

Equation 2 Overall Minimum Critical Crack Length (OMCCL) [26].

From this equation, it is easy to deduce the temperature dependent nature of this problem. The fracture toughness is given as a function of temperature and decreases with

a decrease in temperature. The hoop stress is also equivalently a function of temperature as a high thermal gradient due to thermal shock causes tensile hoop stress values to increase. These thermal stresses must also be considered in conjunction with the interference stresses created by the insertion of one component into another. As seen by this equation, high values of hoop stress may or may not mean the lowest values of the OMCCL. It is the combination of high hoop stress and low fracture toughness at specific times in the cooling procedure that leads to the smallest values of the OMCCL. This is when the assembly is most likely to fail.

The other critical design criteria used by Nguyen is the Overall Minimum Stress Ratio (OMSR) [4,5] which is defined as the minimum stress ratio that the assembly can withstand before failure via yielding. If the Von Mises stress σ_e is greater than the yield strength $Y_s(T)$ of the material at any temperature or time (stress ratio less than 1), the component is in danger of failure. Equation 3 shows the OMSR.

$$\text{OMSR} = \min\left(\frac{Y_s(T)}{\sigma_e}\right)$$

Equation 3 Overall Minimum Stress Ratio (OMSR) [4].

The yield strength, like the fracture toughness, is also a function of temperature but it increases with a decrease in temperature. Figure 6 shows the temperature dependence of both the fracture toughness and yield strength as a function of temperature.

The von Mises stress is also equivalently a function of temperature but depends on a combination of both the radial and hoop stresses at any given time. Again, it is seen that the OMSR is not necessarily calculated at the time where the von Mises stress is

largest. It is the combination of low yield strength and high von Mises stress at a specific time that will produce the smallest value of OMSR.

In either of the previously mentioned assembly procedures, thermal stresses as

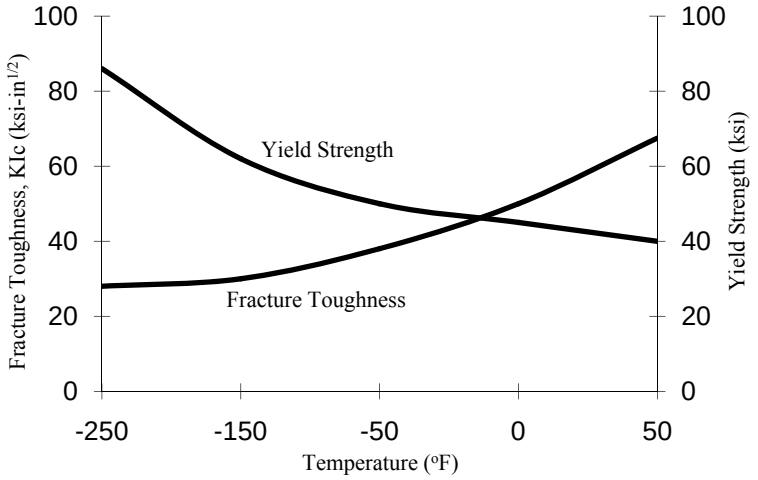

Figure 6 Yield strength and fracture toughness of cast steel as a function of temperature [15].

well as interference stresses are observed during either assembly process. It is important to note, however, that a change in the assembly procedure can dramatically change the stresses experienced by the components. As previous works have shown, AP2 shows significantly lower likelihood for catastrophic crack failure [1,2,4,5]. The primary reason for this is that the interference stresses between the hub-girder interface developed after stage two of AP2 supply a compressive stress to the hub as it warms up in the final portion of stage three in AP2. This compressive stress helps to negate some of the tensile stress produced by the trunnion as it warms back up to the ambient temperature [4]. It is not known, however, which parameters affect the OMSR and OMCCL values the greatest in AP2 which is a topic of this thesis.

In addition, Figure 6 also demonstrates that in AP3, during the first step of the assembly procedure (heating of the girder) there is little likelihood for failure via crack propagation as the fracture toughness of ASTM A36 steel increases with increasing temperature. An increase in temperature does suggest a greater probability for failure via yielding however, as the yield strength of most steels decreases with an increase in temperature.

2.4 Objective of This Thesis

The work of this thesis includes a similar sensitivity analysis as done by Nguyen but will be conducted on AP2 and AP3. The critical portion of AP2 is thought to be the first stage of the assembly procedure whereby the hub is dipped into liquid nitrogen [1]. As such, the sensitivity analysis on AP2 focused on this stage of the assembly procedure and varied cooling methods, AASHTO parameters, and THG geometries as in the previous work of Nguyen (2006). Also, the finite element model created by Nguyen (2006) in ANSYS is being improved to ensure the best results possible. Improvements include mesh refinements and a new meshing scheme which allowed for greater model continuity and improved results.

A similar sensitivity analysis is also conducted for AP3, where the critical step in the assembly procedure is shown to be the third stage of AP3—immersion of the trunnion component into liquid nitrogen. This assumption is verified provided that OMSR and OMCCL values are large for all time steps and loading conditions for the other steps in the assembly procedure. Two finite element models were generated simulating the heating of a 60"×60"×0.75" steel plate with a central hole and of the entire girder

geometry. Both models were loaded with the same thermal conditions and allowed to heat up for the same amount of time. The OMCCL and OMSR values were calculated for each time step for both models. Both models produced large critical crack lengths and stress ratios suggesting that this stage of the assembly procedure would not be a point of failure. From this data, it was concluded that the only critical step in AP3 was the cooling of the trunnion in liquid nitrogen. Chapter 4 in this thesis will explain these models in much greater detail.

In this thesis, a full comparative analysis, including both quantitative and qualitative data, on all parameters—including geometry, cooling methods, and interference fits for all assembly procedures. It is important to verify the best overall assembly procedure with the least likelihood for failure, but also the greatest ease of implementation and greatest practicality. From this thesis, bascule bridge designers will have a much greater reference to the variations in assembly procedures and the associated strengths and weaknesses of each.

CHAPTER 3 PROBLEM GEOMETRY

3.1 Introduction

Variation in hub geometry is a critical factor to study. As previous works and field experience has shown, for different hub geometries, subject to the same loading conditions, failure can occur in certain hubs and not others. This is an important observation as it reveals the sensitivity of geometry on the hoop and Von Mises stresses encountered, and thus the OMCCL and OMSR values. The relationship between the structural and thermal boundary conditions and the geometry is also apparent. For hub geometries that contain a larger flange, and subsequently a larger gusset, the distribution of thermal gradients and thermal stresses can change drastically relative to a hub with smaller dimensions. This can also affect the location of the critical stresses observed in the geometry, and even the time step at which these stresses are observed. The following chapter will explain in detail the variations in geometry for each TH assembly.

3.2 Geometry of Assembly

3.2.1 Assembly Procedure 1

AP1 is the most common assembly procedure used today but is perhaps the most likely to fail. This is due to the combination of high interference stresses as well as thermal stresses due to the immersion of the entire TH assembly in liquid nitrogen—the

currently used cooling medium. Figure 7 and Figure 8 below depicts the TH assembly variables used in this thesis as well as in the work of Nguyen.

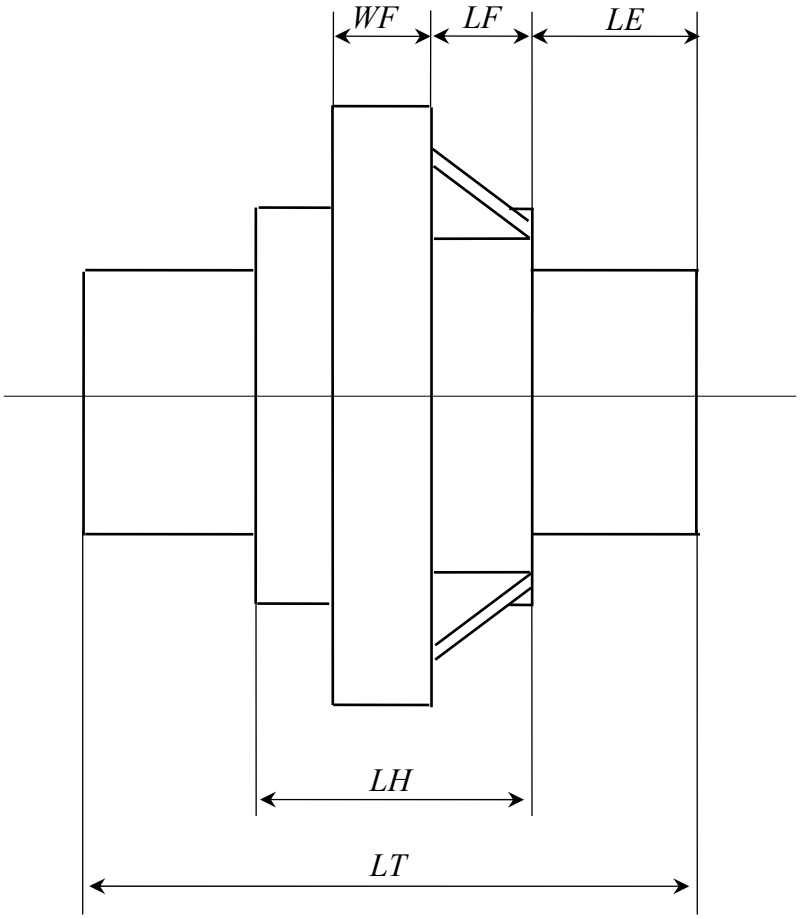

Figure 7 Side view of TH assembly for AP1 [5].

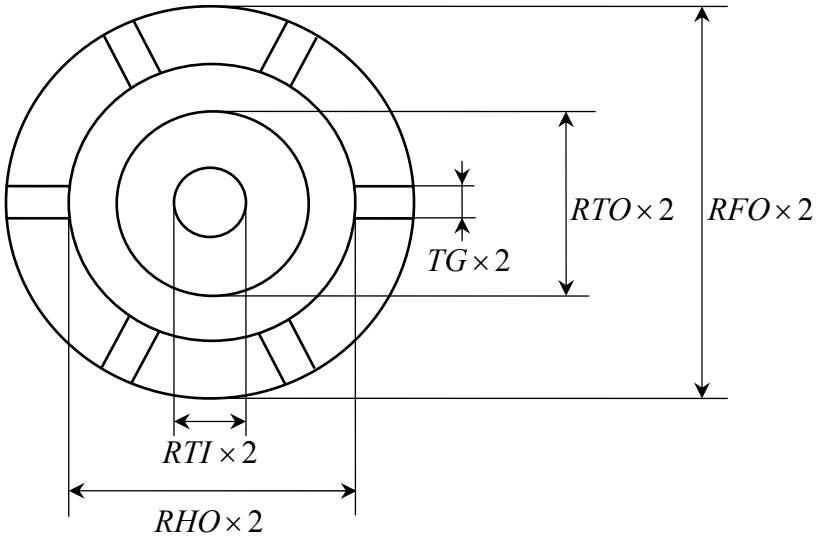

Figure 8 Front view of TH assembly for AP1 [5].

These parameters defining lengths and other variables were used to help construct the model in ANSYS. These parameters are used as part of the ANSYS parametric design language which is described in Chapter 4. The use of these parameters is consistent for every bridge, although the values they represent change. The parameters for the small, medium and large bridge are given in Table 1.

Table 1 Geometric parameters for the TH assembly for all bridges.

Parameter	17th Street Bascule Bridge	Christa MacAuliffe Bascule Bridge	Hallandale Bascule Bridge
WF—width of Flange	1.25	1.75	3.00
LF—distance to hub flange	4.25	4.25	7.00
LE—gusset side trunnion ext.	6.00	18.5	26.0
LH—length of hub	11.0	16.0	28.0
LT—length of trunnion	23.0	53.5	80.0
RFO—flange radius	13.2	27.0	30.0
RTO (same as RHI)—trunnion inner radius	6.47	9.00	13.0
TG—gusset thickness	1.25	1.50	2.00
RTI—trunnion inner radius	1.19	1.00	1.50
RHO (varies)—outer hub radius	8.88	16.0	17.5

3.2.2 Assembly Procedure 2

The geometry of AP2 is the same as AP1 with the exception that the trunnion is absent. With this in mind, the parameters RTO, RTI, LE, and LT can be omitted from Table 1 when building the assembly for AP2. The only factor that changes in this geometry is the RHO factor which changes due to the changes in the AASHTO alpha ratio.

The AASHTO alpha ratio is the ratio of the hub radial thickness to the hub inner diameter. The alpha ratio for all bridges is calculated from the following equation:

$$\alpha = \frac{\text{hub radial thickness}}{\text{hub inner diameter}} = \frac{RHO - RTO}{2RTO}$$

Equation 4 AASHTO alpha ratio.

3.2.3 Assembly Procedure 3

The geometry of AP3 varies significantly with the model that is chosen for analysis. There are two main models in AP3 and each has geometries specific to the problem parameters. The first model is simply used to prove that the heating of the girder is not a critical step of AP3, and the second model is the trunnion by itself.

3.2.3.1 Model 1: Plate and Hub

The first model constructed for AP3 is composed of a plate of dimensions $WID \times HEI \times THI$. This model is used as a platform to make assumptions about the full girder. Stresses and strains developed in this model due to applied thermal loads should be relatively similar to the stresses and strains observed in the full girder. This model provided a good reference point to solve tough modeling problems that might have otherwise been more difficult to tackle had this model not been created. However, this model does not fully represent the process at hand, so some assumptions are made regarding the ability of this model to accurately represent the full girder.

The second portion of this model includes the hub component. The hub component is lowered into the plate hole after sufficient thermal expansion is created to allow for insertion. Previous sections in this chapter detail this geometry explicitly.

Many different coil configurations were tried to generate sufficient heat in the plate, but also allow for ease of modeling and good results when generated in ANSYS. Initial configurations followed the work of Berlin who used a square coil configuration to

heat the plate [18]. These proved difficult to use however, as the hub geometry is largely suited to a cylindrical coordinate system and the plate and coils in this configuration are suited to a Cartesian system. For this reason, it became difficult to generate good results in the analysis with a square coil configuration. Figure 9 shows the general model geometry of AP3. Figure 10 shows the coil geometry and parameters used for the square coil assembly. Four main coils were used and were laid out approximately the same distance apart from one another.

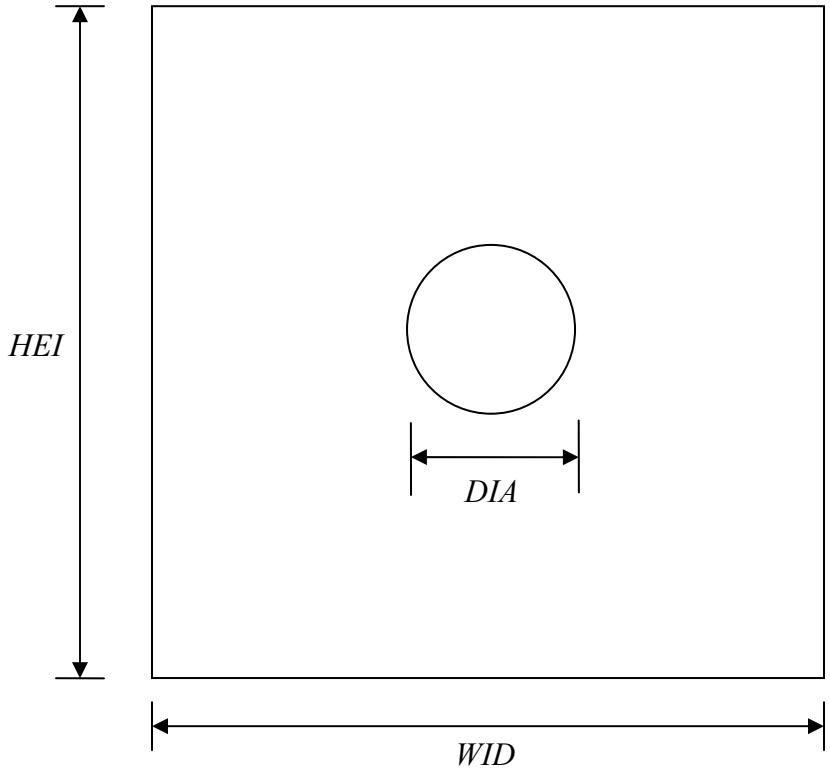

Figure 9 Geometry and parameters used for Model 1 of AP3.

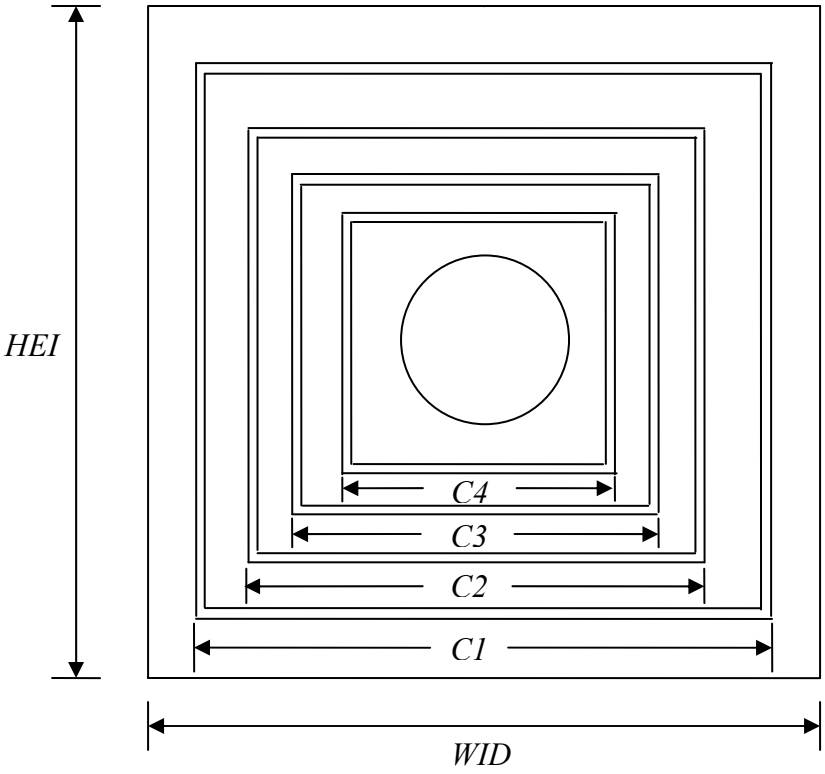

Figure 10 Model 1 of AP3 with square coil configuration.

The answer to this was to generate a circular coil configuration around the girder hole. The primary reason for this change was to allow for the mesh of the hub and the plate to match up more evenly allowing for a better solution to be obtained. Particularly, this configuration benefited the second part of Model 1, the insertion of the hub into the heated plate component. The contact problem associated with this step was much easier to solve with a circular configuration versus a square configuration. Figure 11 shows the circular coil configuration and the associated parameters used in the analysis. Further details of this model and the geometry are discussed in Chapter 4.

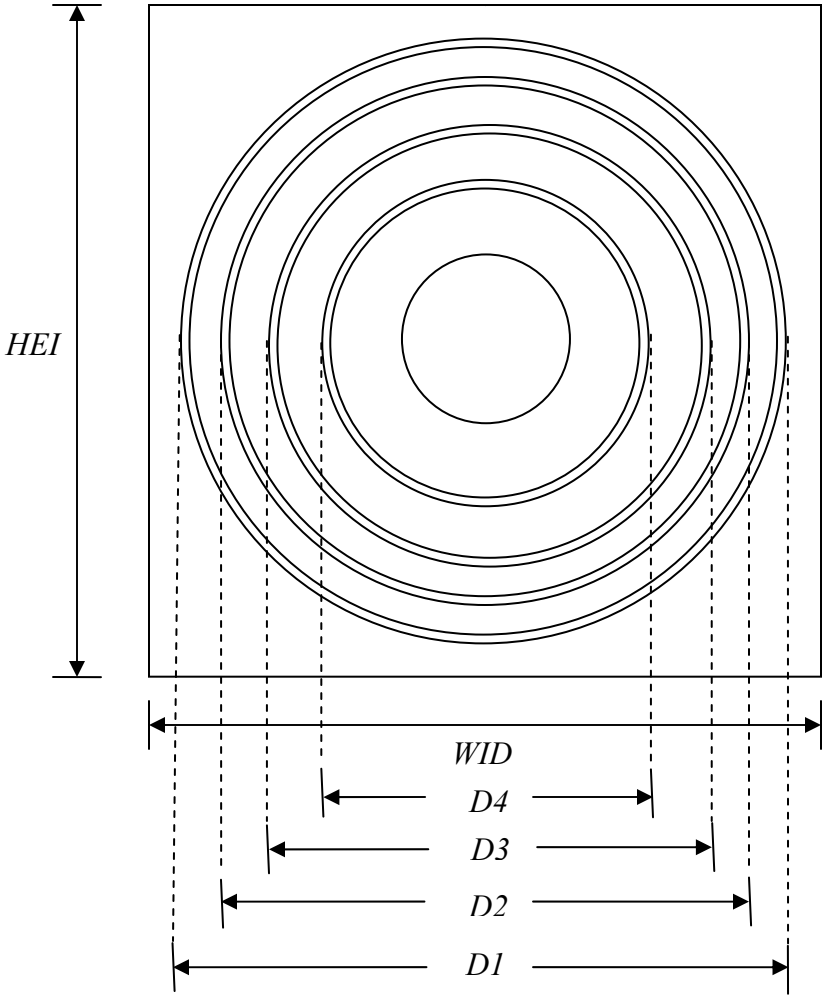

Figure 11 Circular coil configuration for Model 1 of AP3.

CHAPTER 4 ANSYS MODELING

4.1 Introduction

Finite element modeling is perhaps the greatest tool at the fingertips of modern engineers. It provides a virtually limitless platform upon which many engineering problem can be solved to a high degree of accuracy. To calculate and solve the equations needed to accurately represent the THG problem would be extremely difficult, if not impossible to do analytically. This chapter details the finite element modeling for this thesis, including the choice of element type, analysis type, method of modeling, model accuracy and all convergence analyses performed on various models.

4.2 ANSYS Parametric Design Language (APDL)

The ANSYS Parametric Design Language (APDL) is a generalized program language that can be used to generate model geometries, element types, loading conditions, etc. and virtually any other factors in terms of variable names or parameters. It is the programming equivalent of the graphical user interface (GUI) that is normally used in ANSYS. Almost all operations performed in the GUI can be written as APDL code, and are kept in a running database (db) log file and this database file can be output by the user at any time. The ANSYS parametric design language is written in FORTRAN coding, and much of the syntax is similar to typical FORTRAN operations.

All models and operations for this thesis were generated using this coding as it is much more convenient to use and allows the user total control over the input, outputs, and all model related operations in between. It also allows for the use of loops and conditional "if" statements which add a greater degree of freedom to the user. APDL code can be generated as a text file and run through ANSYS in a much shorter time than it would take a user to execute identical operations in the GUI. In addition, APDL code allows for the versatility of executing just a section of the code which makes debugging the model much easier.

4.3 Higher vs. Lower Order Elements

Most elements in the ANSYS element library are lower order elements meaning that they do not have mid-side nodes and cannot account for nonlinear physical phenomenon (large deflections in bending, etc.). Lower order elements generally consist of eight node (hexahedron) and four node (tetrahedral) elements. They are the most commonly used elements in finite element analysis as they require less computation time than higher order elements. This advantage comes at a cost however, as higher order elements are much more effective at modeling irregular geometries due to the use of mid-side nodes in higher order elements. The elements used in this work were all lower order elements as it was not necessary to model large deflections or nonlinear characteristics. This also helped to reduce computation time while recording data.

4.4 Analysis Type

4.4.1 Coupled Field Analysis

Many different types of options are available in modern finite element packages which allow the user a greater degree of freedom in modeling and analysis. Depending on the needs of the user, one analysis type may be more appropriate given a specific situation or need. Coupled field analysis is an analysis that combines two or more physics or engineering fields and their associated principles to generate a solution. This analysis type is the most useful as it is the most common amongst real world applications.

4.4.1.1 One-Way Coupled Field Analysis

A one-way coupled field analysis is often used to describe the coupling of only one field of physics or engineering with another, but the two fields do not necessarily affect each other. The best example of this analysis is a thermal stress problem whereby a thermal load is applied to a volume of a material, and thermal strains and stresses are produced as a consequence. The thermal strains affect the overall stress field, but if any structural strains are also applied, it is safe to assume that the distribution of the strain field due to these external loads will have no effect on the overall temperature distribution. This is not true of the thermal loading however, as a thermal load will certainly induce thermal stresses which will affect the stress field. In this problem, there is a one-way coupling between the fields in the analysis.

4.4.1.2 Two-Way Coupled Field Analysis

In two-way coupled field analysis, the two fields interacting directly affect each other for any given loading. Iterations must be performed in each solution field relative to the other field in order for convergence of the solution to take place. The best example of this analysis type is a piezoelectric problem where the structural displacements directly affect the electric field output and vice versa. A similar process could also take place between the same physics field. An example of this would be the dependence of a natural convection coefficient on temperature and vice versa. Each component directly affects the output of the other and so a continually iterative process is needed for accurate estimation of both the temperature and the convection coefficient.

4.4.2 Direct Coupled Field Analysis

Direct coupled field analysis utilizes several fields of physics under one element type to solve for the solutions to all fields simultaneously. Within this element contains all necessary degrees of freedom that the user requires to achieve the desired output. Virtually all available element types have a direct coupled field element with many different capabilities. Some common direct coupled field elements include (SOLID5, PLANE67, SOLID98, TRANS109, FLUID116, etc.) These elements are particularly useful when the user wishes to cut down on overall APDL code complexity (as there is less to program), but as all fields of a given element must be solved for simultaneously and as such, this method of solution tends to have longer computation times. The direct coupled field element SOLID5 was used in the analysis of the first two models for AP3 to simultaneously solve for the thermal stresses associated with the thermal loading.

4.4.3 Sequential Coupled Field Analysis

Sequential coupled field analysis solves for each physics field sequentially. The results from the first analysis are used as loading conditions in the next solution field. In this way, one solution depends directly upon the results of the previous analysis. Element changes are usually needed in this type of analysis as the element types used for each segment are only able to solve for certain degrees of freedom. For example, Nguyen (2006) used coupled field analysis in his thesis by first solving the thermal problem simulating the dipping of the TH assembly in liquid nitrogen, then using the results of the analysis to solve for the thermal stresses induced in the material due to the thermal loading [4,5]. An element change was performed from SOLID70 (thermal solid element) to SOLID185 (structural solid) to calculate the thermal stresses developed due to the thermal load.

This type of analysis is very useful in that each separate field of physics produces its own independent output, which allows for a greater degree of freedom for the programmer. This analysis method traditionally has lower computational time than the direct coupled field elements as all degrees of freedom are not solved for simultaneously—only a select few as designated by that particular element. The computation time is directly related to the number of physics fields being solved for, so if many different solutions are required in several different fields, a direct coupled field element may be more appropriate and efficient.

This method was used to re-run the trials for AP1 and to run all trials for AP2 for this thesis. A direct coupled field analysis was used for model verification in AP3, but the analysis done for step 3 of AP3 was done using a sequential coupled field approach.

4.5 Element Types

Many different element types exist in ANSYS and can be used to solve a virtually limitless number of problems. Their range of abilities includes, but is not limited to thermal, structural, magnetic, electric, piezoelectric, fluid, contact, and modal problems and any combination of these used in tandem with one another. ANSYS has both two and three dimensional elements available to the user to define a wide range of problems. Often, an analysis can be simplified by using a planar (2-D) element in place of a solid (3-D) element thus limiting computation time. The element types that exist in the ANSYS library include SOLID, PLANE, LINK, SHELL, BEAM, MASS, PIPE, MATRIX, COMBIN, INFIN, FLUID, VISCO, CIRCU, TRANS, HF, ROM, SURF CONTA, TARGE, and others. The use of these elements encompasses a very broad base of topics and modeling options to suit real world analyses.

Each element is designed to model specific degrees of freedom such as temperature, displacement, etc. and is limited by these degrees of freedom. For example, it is impossible to use a thermal element such as SOLID70 to solve for the thermal strains due to an applied thermal load because the only degree of freedom defined for this element is temperature. This temperature data can be used, however, in a subsequent analysis using a structural element to find thermal strains and stresses associated with a given thermal load (sequential coupled field analysis).

The elements used in this thesis were three dimensional elements—SOLID5, SOLID45, SOLID70, SOLID90, SOLID185, and SOLID186 as well as contact elements—CONTA174, and TARGE170. A brief description of each element's capabilities will follow, as well as its specific usage in this thesis.

1. SOLID5: A lower order, eight node 3-D direct coupled field element capable of solving thermal, structural, magnetic, electric, and piezoelectric problems and any combination of these simultaneously. The element has six faces (hexahedral) and a total of six available degrees of freedom at each node. The available degrees of freedom are (u_x, u_y, u_z) displacements, temperature (TEMP), voltage (VOLT), and scalar magnetic potential (MAG). The usage of this element was used in modeling the plate and girder models in AP3. It was chosen because of its direct coupled field ability—both thermal and structural problems were solved simultaneously thus shortening the required APDL code. This choice came at the cost of computation time however, as direct coupled field elements traditionally require longer to solve.
2. SOLID45: A lower order, eight node 3-D structural element capable of solving structural problems. The element has six sides and three available degrees of freedom at each node—displacement in *x*, *y*, and *z* directions (u_x, u_y, u_z). If the finite element analysis requires additional degrees of freedom, this element can be used as part of a sequential coupled field analysis to solve a multi-physics problem. The element also has plasticity, creep, swelling, stress stiffening, large deflection, and large strain capabilities. This element was used in AP1 as the primary structural element for solving for interference stresses in the contact analysis. Later during the AP1 analysis, as per the sequential coupled field analysis, this element is changed to its thermal counterpart SOLID70 for subsequent thermal analysis.

3. SOLID70: A lower order, eight node 3-D thermal solid element capable of solving thermal problems. The element has six sides and only one available degree of freedom at each node—temperature (TEMP). If the finite element analysis requires additional degrees of freedom, this element can be used as part of a sequential coupled field analysis to solve a multi-physics problem. This element is used in both AP1 and AP2 as part of the sequential coupled field analysis. Specifically, this element solves for the temperatures of the nodes at each time step due to the applied convective cooling loads of the various cooling medium used in the analysis. In both AP1 and AP2, this element is later changed to SOLID185 to solve for the thermal strains and stresses at each time step for a given temperature distribution.
4. SOLID90: A higher order version of SOLID70, this twenty node thermal solid element is capable of solving thermal problems and is ideal for modeling complex geometries due to its mid-side nodes. This added benefit comes at the cost of computation time however, which increases much more dramatically with increased mesh density versus lower order elements. Much like SOLID70, this element has six sides and only one degree of freedom for all nodes—temperature (TEMP). This element is used exclusively in AP2 with the explicit purpose of dealing with some elements in particular locations in the model that are often distorted as the mesh density increases. This element offers greater modeling flexibility as it can handle larger aspect ratios in its elements versus lower order elements. This element is later changed to SOLID186, a higher order structural

solid element to solve for thermal strains and stresses in the material at every time step due to the applied thermal load.

5. SOLID185: A more advanced version of SOLID45, this is an eight node 3-D structural solid element capable of solving structural problems. This element has three degrees of freedom at each node—displacement in *x*, *y*, and *z* directions (u_x, u_y, u_z). The element has plasticity, creep, stress stiffening, large deflection, and large strain capabilities like SOLID45, but also has advanced options which allow it to model incompressible elastoplastic materials, as well as fully incompressible hyperelastic materials. SOLID185 also has more solving techniques available through its keyopts such as the selective reduced integration method, the uniform reduced integration method, and the enhanced strain formulation method. None of these methods were used in this thesis as they pertain largely to hyperelastic and elastoplastic materials. As mentioned earlier, this element is used as part of the sequential coupled field analysis in AP1. After the interference and thermal stresses are found in the initial stages of the analysis, an element change is performed from the thermal element SOLID70 to SOLID185 whereby the combined interference stresses and thermal stresses are calculated for each time step.
6. SOLID186: A higher order version of SOLID185, this 20 node structural solid element is capable of solving structural problems and is ideal to model complex geometries and curved surfaces due to its mid-side nodes. Like previous elements SOLID45 and SOLID185, this element has three degrees of freedom at each node—displacement in *x*, *y*, and *z* directions (u_x, u_y, u_z). This element exhibits

quadratic displacement capabilities meaning it can represent displacement as a quadratic function as opposed to a linear function as is more often the case in solid mechanics. This element is used exclusively in AP2 as the second step in the sequential coupled field analysis. During the first stage of this analysis, SOLID90 is used to solve for the temperatures at every time and every node due to the applied convective load. When a thermal to structural element change is performed, SOLID186 is then used to calculate the thermal strains and stresses at each time step and node based on the previous thermal analysis.

4.5.1 Contact Analysis

Very rarely is analysis of contact between two surfaces in finite element modeling an easy process. Due to the inherent difficulty in modeling this problem analytically, finite element approximations are also appropriately complex and rather arduous to model accurately. Analytical models have been developed for special ideal cases—contact between two spheres, two parallel cylinders, cylinders on a flat plate, gear teeth, and some bearing applications such as roller bearings. Contact analysis in finite element modeling typically requires a much greater computational resource, and has many assumptions that go into generating a correct solution. These problems are also prone to convergence problems, often converging very slowly or not at all. Many modern upgrades in finite element software have eliminated various problems through advanced solving techniques and options that assist the calculations to allow for easier convergence.

Both AP1 and AP3 involve the use of contact elements to solve for the stresses due to the shrink fitting process. Additionally, the contact problem in AP3 requires an addition to the previous work done in AP1 in that contact between components does not occur initially. As per the second step of AP3, as the girder cools to steady state temperature, interference stress develops in the HG assembly slowly due to the contraction of the girder around the hub. Therefore, no contact between components exists initially. This differs from the contact analysis performed in AP1 where the entire TH assembly was dipped into liquid nitrogen. Interference between these components had already been made in the previous step, and so modeling the contact problem was solved with respect to this condition.

Solving contact problems in ANSYS requires the use of *contact* and *target* elements. These elements are specifically designed to model contact between components due to an applied load of some kind—change in temperature, force, stress, etc. Many different types of contact can be modeled in ANSYS—node-to-node, node-to-line, node-to-surface, and surface-to-surface contact. The specific behavior of the "contact pair" created between the contact and target elements can also be specified—rigid-to-flexible and flexible-to-flexible boundary conditions. The contact between the TH assembly and the HG assembly occurs over a relatively large area with respect to the element sizes used and so surface-to-surface contact analysis was performed. These components were also expected to undergo deformation, so flexible-to-flexible contact was chosen as the appropriate boundary condition.

From the onset of any contact problem, it is necessary to establish which surface will be the contact and target surfaces respectively. Many guides are available to help

distinguish these surfaces such as the ANSYS Structural Analysis Guide, Release 10.0 which states that "*If one surface is markedly larger than the other surface, such as in the instance where one surface surrounds the other surface, the larger surface should be the target surface.*" [21] Table 2 below shows the list of contact and target elements used in this thesis as well as surfaces that each of these elements were assigned to. Note that only the first stage of AP2 is studied—when the hub is immersed in liquid nitrogen. As such, no contact elements were required for AP2.

Each "contact pair" that is generated between a contact element and its associated target element shares a set of real constants which describe various aspects of the behavior of the elements at the contact region. It is important to note that each contact pair will share one set of real constants which apply to both elements.

Table 2 List of contact and target element usage in present work.

Assembly Procedure	Contact Surface	Contact Element Used	Target Surface	Target Element Used
AP1	Trunnion outer diameter area	CONTA174	Hub inner diameter area	TARGE170
AP3	Hub outer diameter area	CONTA174	Girder hole area	TARGE170

These elements were chosen as they are surface-to-surface contact elements, and can handle flexible-to-flexible contact conditions. A brief summary of the capabilities of each element will follow as well as its specific use in this thesis.

1. CONTA174: This is a three-dimensional, four-node, surface-to-surface contact that it is compatible with higher order elements with mid-side nodes. This element is considered a "deformable" element surface and takes on the geometric characteristics of any solid or shell element to which it is connected. This

element is used in AP1 and AP3 to study the interference stresses developed in various stages of these assembly procedures. It was chosen for use due to its compatibility with SOLID45, the element used to model the TH components.

2. TARGE170: This is a three-dimensional, four-node, surface-to-surface target element used to designate a "target surface" for many associated contact elements (CONTA173, CONTA174, CONTA175, CONTA176, and CONTA177). This element may or may not be initially in contact with its associated contact element, and contact can be made incrementally via various keyopts available to the user. This target element can easily model complex target surface shapes. For flexible target areas, like the ones assumed in this work, the target elements generated will overlay the solid, shell, or line elements which define the boundary between the contact pair [21]. This element is used in both AP1 and AP3 as the target element in the contact pair. In AP1, the target surface is the hub inner diameter surface area, and in AP3 the target surface is the surface area of the hole in the girder.

4.6 Convergence Testing

Convergence testing is performed for finite element modeling to ensure an accurate solution is obtained with relatively small error in the results. The degree of accuracy achieved in finite element analysis is directly related to the mesh density. In theory, infinite mesh density would yield a perfectly accurate solution but this is computationally impossible to attain and entirely impractical. It is important to note, however, that finite element analysis by definition is an approximation and subject to error inherently, and that this error is associated directly with the mesh generation,

element size and shape, as well as overall model continuity. Often, a densely meshed model with poorly shaped elements will have a much less accurate solution than a less dense mesh with well constructed elements. Therefore, it is the job of the finite element analyst to find the best medium between mesh density, element size and shape, and overall mesh effectiveness.

It is important in finite element analysis, as in any numerical method, to minimize the relative error between iterations. Convergence testing is performed by taking data at varying degrees of mesh density at specific node locations or at all locations in the model geometry and determining the relative approximate error in the results from one density to the next. As mesh density increases, assuming that no error is introduced by improperly shaped or generated elements or other variables, the absolute relative error should tend towards zero which would suggest the solution is converging to one value. This is the true value, and could only be achieved with a theoretical infinite mesh density or with an exact analytical solution. Since most geometries in the real world are far from ideal to model analytically, a finite element solution is often the only viable solution.

One type of convergence analysis was conducted by Collier (2004) in the appendix of his MS thesis. The temperature, stress or any other degree of freedom reliant on mesh density at a node can be represented by Equation 5.

$$R_N = A + \frac{B}{N^\alpha}$$

Equation 5 Convergence equation for finite element analysis.

R_N represents the value to test the convergence of (stress, temperature, etc), A represents the theoretical value assuming infinite mesh density, N represents the number of nodes, and B and α are constants to be determined. Three different mesh densities

are used which range from a large element size (fewer elements) to a smaller element size (more elements). Values for stress, temperature, etc. are found from these different mesh densities and substituted for R_N. Using the number of nodes or elements as the value *N*, a system of nonlinear equations can be constructed and the unknowns A, B, and α are solved for. In order for the mesh to converge quickly, the value of α must be greater than one. A mesh may still be convergent for a value of α less than one, but this convergence is most likely to occur very slowly if at all. It is important to note however, that the variability inherent in finite element analysis often makes proving convergence in this way difficult. The number of elements should effectively double for each trial of the convergence analysis, and there are certain situations where a simple doubling of elements is no simple task and can often adversely affect mesh integrity.

Another method to demonstrate convergence was used by Berlin (2004) in his MS thesis [22]. The method is a graphical representation of convergence based on the properties of logarithms. Using a logarithmic scale on both the *x* and *y* axis, data of the output vs. mesh density is plotted. The output data is the result from the finite element analysis we seek to prove the convergence of (stress, temperature, etc.). If the line connecting these data points has a slope close to zero (flat line), it can be assumed that the mesh is convergent. This method also has limitations, however, as the difference in mesh density from one trial to the next should be reasonably close to one order of magnitude larger than the previous trial (10, 100, 1000, etc). If this is true of the data being represented, then this method is a good indicator of mesh convergence.

If all else fails, a good rule of thumb is to calculate an absolute relative approximate error of less than five percent from solutions with the two highest mesh

densities. Derivations of less than five percent are generally acceptable as they will normally not affect critical parameters such as stress ratios by a significant amount.

In general, convergence was very difficult to definitively prove in this work. All of the previously mentioned methods were used at some point to prove convergence. In many situations, changes in mesh integrity due to an increase in mesh density for the convergence analysis caused some meshes to yield inaccurate results. In the meshes of AP1 and AP2, it is very difficult to gain complete nodal continuity due to the irregular geometry of the gusset. This irregular geometry means that only a small number of nodes will be able to be merged across the hub-gusset and the hub-flange interfaces. This often caused stress singularities at these locations, and made convergence very difficult to prove. However, temperature was consistently convergent and produced good results on almost every trial. A further discussion of the convergence analyses performed will follow in each subchapter for the assembly procedures.

4.7 Assembly Procedure 1

The third step of this assembly procedure has been shown to be the most critical step and is characterized by the dipping of the TH assembly into liquid nitrogen. The geometry for the hub and trunnion was taken from previous works and was detailed in Chapter 3. This model is simulated in ANSYS by creating cylindrical volumes of the trunnion and hub geometries respectively and applying a convection load on the appropriate exterior areas. An interference stress is applied by specifying a slightly larger outer radius for the trunnion. As the trunnion reheats to a steady state temperature inside the hub, the outer radius of the trunnion pushes out on the inner radius of the hub, which

generates the interference stress. Figure 12 shows the basic volumes of the TH assembly used for AP1.

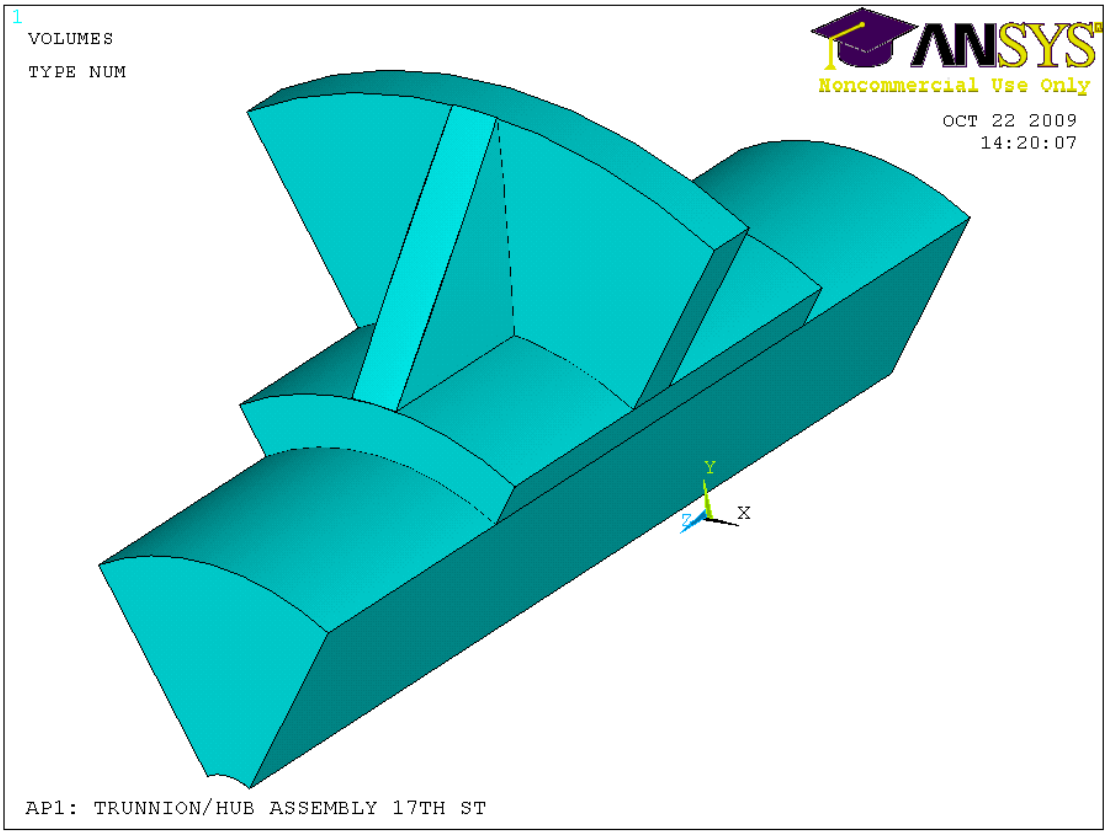

Figure 12 Basic finite element model used for AP1.

To model the interference between the hub and the trunnion, contact elements were used. The description of these elements was given in a previous subchapter. The area of the inner hub radius is considered the target area and the area of the outer trunnion radius is considered the contact area.

4.7.1 Meshing Scheme

The primary goal of the meshing scheme used for AP1 was to help improve the model of Nguyen (2006) by increasing the number of merged nodes at any applicable volume interface as this was an issue brought up by his thesis committee in 2006.

Initially, full nodal continuity was achieved by creating a model with thirteen separate volumes which allowed for precise control over the mesh at every volume interface resulting in perfect nodal continuity throughout the entire model. Further details of this model will follow in AP2 as its primary purpose was for this assembly procedure. This model, however, was met with problems when attempting to solve the contact problem. Certain volumes at the TH interface were "digging in" more than others and were accepting all the stress of the contact and not distributing it evenly throughout the entire volume as would be the case in practice. This prompted the creation of another model which used only one volume for the hub inner diameter. This allowed for accurate contact behavior to be obtained and eliminated the problems of the previous model. The only drawback of this new model was that complete nodal continuity was now impossible to obtain due to the irregularity of the gusset geometry.

The final model was able to create perfect nodal continuity between the hub and flange volumes however, as well as align the nodes between the hub and the trunnion allowing for improved contact behavior. Since the smallest common denominator of length was 0.25 inches, the length of the hub, trunnion and the width of the flange were divided by 0.25. This created element divisions which line up perfectly with one another allowing for complete nodal continuity. Figure 13 shows the mesh used by Nguyen (2006) in his masters thesis. The main point to notice is the lack of nodal continuity between the hub and the flange and the hub and trunnion. The nodes between the hub and trunnion are not as critical, as the contact between these two geometries is not strictly dependent on perfect nodal continuity. However, the interface between the hub and the

flange is more important as improved nodal continuity in this area will allow for a more continuous stress and temperature distribution.

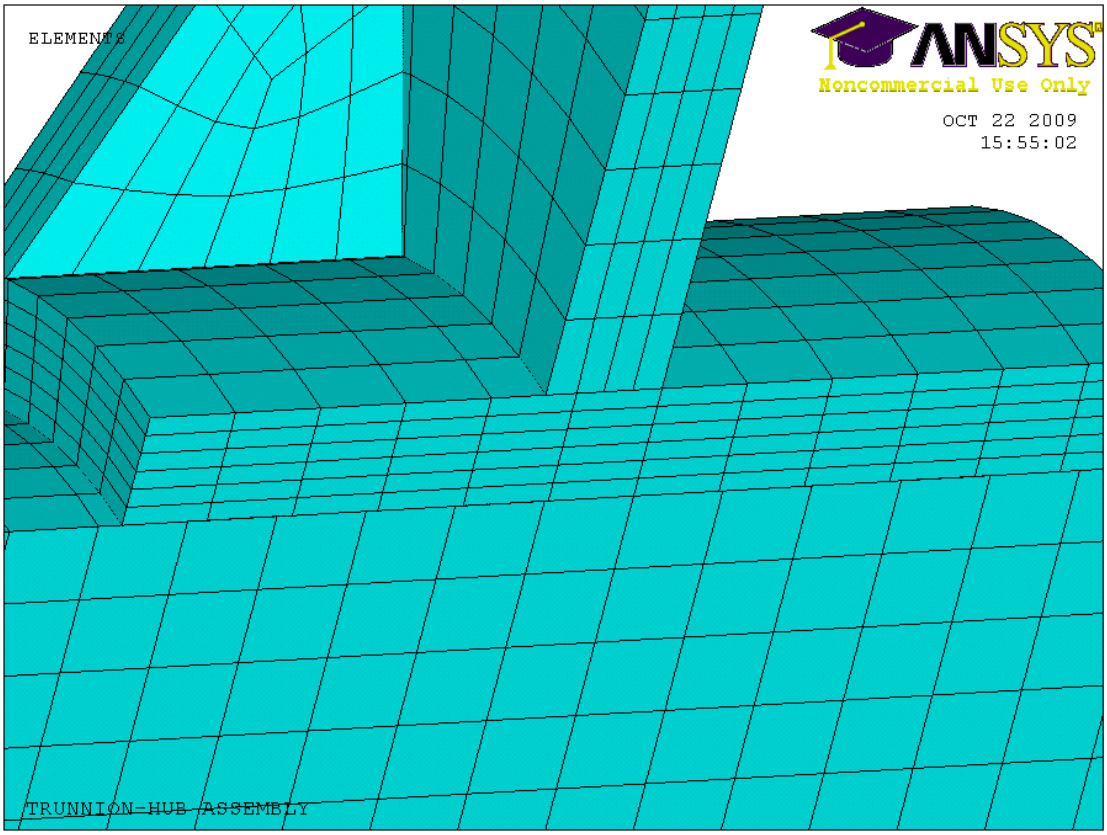

Figure 13 Mesh used by Nguyen (2006) for AP1.

Some other changes were made to the model constructed by Nguyen (2006). One such change was the addition of a mesh that changed with the model geometry. As the AASHTO alpha ratio is increased in this model, the hub outer diameter increases effectively increasing the overall thickness of the hub and reducing the size of the flange. The difference in length between the flange outer radius and the hub outer radius is calculated for each change in alpha, and this value was divided by 0.25. This method helped to keep some of the elements in the gusset from being distorted.

This new model allowed for more nodal continuity between the hub and flange volumes as well as ensured an accurate contact analysis between the hub and the trunnion. Boundary conditions and loads are applied in exactly the same manner as in the work of Nguyen (2006). Figure 14 shows the new model used for AP1.

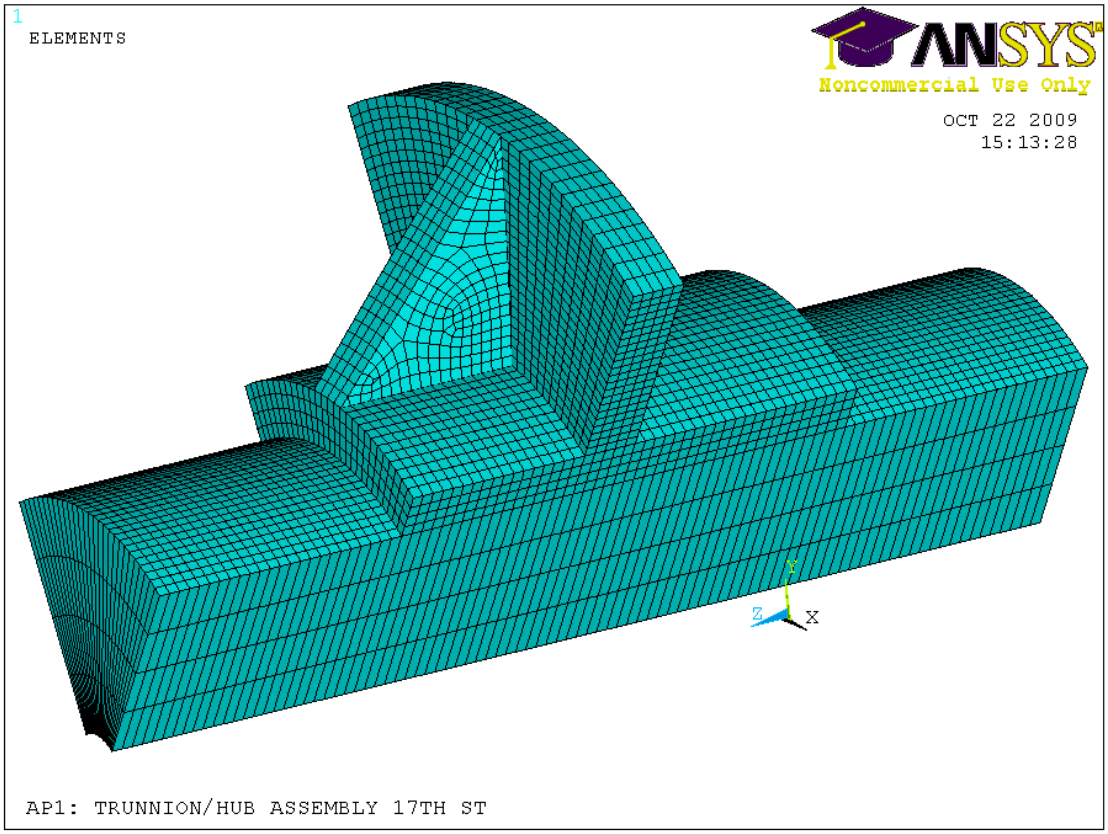

Figure 14 Meshing scheme used for AP1 in current work.

4.8 Assembly Procedure 2

Previous studies offered insight into the critical steps of AP2 with details on maximum hoop stresses, and maximum Von Mises stresses induced in the materials during the cooling procedure [2]. Although these studies did provide some useful information with regard to these factors, it still remained to fully understand the significance of the cooling methods, AASHTO alpha ratios and variations in hub

geometry on the OMCCL and the OMSR. A full sensitivity analysis was needed to gain a complete understanding of how these variations affected these design parameters.

4.8.1 Model Accuracy

In the previous work of Nguyen (2006), one issue addressed by the thesis committee was the lack of continuity between elements and nodes in his model. For a more accurate solution, it was suggested that a greater uniformity be achieved through either an alternate meshing scheme or element which would allow for the proper merging of nodes at all appropriate locations in the geometry. Figure 15 below shows some locations of unmerged nodes in Nguyen's model.

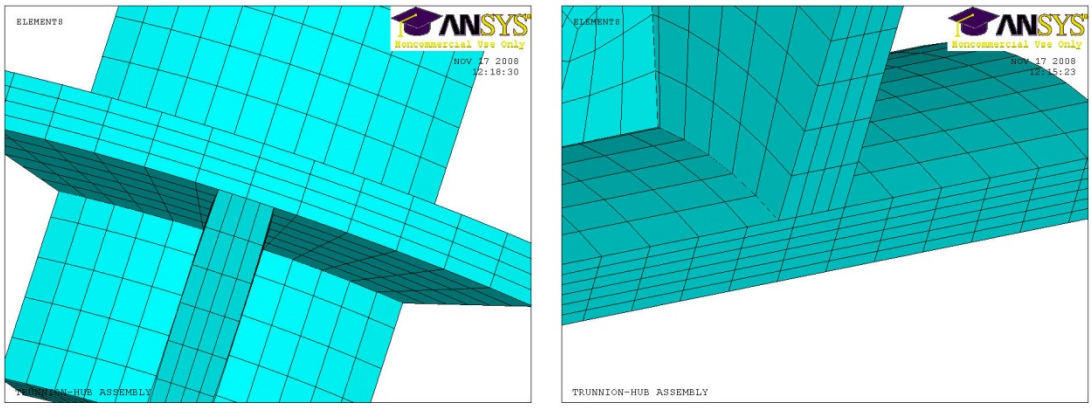

Figure 15 Finite element model of hub for AP1 produced by Nguyen (2006).

The major difficulty in creating nodal continuity in this model is the gusset volume. This volume is meshed with respect to a Cartesian system, and the hub and flange are meshed with respect to a cylindrical coordinate system. One solution to this problem was to divide the model up into many different volumes at appropriate geometrical boundaries such as the distance from the front of the hub on the gusset side to the beginning of the flange (LF). This allows for complete control for the analyst over

how each volume is meshed, and since each volume shares adjacent areas, the mesh at those areas must be the same, thus ensuring nodal continuity.

If breaking the geometry up into several different volumes is not an option, a general solution to this problem can be found using a mathematical algorithm relating the ratio of the length of two specific lines in the geometry to the ratio of the corresponding number of elements in these lines. A relationship can be drawn between these two factors, as each respective line is simply the addition of smaller lines represented by the edge length. Assuming that each line uses the same element edge length, we can then solve for the number of line divisions needed using an iterative program which can be constructed in any programming language (MATLAB, Mathematica, Maple, etc.). Figure 16 illustrates the concept. For a vertical meshing scheme, any given line lengths *A* and *B*, or *C* and *D*, there will exist an edge length such that the number of divisions created in *D* will match up with edge lengths created in *C* to some pre-specified tolerance.

This logic can be applied to any two line lengths, but it is important to note that this method is limited as there are a finite number of combinations that can make the ratio true. This fact, when coupled with the limitations on the number of nodes able to be used by ANSYS, allows for less flexibility in mesh generation. This is naturally made much easier if there is a relatively simple common denominator of length that exists between dimensions. Figure 17 illustrates this concept.

A pre-specified tolerance is entered by which the distance between nodes must be less than in order for the program to stop running. This tolerance can subsequently be used in the APDL code as the meshing tolerance.

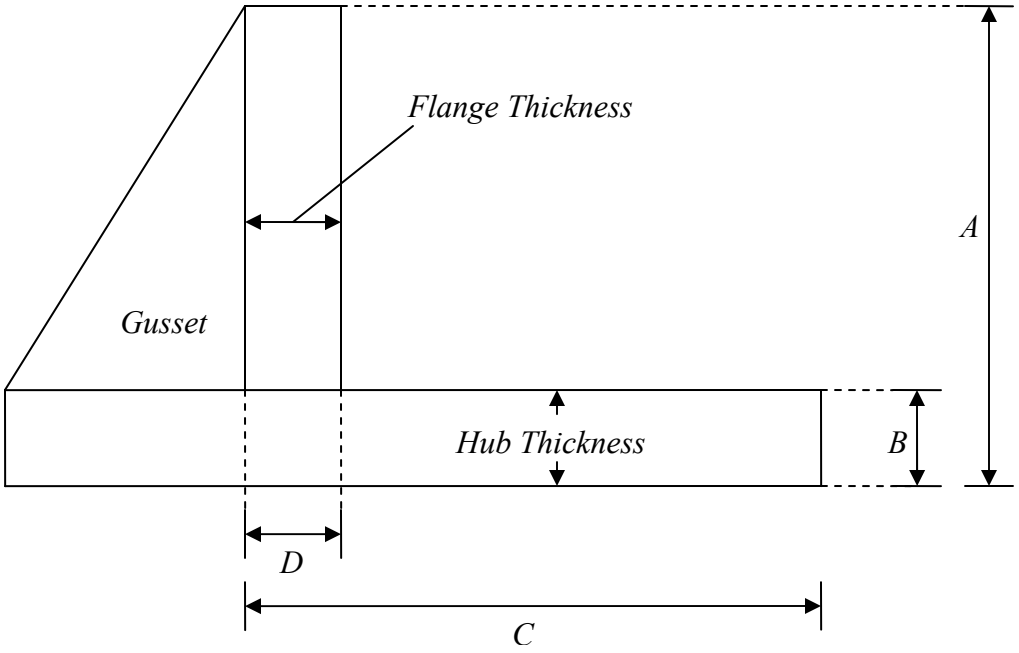

Figure 16 Schematic of iterative meshing scheme used for AP2.

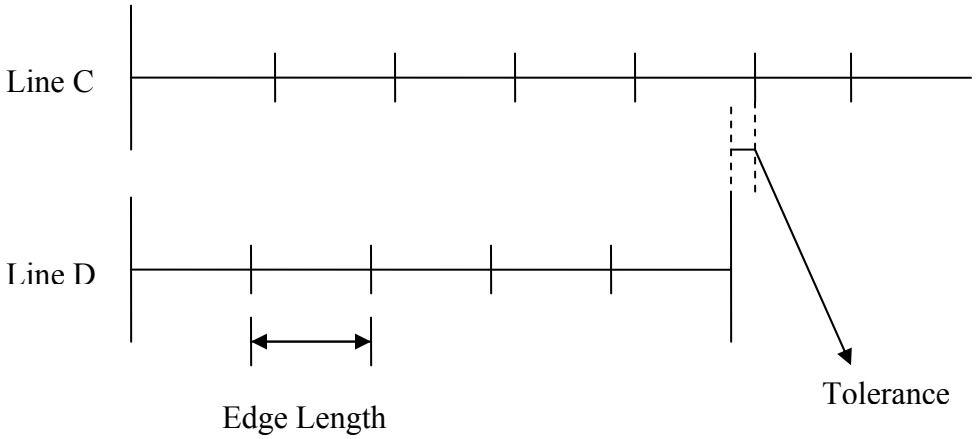

Figure 17 Close up view of element edge lengths in Line C and Line D for horizontal meshing scheme.

In the current analysis, the use of this iterative program was somewhat unnecessary as all dimensions for the horizontal meshing scheme described above divided evenly into each other. In most cases, an edge length of 0.25" allowed for perfect

merging between nodes on all surfaces. Smaller edge lengths were also able to be used by divided the edge length by a factor of two or more.

The model used by Nguyen (2006) was composed of four separate volumes—a cylindrical volume for the trunnion, a cylindrical volume for the hub volume, a cylindrical volume for the hub flange, and a triangular volume for the gusset dimensions. To create perfect nodal continuity, the three volumes used by Nguyen (2006) representing the hub and flange geometries were subsequently divided up into twelve separate volumes—nine volumes for the hub, and three volumes for the flange. With the addition of the gusset volume, a total of thirteen volumes were generated in this model. This modeling technique allowed the mesh to be precisely controlled. Figure 18 below shows the meshing scheme created using this modeling scheme. As seen in Figure 18, nodes are able to be merged at all locations between all surfaces creating much greater model continuity.

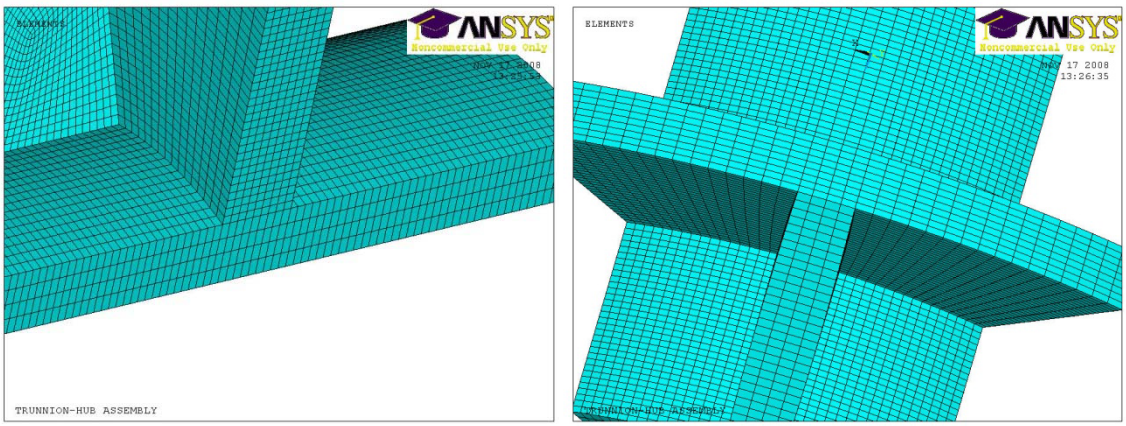

Figure 18 Improved finite element meshing scheme for study of AP1 and AP2.

To perform a convergence analysis, an initial starting number of line divisions are chosen at specific places in the geometry. This number is subsequently multiplied by a

"mesh factor" which is nothing more than a multiplier used to increase the number of divisions by a set amount. As the mesh factor increases, so must the number of divisions for each line increase, which yields more elements and nodes. Although this model did produce very good temperature and stress distributions throughout the material, it was very difficult if not impossible to prove convergence for this model. For reasons unknown, the stress plots showed irregular behavior with regards to convergence, even though the temperatures were very often convergent. Figure 19 shows the maximum hoop stress at any point in the model versus the number of nodes in the model at the same time. As seen from this figure, convergence is not definitively proved.

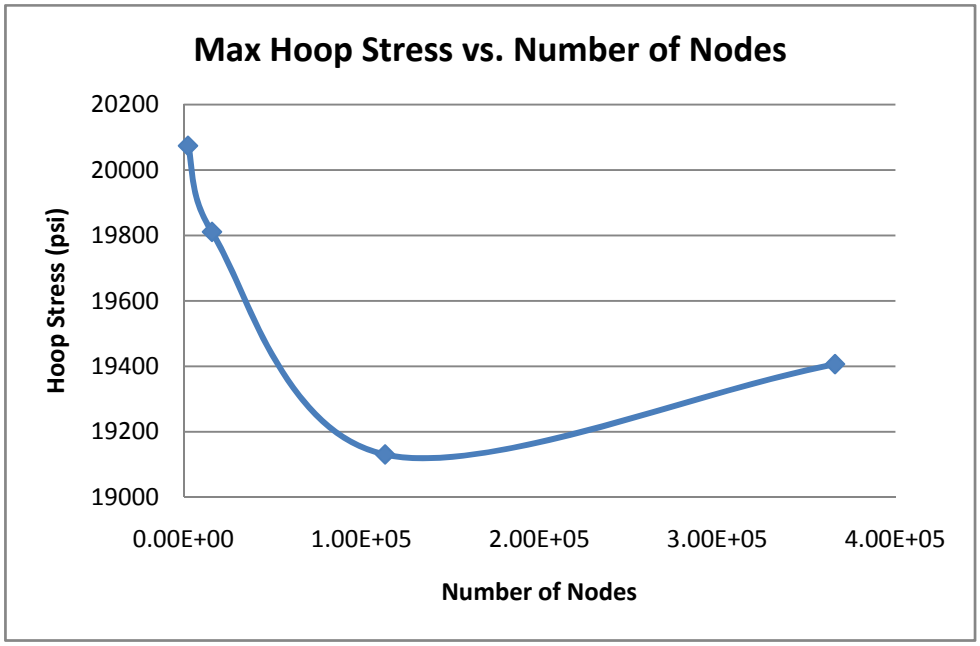

Figure 19 Max hoop stress at any point vs. number of nodes for thirteen volume model for AP2.

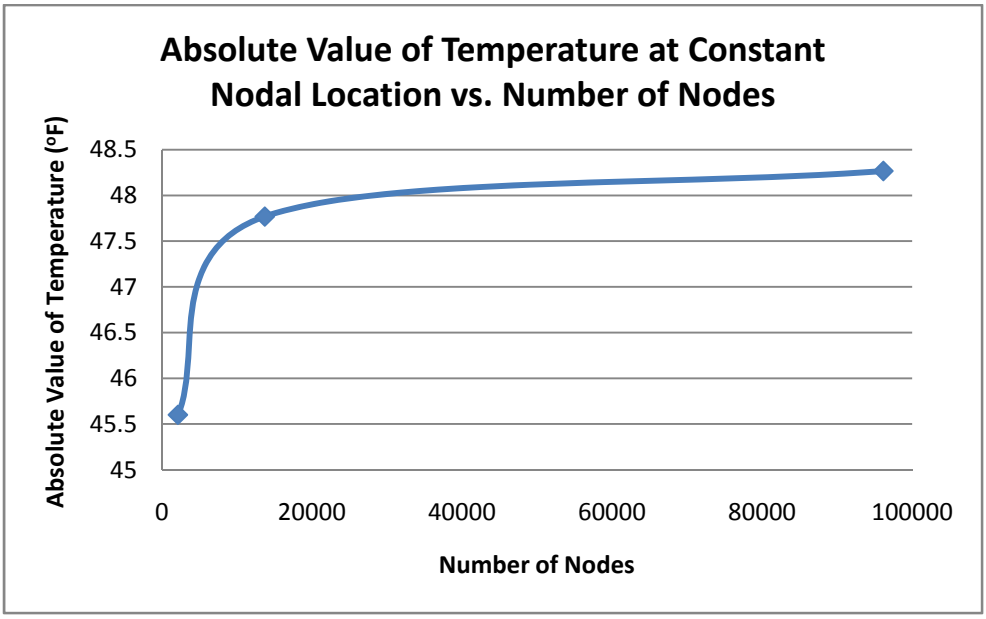

Figure 20 Absolute value of temperature at constant nodal location vs. number of nodes.

Figure 20 shows the absolute value of temperature at the same nodal location on the right hand side of the flange centered vertically and horizontally. This plot certainly shows convergent trends but this is not the case with regards to the hoop stress. As all stress in this problem is thermal stress, it is reasonable to assume that if the temperature is consistently convergent, then the model itself is producing valid data with regards to stress even if these values are not necessarily convergent.

The mesh that was used to take data corresponds to the second point on the hoop stress and temperature plots. This point was chosen because it was more convenient computationally speaking and was within a slight margin of error (in terms of temperature) to the next highest mesh density. Also, this model produced stresses close to experimental stresses measured in previous studies [2,3]. Furthermore, this model had

little if any problems with stress singularities or poorly shaped elements. The continuity of the nodes from one volume to the next helped to drastically reduce these problems.

4.9 Assembly Procedure 3

To ensure that the critical step of AP3 was the third step—dipping the trunnion into liquid nitrogen, a finite element model was constructed to simulate the heating of the girder and a 60"×60"×0.75" flat steel plate. This follows the work done by Berlin (2004) who used both a finite element model and experimentation to demonstrate the feasibility of AP3. Berlin conducted an experiment whereby he placed induction heating coils spaced evenly around a central hole in an ASTM A36 60"×60"×0.75" flat steel plate. An insulating fiberglass blanket was then placed overtop of the coils and the entire assembly was heated to approximately 500°F. This heat load generated sufficient thermal expansion in the material to allow for a clearance of 0.002125" which was sufficient for the insertion of the hub component based on FN2 interference fit criterion. Full scale testing on an actual girder was not performed due to the limitations of cost and availability.

To verify his experimental results, Berlin used a finite element model constructed in ANSYS simulating the full girder dimensions as well as his experiment on the flat steel plate. These finite element models were duplicated for this thesis to assure that the results were accurate and to verify the earlier assumption that the first step of AP3 was not a critical step in the assembly procedure. It was also necessary to verify the assumption that the second step of AP3 was not a critical step of the assembly procedure. This was accomplished by modeling the hub in addition to the original plate model, and

analyzing the contact problem involved with the insertion of the hub into the heated plate. It is assumed that the stresses developed in the plate model will be very close to the stresses developed in the girder model and so as such, the girder is not modeled in this work. With the verification of these assumptions, it can be reasonably deduced that the step of AP3 with the greatest likelihood for failure is the third step—insertion of the trunnion into liquid nitrogen.

4.9.1 AP3: Model 1

This model was used as a reference to the actual bridge girder to get a more complete idea of the displacements and stresses associated with the heating of the girder. Much of the modeling and meshing techniques, as well as the contacts generated from this model were used as a template for the full girder and were considered to be comparable. The addition of the hub was a significant contribution to this work and allowed for a clearer perspective on this assembly procedure as a whole. The model consisted of four components:

1. 60"×60"×0.75" ASTM A36 mild steel plate. This is the most commonly used structural grade steel in bridges and buildings. This was modeled in ANSYS as a 60"×60"×0.75" volume with a central hole with a radius of 7.7664" which matched the dimensions of the 17th Street bascule bridge hub outer radius for $\alpha = 0.1$. Circular volumes were created in the plate itself to match with the adjacent coil volume positions directly above the plate. Figure 21 shows the plate volume as generated in ANSYS.

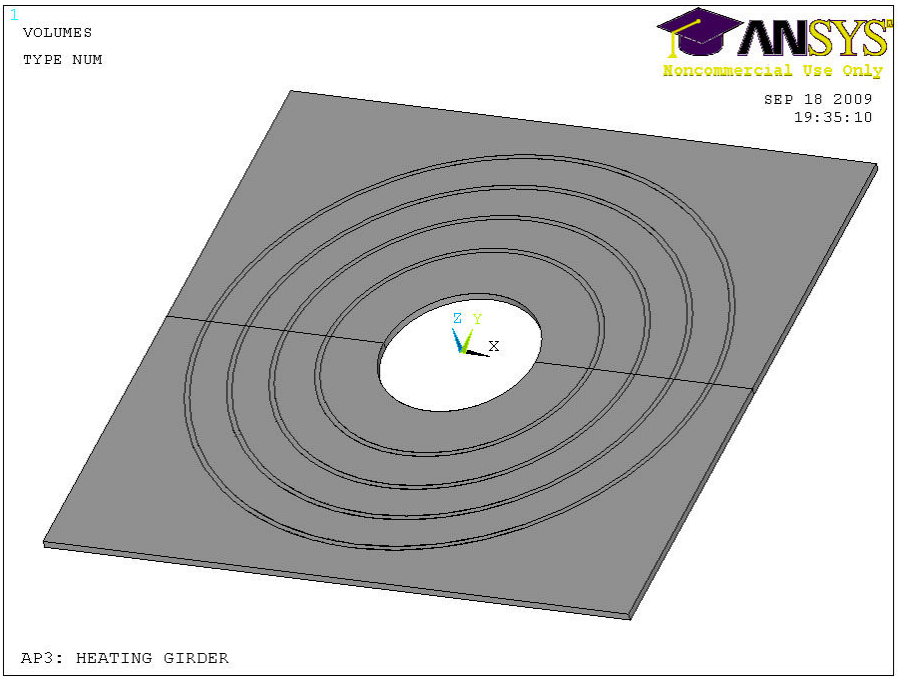

Figure 21 Finite element model of plate volumes for AP3.

2. Four 0.5"×0.5" ceramic induction coils. These were volumes with a square cross section that were modeled around the perimeter of the hole at specific locations on top of the plate. The coils were modeled as a single piece of ceramic material, although the actual coils are comprised of an inner core of copper and an outer coating of ceramic material. It was assumed that all heat transferred into the plate would be transferred through the ceramic, and adding the copper core to the model would not have greatly affected the model accuracy. It is also important to note that the actual coils used during experimentation had a circular cross section, which would have somewhat different heat transfer properties than the square cross section used for the finite element model. This difference was omitted however, to help reduce the overall model complexity. The orientation of these coils with respect to the central hole was circular for the given test, although a

square orientation is also possible. This circular configuration was chosen mainly to help create unification between the hub elements and the elements of the plate. It is reasonable to assume however, that a different coil orientation would not affect the thermal stresses and thus the OMCCL and OMSR dramatically. Figure 22 below shows the plate volume with the addition of the ceramic coils on top.

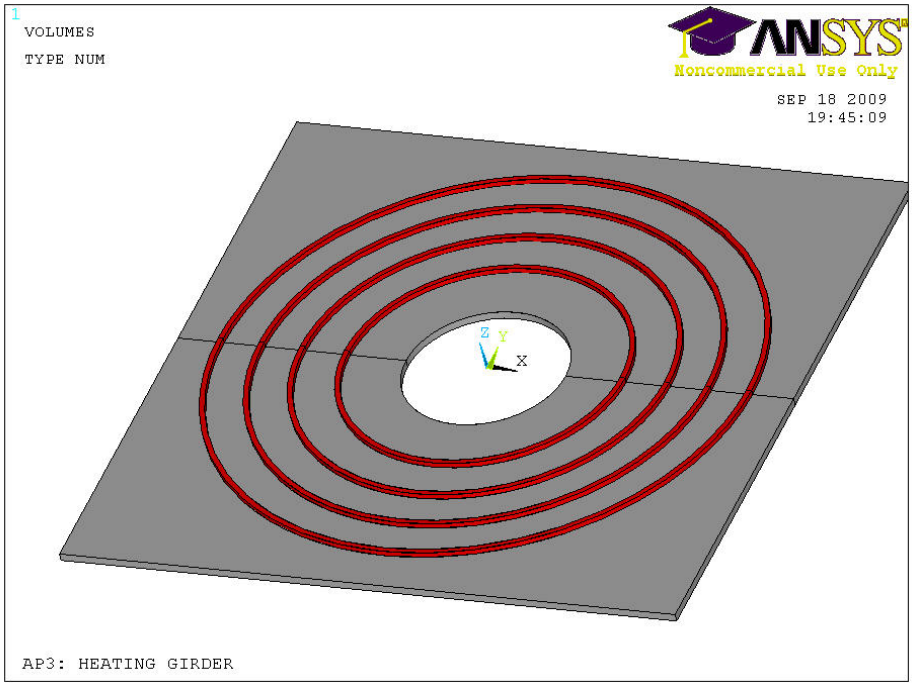

Figure 22 Finite element model of heating coil volumes and plate for AP3.

3. The third component to this model is the air volumes that were modeled in between the coil volumes. This was done to ensure optimum model accuracy as the experimental model would have contained air in these locations. It was reasonably assumed that any heat transfer taking place by a natural convection cycle in these volumes would be nonexistent or negligible compared to the more dominant conduction mode of heat transfer. It was therefore assumed that these volumes were purely a conductive medium, and offered no convective mode of

heat transfer. Figure 23 shows one side of the purple air volumes between the coil volumes.

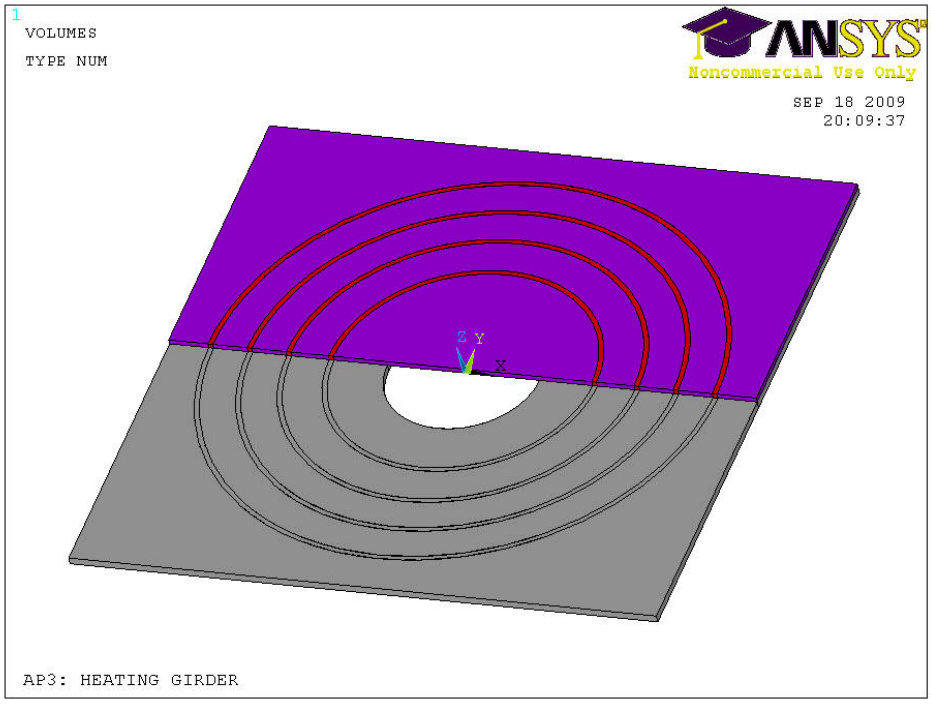

Figure 23 Finite element model of air volumes and air volumes with coils and plate respectively.

4. 60"×60"×4" fiberglass insulating blanket. This volume was modeled directly on top of the air/heating coil volumes and comprised the final top layer of the model. Separate volumes were created in the fiberglass itself to match up exactly with the air and coil volumes directly below the fiberglass volumes. This was done to ensure perfect mesh continuity between volumes. Figure 24 shows half of the fiberglass volumes with the air, coil, and plate volumes respectively.

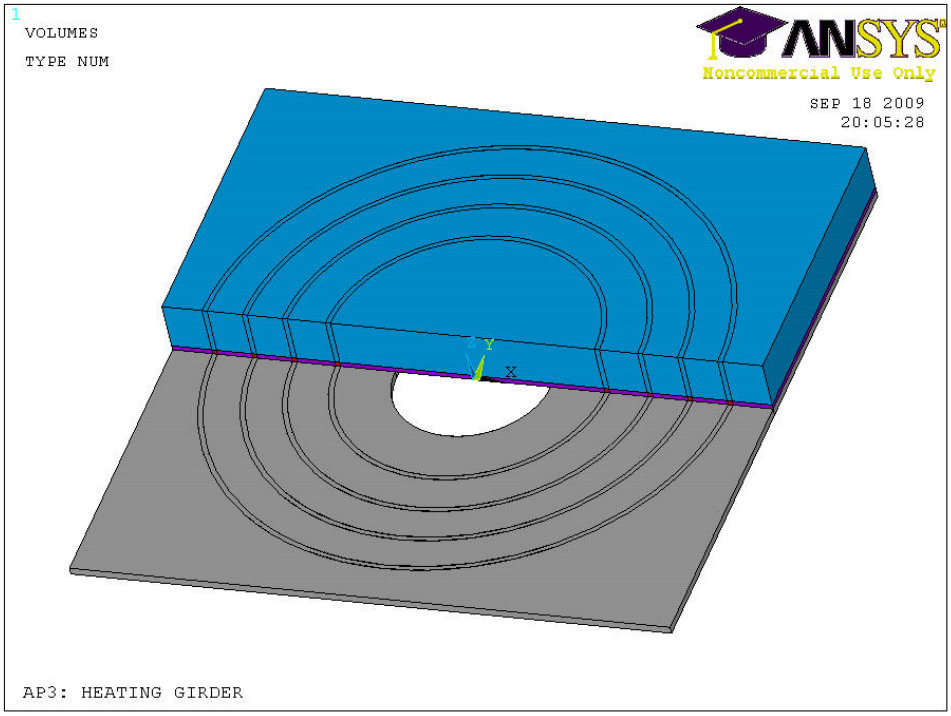

Figure 24 Finite element model of half of fiberglass volumes with plate, coil, and air volumes respectively.

All volumes in the model were divided up along the *x*-axis along the plane $y = 0$. The primary reason for this was to make meshing the model easier and allow for precise control of all meshing along the border between the adjacent sets of volumes.

All volumes were meshed by sweeping a mapped meshing scheme from a source to a target area. These source and target areas were chosen by ANSYS after specific line divisions were specified for each individual volume. Circumferential and radial divisions were specified for each volume, as well as divisions along the *z* direction. Figure 25 shows the top view of the model fully meshed.

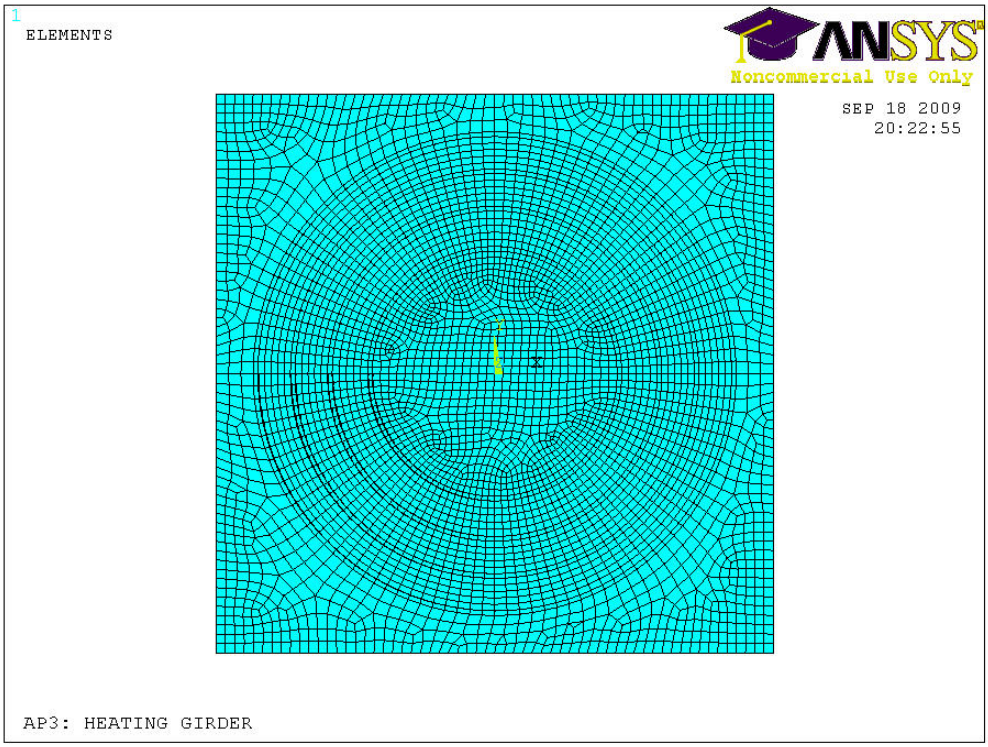

Figure 25 Top view of finite element mesh generated for Model 1 of AP3.

Additional mesh density was added to the plate volumes directly around the hole where the hub comes into contact with the plate in the second stage of AP3. The mesh in the hub was generated to match the mesh of the plate exactly as to attain a high level of accuracy for the thermal contact analysis. Figure 26 shows the meshed plate volumes.

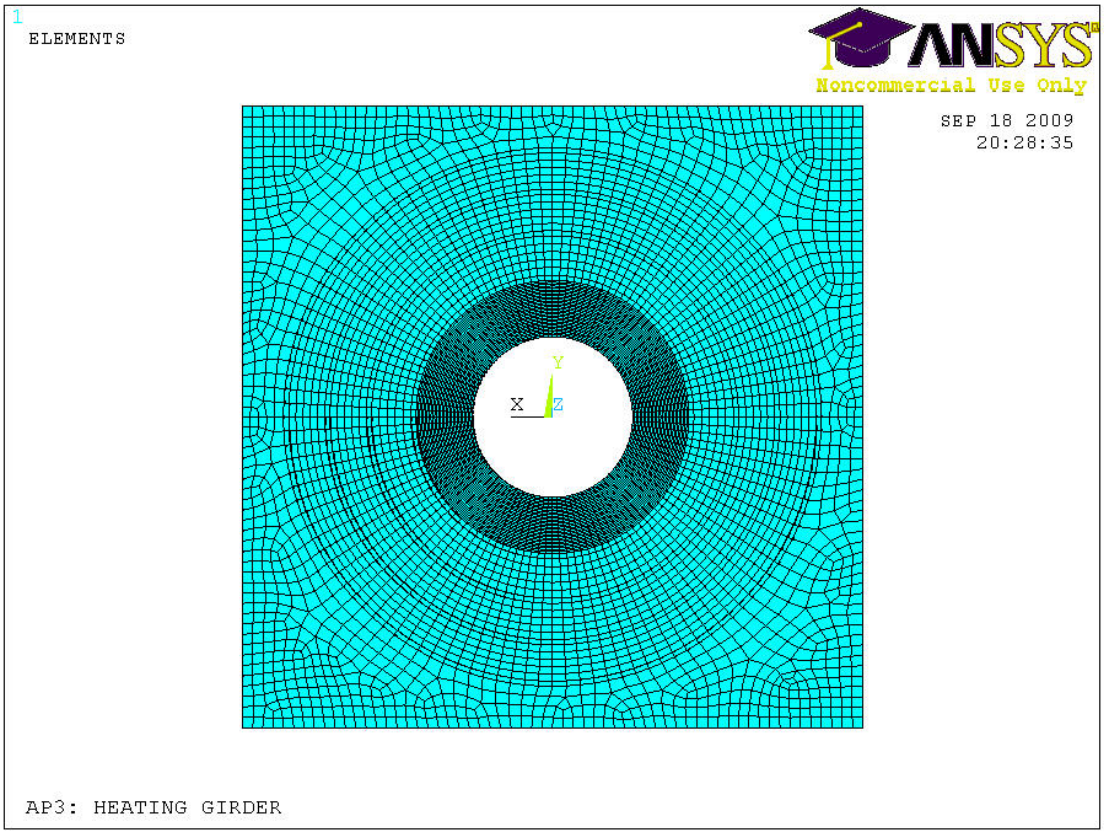

Figure 26 Meshed plate volumes for Model 1 of AP3.

To verify that the second step of AP3 was not a critical step in the assembly procedure, the hub was modeled in addition to the girder and plate models. It is important to study the contact analysis of these components as it has not yet been addressed in previous works or experimentally studied. Basic hand calculations using elasticity equations can yield some idea as to the steady state interference stresses, but it is the combined interference and thermal stresses that will contribute to failure. As these components cool towards a steady state temperature, thermal gradients will be induced in the material immediately as the hub will be inserted at room temperature, and the girder and plate will have a temperature distribution associated with the heating process.

4.9.1.1 Loading and Boundary Conditions

A heat generation load of $\dot{q} = 3.75 \ \text{BTU}/(\text{min} \cdot \text{in}^3)$ was applied to the ceramic coils as specified by the work of Berlin, and was heated for 90 minutes to a maximum temperature around 500°F. The material properties for the thermal conductivity of air, as calculated by Berlin (2004), are specified as a function of temperature and are shown in Table 3. These convection coefficients were applied to the exterior of the model. The "Top" convection coefficient was applied on the top areas of the model on the plane $z = 5$—i.e. the top of the fiberglass volumes. The "Side" coefficients were applied to all areas on the planes $x = 30$, $x = -30$, $y = 30$, and $y = -30$ respectively. These areas were part of all components of the model—fiberglass, air, and plate volumes with the exception of the coils. The "Bottom" convection coefficient was applied to all areas of the model on the plane $z = -0.75$—i.e. the bottom of the plate.

Table 3 Convection coefficients as a function of temperature for plate model.

Temperature, $^\circ$F	Sides $\frac{\text{BTU}}{\text{min} \cdot \text{in}^2 \cdot {}^\circ \text{F}}$	Top $\frac{\text{BTU}}{\text{min} \cdot \text{in}^2 \cdot {}^\circ \text{F}}$	Bottom $\frac{\text{BTU}}{\text{min} \cdot \text{in}^2 \cdot {}^\circ \text{F}}$
70	2.5984×10^{-6}	0	0
102	9.3211×10^{-5}	9.3212×10^{-5}	3.6494×10^{-5}
210	1.2808×10^{-4}	1.4071×10^{-4}	5.0630×10^{-5}
354	1.5417×10^{-4}	1.7260×10^{-4}	6.1015×10^{-5}
714	1.6672×10^{-4}	1.7946×10^{-4}	6.6011×10^{-5}

The boundary conditions that were applied were identical to those used by Berlin (2004) with the exception that for the model used in this thesis, the bottom of the plate was modeled at $z = -0.75$ as opposed to $z = 0$. These boundary conditions are given by Equation 6 to Equation 8.

$$U_x(x = -30) = 0$$

Equation 6 Boundary condition 1 for first AP3 model.

$$U_y(y = -30) = 0$$

Equation 7 Boundary condition 2 for first AP3 model.

$$U_z(z = -0.75) = 0$$

Equation 8 Boundary condition 3 for first AP3 model.

Model 1 was heated for 90 minutes in 3 minute intervals. Figure 27 shows the temperature profile in the plate generated after 3 minutes into the heating process.

A MATLAB program was written to determine when adequate clearance is generated in the plate to allow for the insertion of the hub. Radial displacements were taken at nodes around the hole perimeter at 0 and 180°, and at 90° and 270° respectively. These displacements were used to calculate diametric and radial clearance values based on FN2 fit specifications. The diametric clearance required was calculated as 0.0085785". An additional 0.01 inches is added to this measurement to allow for some play in the assembly process making the required diametric clearance 0.0185785". Also, an additional 25% was added to this clearance just to account for any errors in the finite element program and to again add in a factor of safety for the analysis. Thus the total diametric clearance was calculated as 0.023223". For Model 1, it was determined that sufficient clearance is generated in the plate hole at 42 minutes into the heating process. As this program assumes that radial displacements around the hole will take place evenly, and that no distortion in the hole will occur, it is reasonable to assume that more heating may be necessary in actual practice.

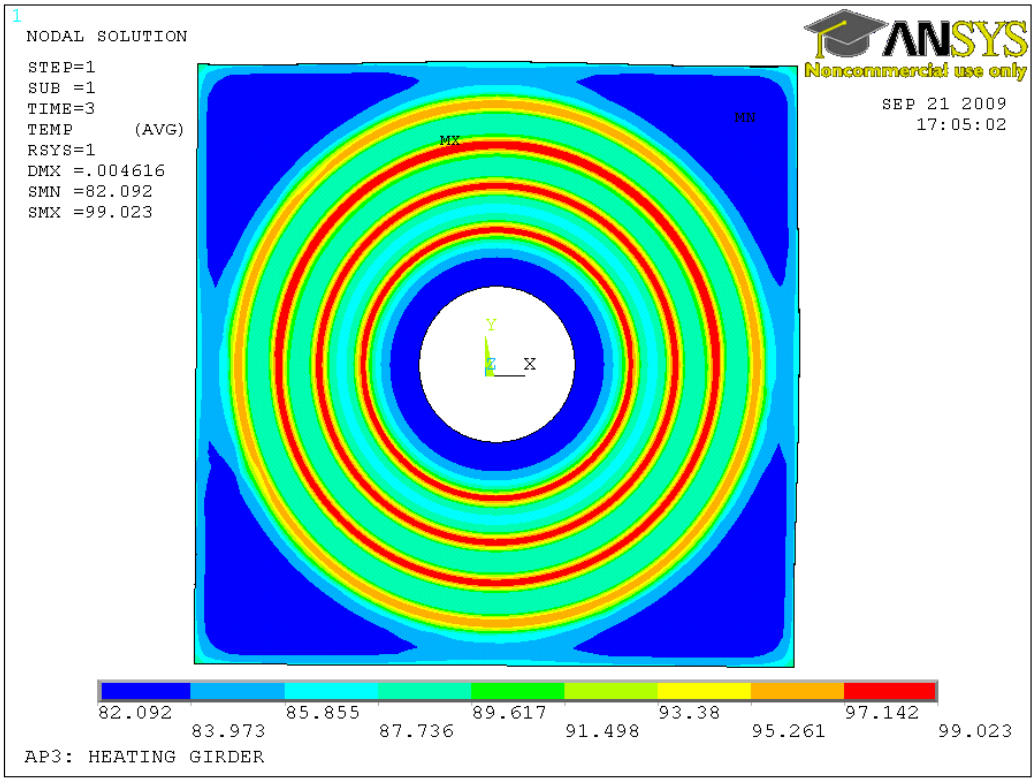

Figure 27 Temperature profile of plate volumes in Model 1 of AP3.

4.9.1.2 Results: Heating Model 1

Data for each time step was output to a text file and was evaluated using a different MATLAB program. The tensile (positive) hoop stress and Von Mises stresses in the plate for each time step were evaluated and are shown in Figure 28. Only the tensile hoop stresses were considered, as compressive (negative) hoop stress tends to close cracks and not open them. The maximum recorded hoop stress for the heating process was 22.427 ksi and the maximum Von Mises stress was 22.598 ksi.

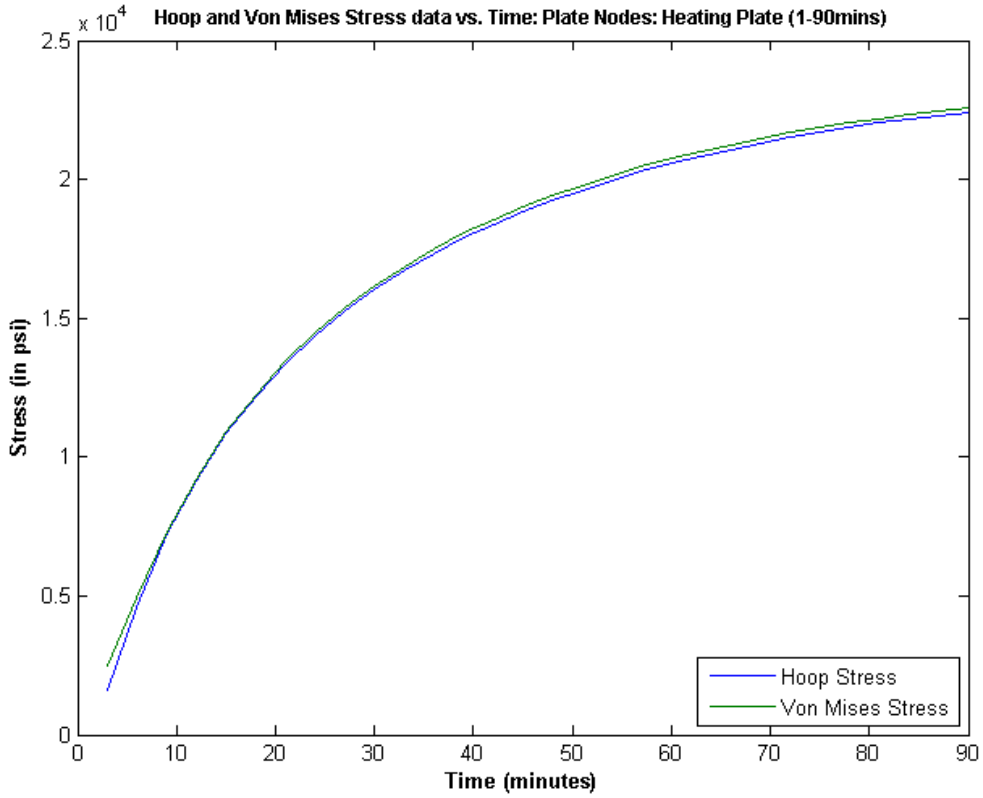

Figure 28 Hoop and Von Mises stresses vs. time for plate nodes in Model 1 of AP3.

Since the fracture toughness of ASTM A36 steel increases with an increase in temperature, the value of fracture toughness at room temperature (47 ksi) was constant in the calculation of the OMCCL. Therefore, the value of the highest hoop stress will produce the smallest critical crack length. From these observations, it is reasonable to assume that the OMCCL values will be large for this step of the assembly procedure as an applied heat load will tend to close cracks rather than open them. It was necessary to determine this firsthand however, and the lowest calculated OMCCL value was 2.9911" calculated at $t = 90$ minutes into the heating process. The temperature at the node where the OMCCL was calculated was $465.18^{\circ}\mathrm{F}$. Figure 29 shows the calculated critical crack lengths for every time step for all nodes in the plate.

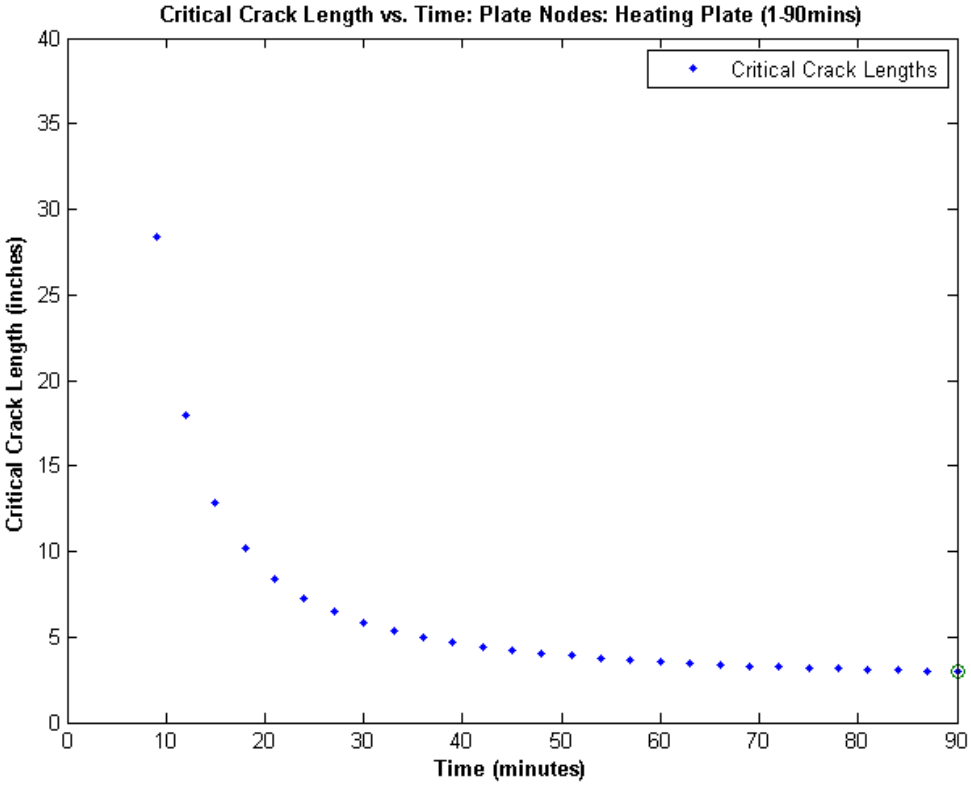

Figure 29 Critical Crack Length vs. time data for plate nodes in Model 1 of AP3.

As seen by the trend of the data in the graph, if the heating process continued, this could potentially create a lower critical crack length if heated for too long. This is inconsequential however, as sufficient expansion is generated between 40-50 minutes of the heating process depending on plate dimensions, coil generation rates, etc. and as such, it will never be necessary to heat beyond this point. Therefore, it is reasonable to assume that the critical crack lengths will not be small and thus failure via crack propagation is unlikely in the heating portion of AP3 for Model 1.

The yield strength of most steels decreases with an increase in temperature so there is a greater likelihood that failure will occur via yielding when the material is being heated. Therefore, it was necessary to calculate the value of the yield strength as a

function of temperature for all nodal temperatures at all time steps. The yield strength values of mild steel as a function of temperature at a 0.2% strain rate were used to calculate the yield strength for any given temperature in the assembly process [27]. Cubic spline interpolation was used to calculate values in between existing data points.

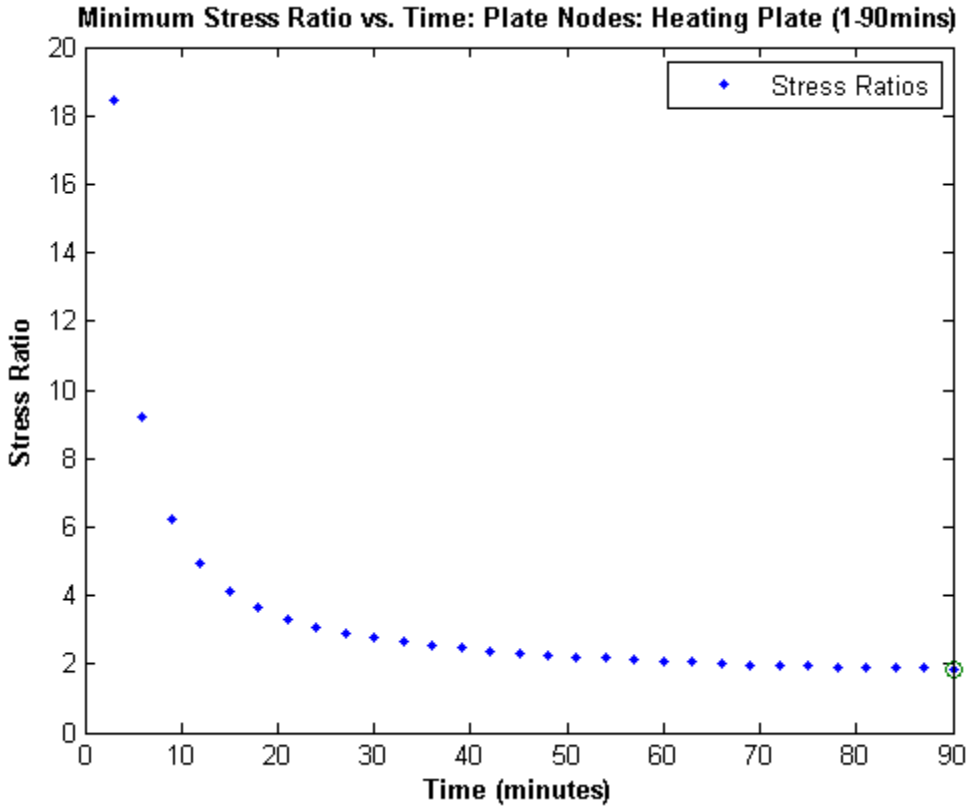

Figure 30 Stress ratio vs. time data for Model 1 of AP3.

The value of the stress ratio was calculated at every nodal location for every time step in the model. The minimum of these values is defined as the OMSR and was calculated as 1.8709 at time $t = 90$ minutes in the heating process. Figure 30 shows the calculated stress ratios for every time step. The temperature of the node where this OMSR was calculated was $459.41^{\circ}\,\mathrm{F}$.

It is important to note that the plate will not need to be heated beyond the point when sufficient clearance is generated in the plate. As stated previously, sufficient clearance is generated at $t = 42$ minutes into the heating process, which reduces the likelihood for low stress ratios or stress ratios below one.

4.9.1.3 Addition of Contact Problem

One of the major contributions of this work is to model the second step of AP3—insertion of the hub into the girder hole to form the hub-girder interface—and the associated contact problem. It is necessary to determine the combined interference and thermal stresses at every time step in this stage of the assembly procedure as this combination of stresses may be more likely to contribute to component failure. As the plate is cooled, the plate contracts creating an interference fit between the hub and plate (HG interface). This process was modeled in ANSYS and the stresses and temperatures were recorded at every time step. For Model 1 of AP3, the dimensions of the 17th Street bascule bridge hub were used.

After successful heating of the plate component using the previously outlined finite element model, the fiberglass, air, and coil volumes were deleted from the assembly, much like they would be removed in actual practice. All nodal temperature data was recorded and stored in the ANSYS ".rst" file from the heating process. The radial interference calculations as per FN2 fit specifications are given in Appendix A. The plate volumes were loaded with the temperature and reaction force profile for $t = 51$ minutes into the heating process. Although it was previously shown that sufficient

clearance was generated in the plate hole at $t = 42$ minutes into the heating process, an additional factor of safety is put into the analysis by loading at $t = 51$ minutes.

The hub was then built around a cylindrical coordinate system at the center of the plate hole. Figure 31 shows the meshed hub built inside the center of the plate hole.

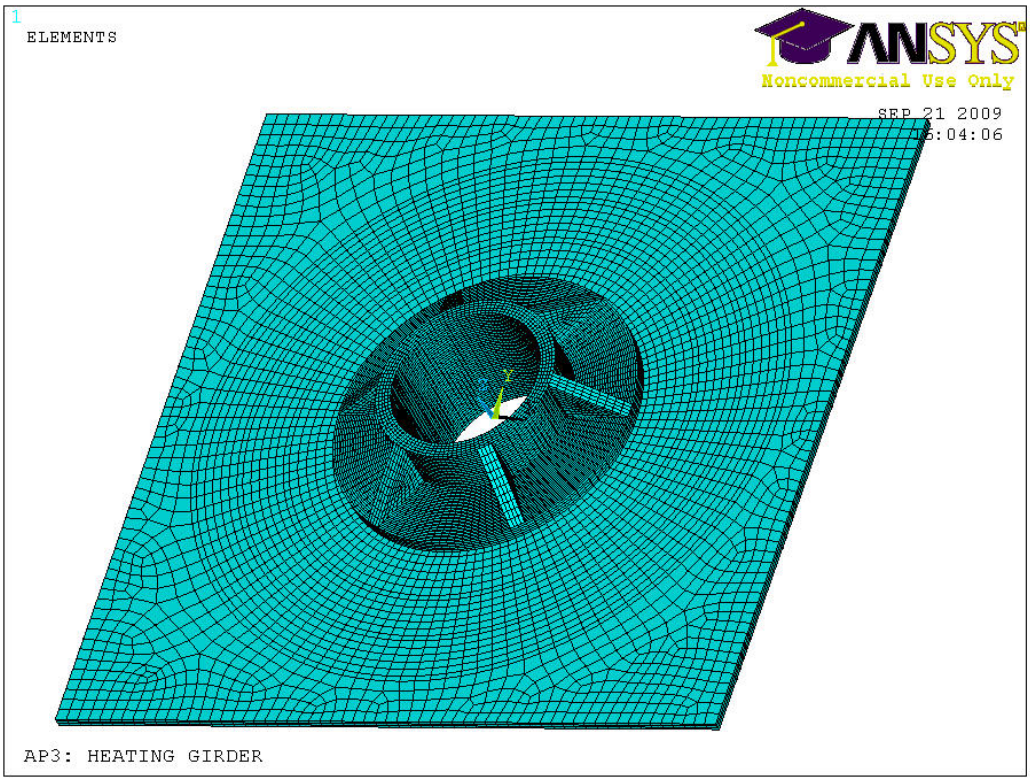

Figure 31 Model 1 of AP3 fully meshed with the addition of the hub component.

The problem involves four different contact pairs—one between the plate hole area and the outer hub diameter area, another between the hub flange and the plate, and two bonded contact pairs used to simulate the attachment of the flange volumes to the main hub volumes. The contact between the plate hole and the hub outer diameter is both thermal and structural, as interference stress will be generated in the material as the assembly cools to steady state. Minimal or no contact is made in the first contact pair,

but contact takes place immediately between the hub flange and the plate (second contact pair). The contact between the plate and the hub flange is entirely a thermal contact as no structural stresses or strains will be induced into the material. This contact directly affects the first contact pair as it alters the heat distribution in the material and thus the contraction of the hole due to cooling.

Due to the fact that the hub and flange volumes are meshed with respect to a cylindrical coordinate system and the gusset volumes with respect to a Cartesian system, it is inherently difficult to obtain perfect nodal continuity. Often times, only a section of nodes out of all the nodes in an area merge with only some of the nodes in an adjacent area, and a stress concentration occurs which skews results. To counter this problem, bonded contact pairs are created on the back sides of the gusset volumes where they meet the hub and flange volumes, respectively. These bonded contacts act as a "glue" to join one section of material to another to help increase continuity of stresses and temperatures from one volume to another.

After the contact pairs are established, the entire model is loaded with convection coefficients in the appropriate areas. The top of the plate is loaded with the "Top" convection coefficient used in the previous analysis, and the bottom of the plate with the "Bottom" convection coefficient. The hub itself is loaded with the "Side" convection coefficient as a majority of the areas on the hub are parallel with the z-axis. Although this is not entirely accurate, it can be reasonably assumed that thermal gradients induced in the hub due to the heat transfer via convection will not be significant enough to create large thermal stresses. Therefore, application of any of the convection coefficients would most likely not have affected the results significantly as all the convection coefficients

are close to the same order of magnitude. The hub was considered to be at room temperature and thus the analysis was run with the hub at 80°F.

As the plate is cooled, contraction takes place in the plate and an interference fit between the hub and girder is created. The model was analyzed the first 50 minutes of the cooling procedure and was used to determine whether or not this stage of AP3 was critical. The first few minutes of the cooling procedure produced the largest stresses due to the difference in temperature from the hub to the plate, and so it was important to ensure that the OMSR and OMCCL values did not drop too low in either the hub or the plate. Figure 32 shows the values of tensile (positive) hoop stress and Von Mises stress for the nodes in the hub. The largest tensile hoop stress in the hub was 17.278 ksi and can be seen at $t = 3$ minutes into the cooling procedure. The largest Von Mises stress in the hub was 22.520 ksi and occurred during the first minute of the assembly procedure. This is undoubtedly due to thermal gradients in the material as it comes into contact with the heated plate. Eventually as thermal gradients decline, both stresses appear to level off to a constant stress value.

The oscillation in the data is most likely caused by the "opening" and "closing" of the contact status. ANSYS allows for automatic adjustment in the contact pairs for each time step, which helps to provide convergent solutions. However, it is possible that the expansion and contraction of the hub and plate respectively cause the program to adjust the contact status unnecessarily, thus causing the slight oscillatory nature of the results. These oscillations do not have large amplitudes and follow a general trend line so they can be discounted as insignificant to the validity of the data.

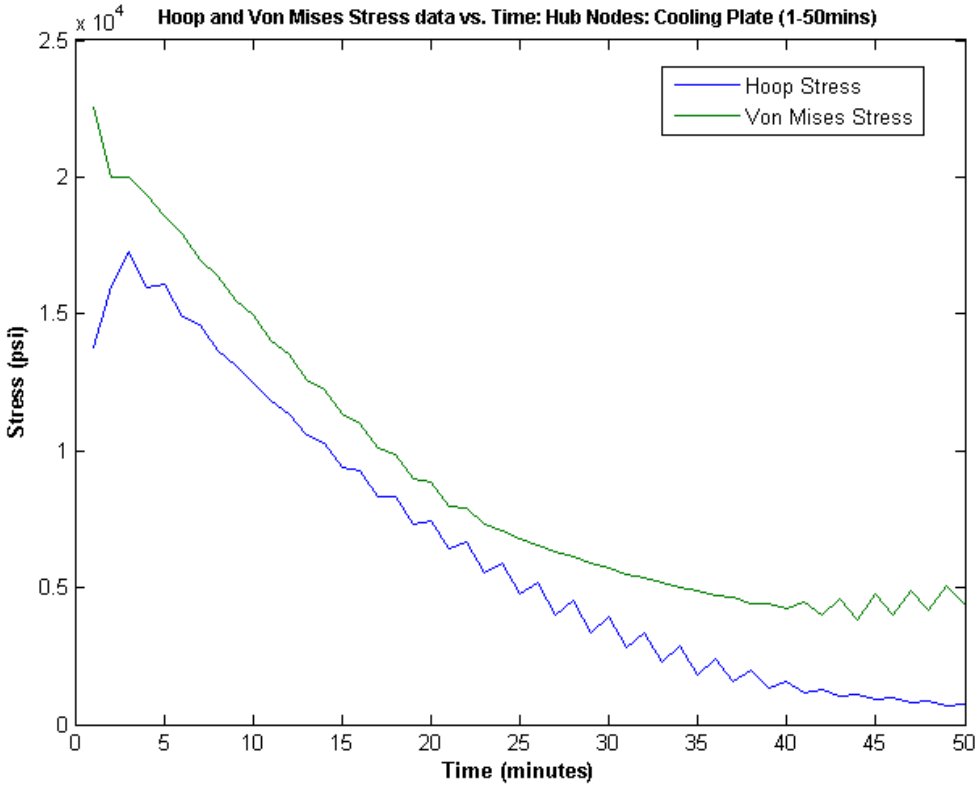

Figure 32 Tensile hoop stress and Von Mises stresses vs. time for hub nodes in Model 1 of AP3.

Temperature, nodal location and number, as well as stress data is written to a text file for each time step. MATLAB is again used to evaluate the data and calculate the stress ratios and critical crack lengths for each time step. The fracture toughness was again taken to be constant ($K = 47$ ksi) as this material property only increases with an increase in temperature for most steels. Figure 33 shows the CCL and OMCCL for the nodes in the hub from 1 to 18 minutes in the cooling procedure. The OMCCL was calculated as 5.0397" at $t = 3$ minutes into the cooling procedure which corresponds with the maximum hoop stress.

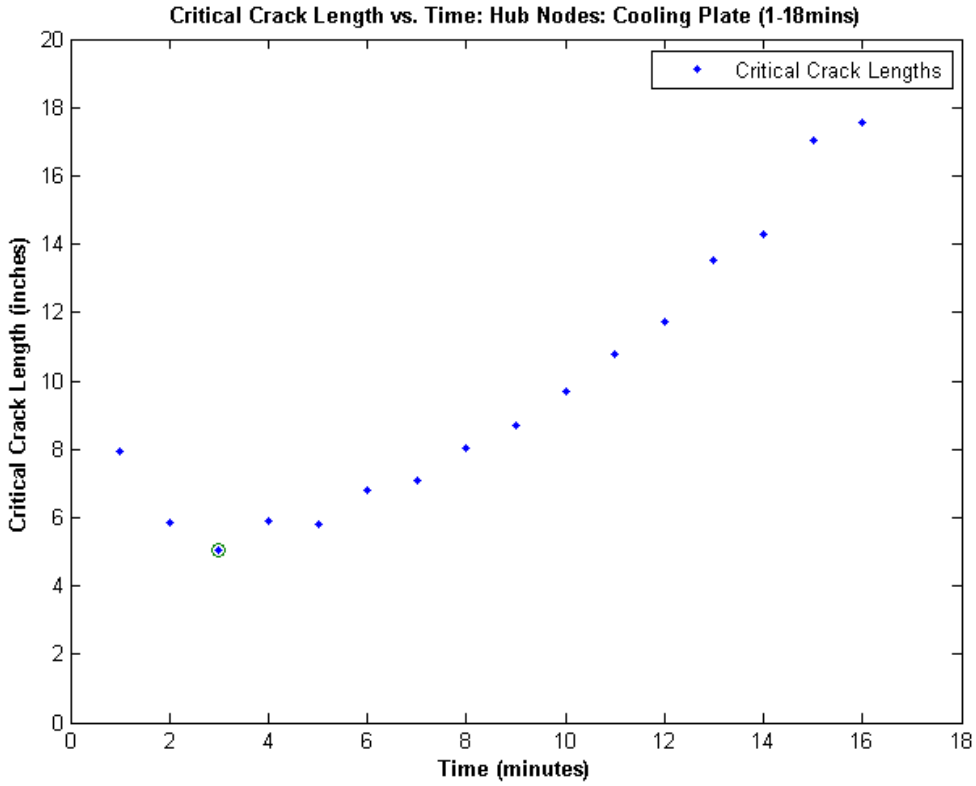

Figure 33 Critical crack lengths vs. time for hub nodes in the cooling portion of Model 1 of AP3.

The minimum stress ratios were also calculated at every nodal location for every time step. The yield strength of the material was calculated as a function of temperature using spline interpolation in exactly the same fashion as in the heating analysis. Figure 34 shows the minimum stress ratios versus time for all the nodes in the hub. The OMSR was calculated as 2.016 in the first time step of the cooling process. This is due to the high Von Mises stresses induced in the hub as it makes contact with the girder. The stress ratios steadily increase from this point however, and should continue to increase as temperatures reach steady state.

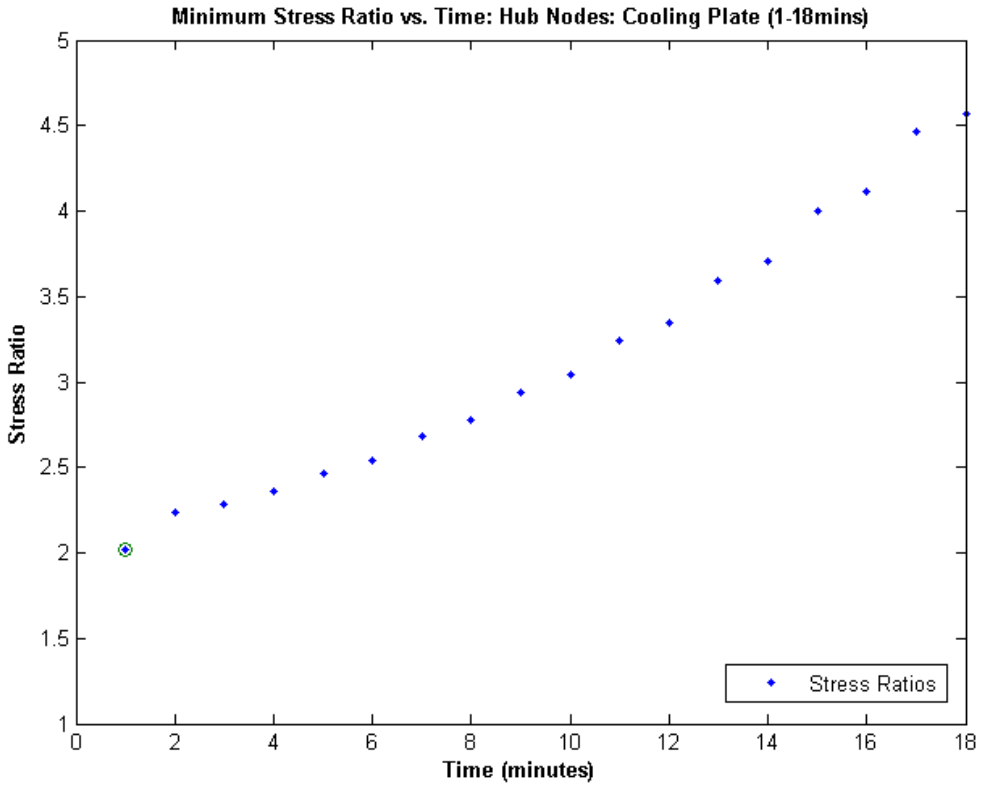

Figure 34 Minimum stress ratios vs. time for hub nodes in the cooling portion of Model 1 of AP3.

Additionally, the nodes in the plate must also be analyzed as failure must not occur in either the hub or plate components. The same procedures were used to analyze the plate nodes and the same components were calculated. It is logical to think that the most likely mode of failure would be via yielding as increased temperatures in the plate lower the yield strength of the material. Figure 35 shows the tensile hoop and Von Mises stresses in the plate for every time step. The highest hoop and Von Mises stresses are observed near the beginning of the trial which is similar to the stress plot of the hub. This is not unexpected as the plate will also have large thermal stresses induced in the material as it comes into contact with the hub. The largest hoop stress was 30.838 ksi and was

recorded at $t = 4$ minutes into the cooling procedure. The largest Von Mises stress was 29.755 ksi and was recorded at $t = 2$ minutes into the cooling procedure.

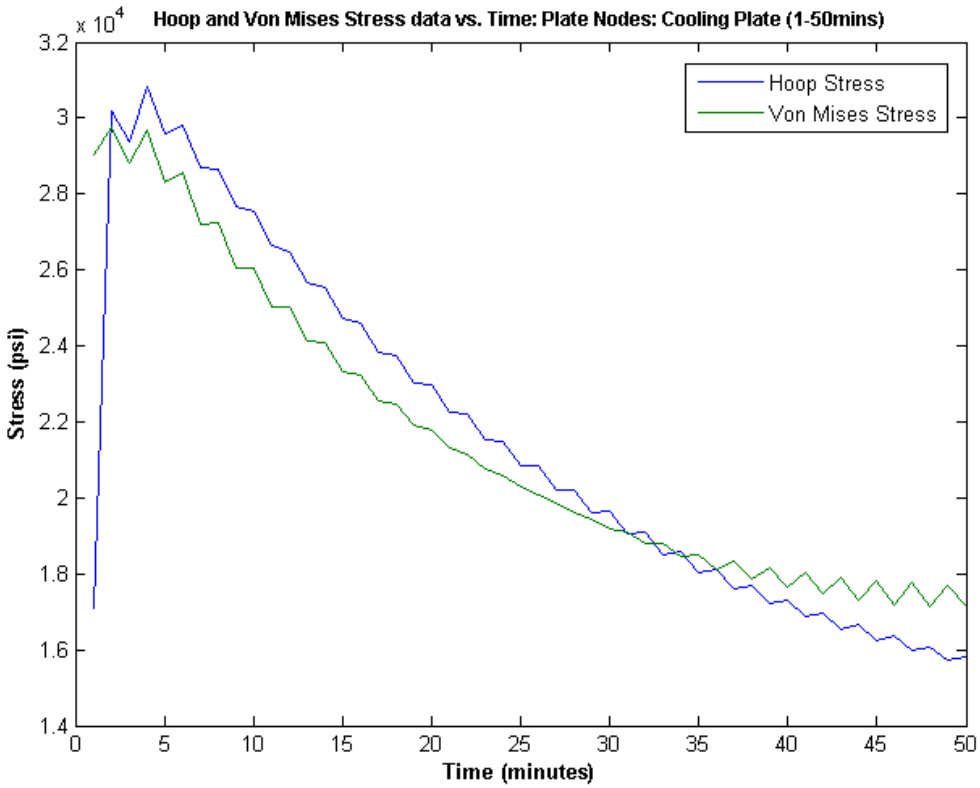

Figure 35 Tensile hoop stress and Von Mises stress vs. time for plate nodes in cooling of Model 1 for AP3.

The critical crack lengths were also calculated for every time step at the node with the maximum hoop stress. The same MATLAB program was used in the calculations and the same assumptions were applied. The OMCCL for the plate nodes was calculated as 1.5820" at $t = 4$ minutes into the cooling procedure. Figure 36 shows the CCL and OMCCL values from 1 to 18 minutes into the cooling procedure.

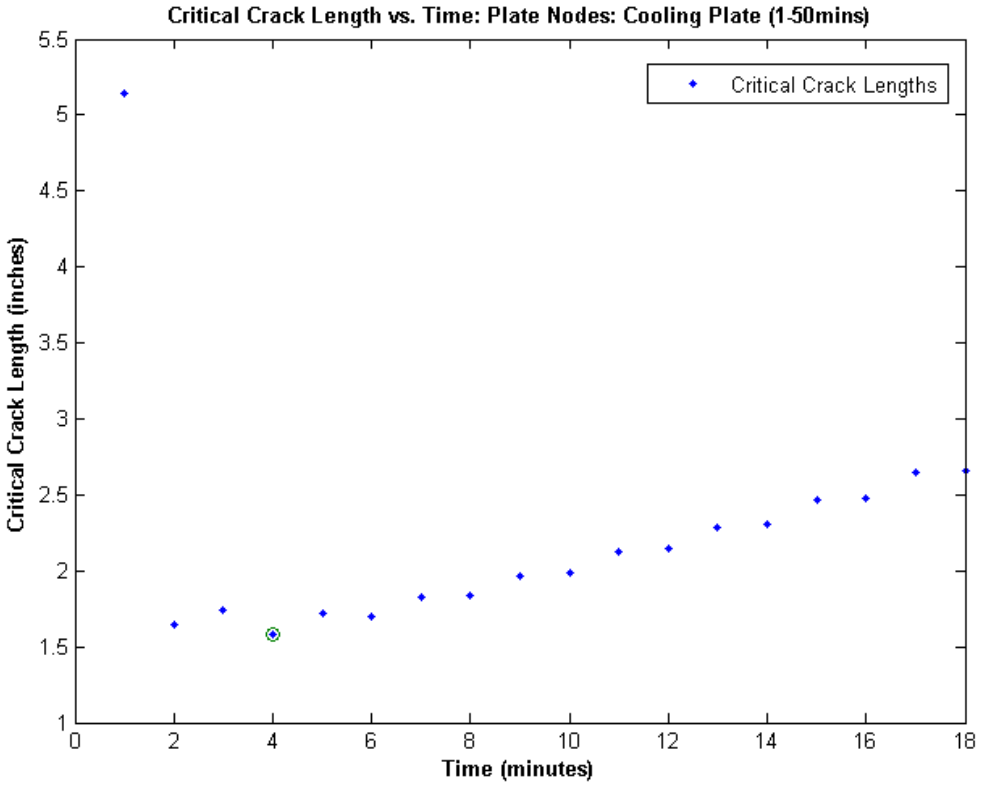

Figure 36 CCL and OMCCL values vs time for plate nodes in cooling of Model 1 of AP3.

In the same fashion, the minimum stress ratios are calculated just as previously in the heating of the plate. The yield strength was calculated in the same fashion as previously. The OMSR was calculated as 1.4701 at $t = 2$ minutes into the cooling procedure. Figure 37 shows the stress ratios and OMSR from 1 to 18 minutes into the cooling procedure.

The OMSR corresponds to the maximum Von Mises stress, but it is important to note that this may not always be the case. As the material properties of steel fluctuate with temperature, it is entirely possible that the right combination of temperature and stress could produce an OMSR that does not correspond to the time of maximum Von

Mises stress. This is why it is necessary to evaluate the stress ratios of all nodes at all time steps instead of just the nodes with the maximum stress.

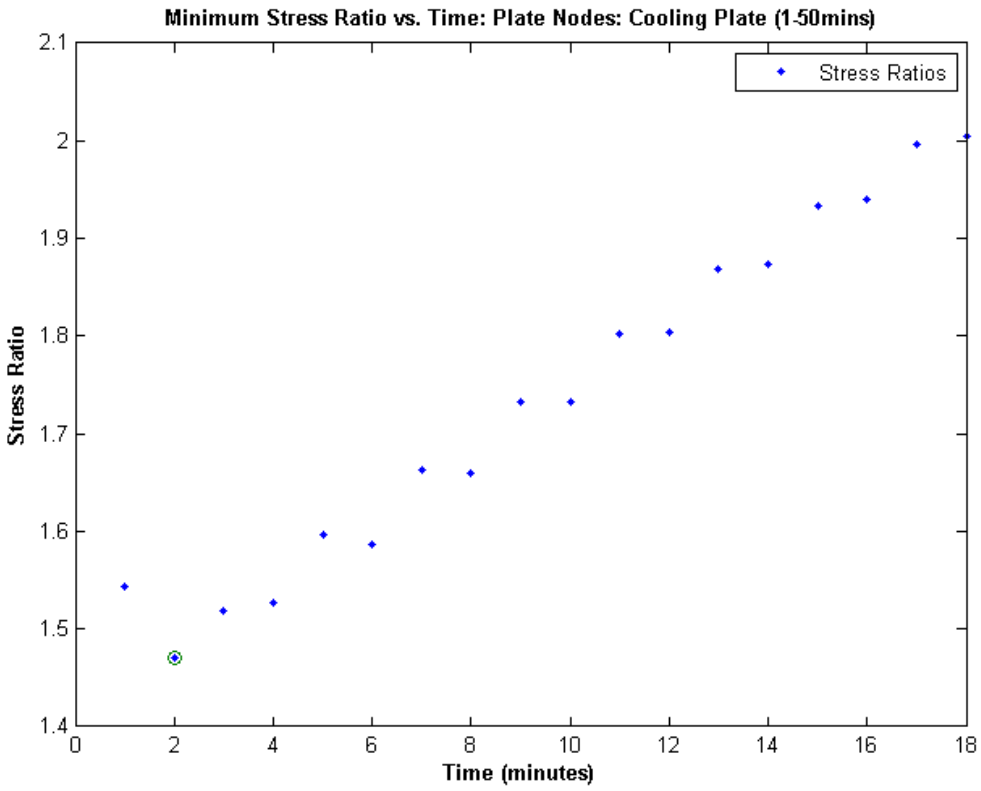

Figure 37 Minimum stress ratios vs. time for plate nodes in cooling of Model 1 for AP3.

From these calculations and plots, it can be reasonably deduced that no components would fail in either step 1 or step 2 of Model 1. For both step 1 and step 2 of the assembly procedure, stress ratios only increase with time after the initial thermal stresses reduce in magnitude. Critical crack lengths also display the same behavior, and only increase with time as the components move towards a steady state temperature. The only danger to this assembly procedure comes within the first few minutes of the cooling stage when the thermal stresses are high. Therefore, it is imperative that the plate is not heated beyond what is absolutely necessary to gain sufficient clearance in the hole to

allow for the insertion of the hub. Overheating could cause even larger thermal stresses to be induced in the material, and it increases the likelihood for failure.

This plate model serves as a very good basis of assumption for the girder. It is reasonably assumed that the temperatures and stresses in the girder would be comparable to those calculated in the plate model and so it was deemed unnecessary to analyze the full girder model.

4.9.2 Trunnion

With the validation that step 1 and 2 would not be critical steps in AP3, it was reasonably assumed that step 3—cooling of the trunnion—would be the critical step in this assembly procedure. High thermal stresses can develop in this component when dipped into various cooling mediums which could lead to failure.

A one-sixth axisymmetric model of each trunnion geometry was constructed in ANSYS and loaded in exactly the same fashion as in the previous analyses. Symmetric boundary and heat transfer conditions were applied to the "cut" edges, and convection coefficients were applied on all applicable surfaces. Figure 38 shows the fully meshed trunnion model for the 17th Street bridge.

A convergence study was performed on this model to ensure solution accuracy. Due to the simplicity of this model, convergence was much easier to prove definitively allowing for much greater confidence in model performance. The same procedure is utilized in this model with the use of a "mesh factor" to multiply the initial line divisions by some constant number. Figure 39 and 40 show the maximum hoop and Von Mises stresses at any point in the model at the same time step, respectively. This model

displays good characteristics and appears to converge to a value somewhere around 31 ksi for the hoop stress and 25 ksi for the Von Mises stress. Although a denser mesh will lead to a more accurate solution, it will also be very computationally expensive.

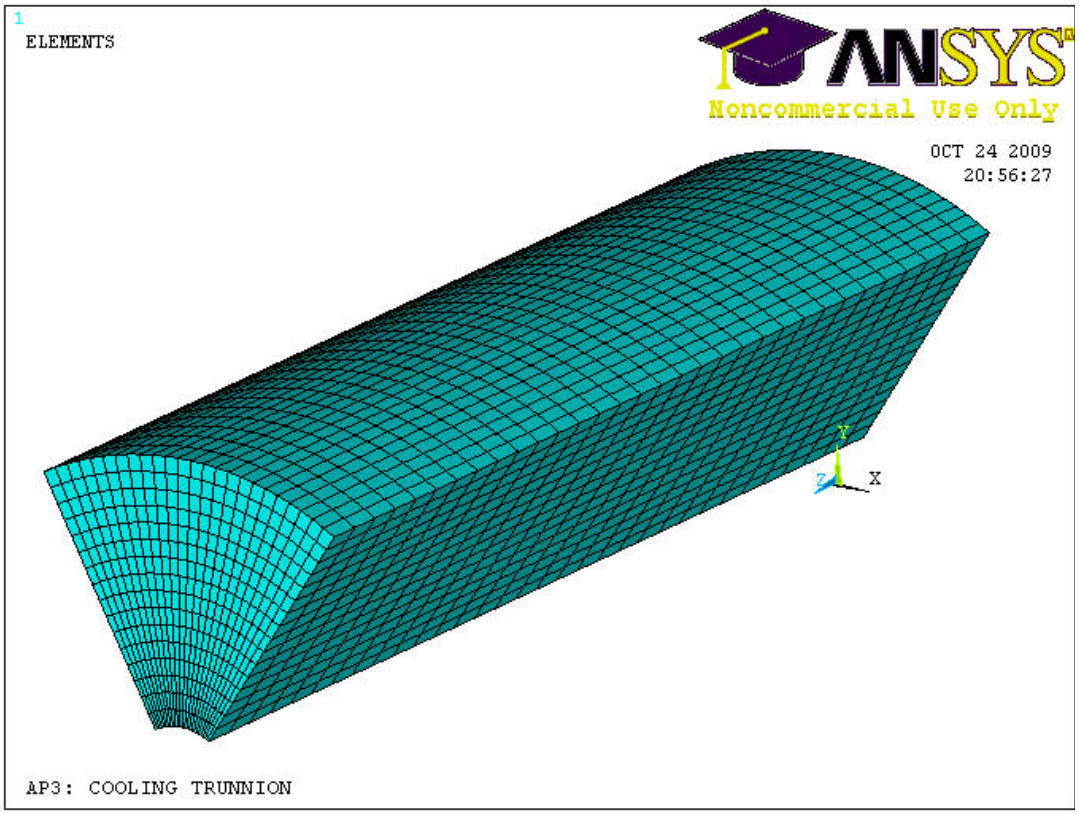

Figure 38 Fully meshed trunnion model used for AP3.

If the relative error between mesh densities is less than five percent, the model can be run at coarser densities without adversely affecting the results. For this work, the trunnion model was run at 71,079 nodes. This model produces a max hoop and Von Mises stress within five percent of the model run at 148,555 nodes, but in less than a quarter of the time. Using this technique, computation time is saved and model accuracy is secure.

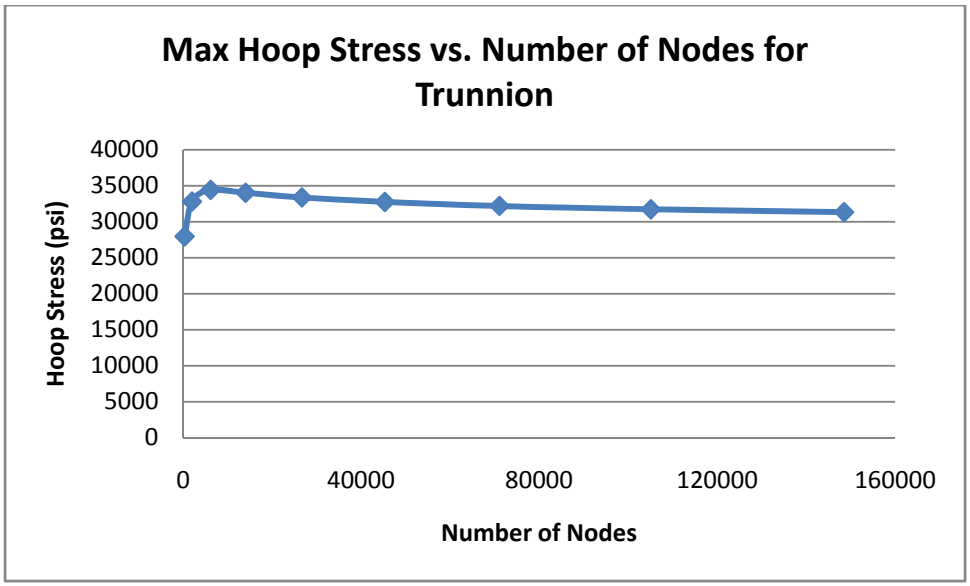

Figure 39 Maximum hoop stress vs. number of nodes for trunnion model for AP3.

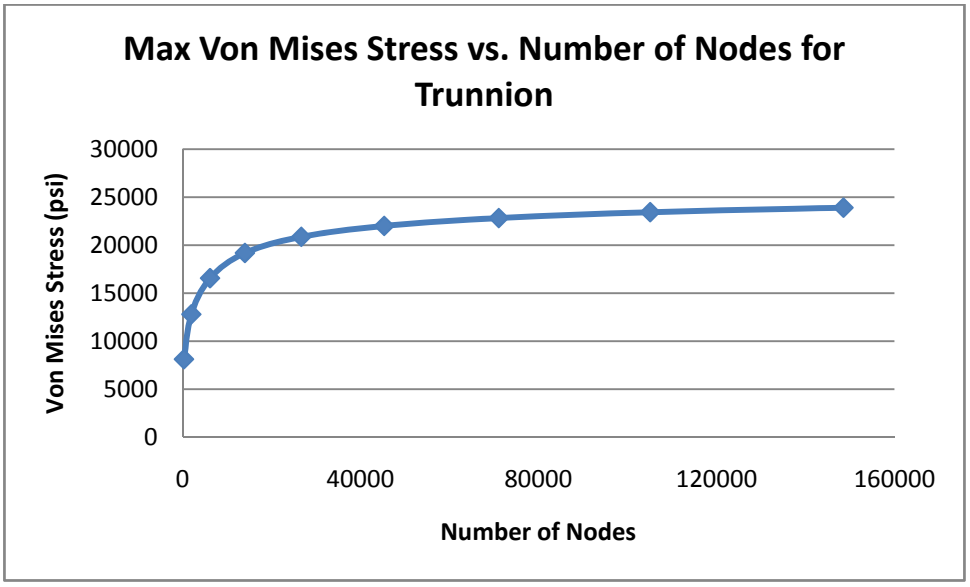

Figure 40 Maximum Von Mises stress vs. number of nodes for trunnion model for AP3.

CHAPTER 5 DESIGN OF EXPERIMENTS ANALYSIS

5.1 Introduction

A design of experiments analysis is a set of statistical techniques used in data evaluation to determine the effect of specific factors or combination of factors on the overall result. The overall goal is to determine specifically which factors effect the results most significantly. Experimentation is a vital part of science and engineering and it is necessary to have reliable and thorough methods for evaluating these experiments.

Traditional experimentation is based on experience—a simple experiment is run and the outputs are recorded. In the next experiment, changes are made to one of the input factors and again the outputs are recorded. Such changes are made indefinitely until the result is within the desired parameters. This method, although simple and easy to employ, lacks rigor and often does not indicate the *best* solution but rather just a *possible* solution. This is why a design of experiments approach was used in this thesis as it was necessary to know the extent of the influence the input factors or combination of factors had on the overall result. In this way, we can effectively quantify the effectiveness of an input factor or combination of factors on the overall output result.

5.2 Factorial Experiment

A factorial design of experiments approach varies several factors together in experimentation, rather than just one at a time [28]. Most problems in science and engineering are multi-faceted in that multiple inputs affect the overall output. Without an effective method of data evaluation, it would be impossible to determine which of these factors or combination of factors had the greatest influence on the result. A factorial experiment covers all possible combinations of inputs and how they affect the result. It also gives a basis of comparison to other similar experiments and allows for valuable quantitative and qualitative comparisons across multiple studies.

5.2.1 General Factorial Design

The general factorial design is one of the most basic but most effective factorial designs that can be used. It allows for mixed level factors very easily, and can handle as many factors as necessary for the analysis. It is important to note that an increase in factors often yields greater error in the experiment, and conclusions about factors and factor interactions on the output can be more difficult to determine.

For a general factorial design, the number of levels for factor A is given by a, the number of levels for factor B is given by b, and so on [28]. The number of factors and levels can be as large or as small as the designer wishes, although additional possibilities for error are induced in the experiment as the number of factors increases. Each factor has a specified number of degrees of freedom—or number of independent elements within a factor's sum of squares. For a general factorial design, the degrees of freedom are calculated as (a-1) for factor A, (b-1) for factor B and so on. The number of degrees

of freedom for factor interactions is given by the product of the degrees of freedom for each respective factor.

As in other factorial designs, the analysis of variance or ANOVA analysis is performed in the same manner. If analyzing a fixed effects model, test statistics for each main effect and interaction may be constructed by dividing the corresponding mean square for the effect or interaction by the mean square error for the experiment [28]. The percent contribution of each factor or factor interactions is given by the sum of squares for each factor or factor interaction divided by the total sum squares. Equation 9 shows the total sum of squares for a three level general factorial design.

$$SS_T = \sum_{i=1}^{a}\sum_{j=1}^{b}\sum_{k=1}^{c}\sum_{l=1}^{n} y_{ijkl}^2 - \frac{y_{....}^2}{abcn}$$

Equation 9 Total sum of squares for three factor design.

$$SS_A = \frac{1}{bcn}\sum_{i=1}^{a} y_{i...}^2 - \frac{y_{....}^2}{abcn}$$

Equation 10 Sum of squares for factor *A*.

$$SS_B = \frac{1}{acn}\sum_{j=1}^{b} y_{.j..}^2 - \frac{y_{....}^2}{abcn}$$

Equation 11 Sum of squares for factor *B*.

$$SS_C = \frac{1}{abn}\sum_{k=1}^{c} y_{..k.}^2 - \frac{y_{....}^2}{abcn}$$

Equation 12 Sum of squares for factor *C*.

The sum of squares for each of the main factor effects are given by Equation 10, 10 and 11. The sum of squares for the factor interactions are calculated in a similar manner. The percent contribution is one of the most important outputs of the ANOVA

analysis as it tells the experimenter which of the factors or factor interactions have the most significant affect on the output. This allows for quantitative comparison of the extent one factor or combination of factors is having on the experiment output. This is very useful to determine how best to avoid undesirable outputs, as well as contribute to the overall efficiency of a given process.

For this work, it is important to determine which factors or combination of factors affects the outputs OMCCL and OMSR most significantly for each assembly procedure. In the case of the OMCCL and OMSR, we desire to have large values and to avoid factors which cause small critical crack lengths to be produced. The following subchapters will detail the experimental design and results for each assembly procedure.

5.3 Assembly Procedure 1

There are four main factors for the general factorial design for AP1. Table 4 shows each factor and its corresponding levels. Note that an addition of this work is to add the bridge size itself as a factor in the design. This was a suggested addition to the work of Nguyen (2006) and provides a greater insight into how the size of the bridge geometry itself plays a role in the output of the OMCCL and OMSR. It is important to note however, that this factor may not be completely viable as the geometry for each bridge has large variations in dimensions. A better use of this factor would most likely come from dimensions that were scaled up relative to one another. Three bridge geometries are tested: 17th Street (small), Christa MacAuliffe (medium), and Hallandale (large).

Table 4 All factors and levels for general factorial design for AP1.

Factor		Levels
A	Bridge Size	Small (17th St.)
		Medium (Christa MacAuliffe)
		Large (Hallandale)
B	AASHTO Alpha Ratio	$\alpha = 0.10$
		$\alpha = 0.25$
		$\alpha = 0.40$
C	Radial Interference	Low
		High
D	Cooling Method	1. Liq Nitrogen
		2. Dry Ice/Al + Liq Nitrogen
		3. Ref Air + Liq Nitrogen
		4. Ref Air + Dry Ice/Al + Liq Nit

The experiment was not set up in random order as it is unnecessary and futile to do so. The purpose of randomization is to reduce error in the analysis but this is only valid for experimentation where unforeseen variables can directly influence the data. Since there are no external factors which could affect the solutions of the finite element analysis other than the user specified changes such as mesh density, cooling method etc. there is no need for randomization. A trial can be run a hundred times in ANSYS with no variation in the results.

The trials are set up sequentially based on the factor outline. This can be thought of as four nested "for" loops with the outermost loop defined by factor *A* and the innermost loop defined by factor *D*. Precise control over the order of the runs is very important when inputting the data into statistical software such as Minitab which was used for this work. The total number of runs required is the product of the number of levels for each factor. For this analysis, 3 (bridge size) × 3 (AASHTO alpha ratio) × 2 (radial interference) × 4 (cooling method) = 72 runs. All trials involving refrigerated air

as the cooling medium were eliminated as it can be reasonably assumed that no critical stresses or stress ratios will exist in that stage of the cooling process. For further details on cooling methods and convection coefficients refer to the work of Nguyen (2006).

The node number, *x*, *y*, and *z* locations, temperature, and the von Mises and hoop stresses are output for each time step for each trial. Although the units in ANSYS can be defined through the program, it is often the case to specify the units in such a way to allow for whatever time unit is appropriate. In this case, each trial was run for seventy "time units" which varied based on the cooling method used for that trial. The speed of the cooling process for liquid nitrogen is more rapid than that of a dry ice/alcohol bath and so the time unit was two seconds. The unit used for dry ice/alcohol was thirty seconds.

Once all data files were run, a MATLAB program was used to evaluate the data. Only the nodes with tensile (positive) hoop stress were considered in the calculation of the critical crack lengths. The MATLAB program then writes all critical crack length values and the OMCCL values to Excel files for further evaluation.

5.3.1 Results: AP1: OMCCL

The results of AP1 were consistent with the work of Nguyen (2006) with a few exceptions. The analysis had a percent contribution from the sum of the squares of the error of less than 0.3%. All values for OMCCL for AP1 are given in Appendix B. Figure 41 shows the percent contribution of the five most significant factors or factor interactions for the OMCCL in AP1.

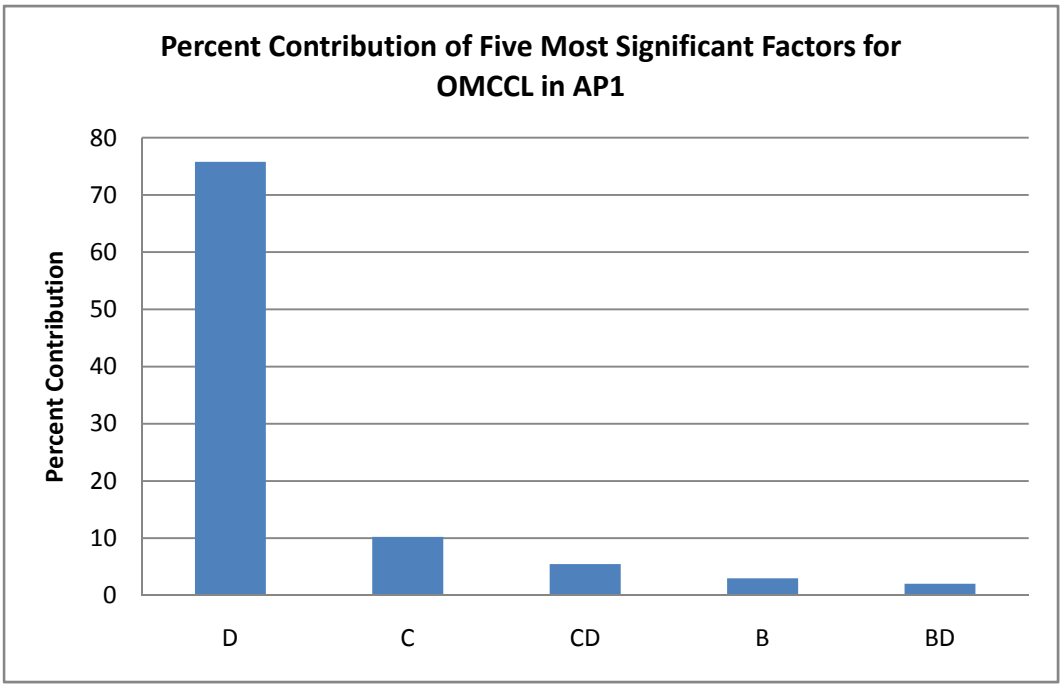

Figure 41 Percent contribution of five most significant factors for OMCCL in AP1.

As expected, the cooling method used (factor *D*) has the largest effect on the OMCCL in AP1 with a percent contribution of 75.7 percent. The radial interference (factor *C*) is also an important factor to consider as it contributes up to 10.2 percent to the OMCCL. The interaction between these two factors (*CD*) has a percent contribution of 5.5 percent. Other factors, such as the AASHTO alpha ratio (factor *B*) and the interaction between the cooling method and alpha ratio (factor *BD*) are not as significant but still contribute 2.9 and 2.1, percent respectively. This is consistent with the work of Nguyen (2006) who also found the cooling method to be the most significant.

5.3.1.1 Individual Factors

The influence of the individual factors on the OMCCL for AP1 is discussed in this section. These are the most basic of the factors in the ANOVA analysis but are often the most important.

As seen by Figure 42, the smallest OMCCL value comes from the smallest bridge (17^{th} Street bridge) and the largest from the medium size bridge (Christa MacAuliffe). It should be noted however, that the values of the OMCCL are very close to one another. The percent change from the small bridge to the large bridge is less than ten percent suggesting that changes in bridge size do not contribute significantly to the OMCCL. This could also be due solely to the variations in bridge geometry as discussed earlier.

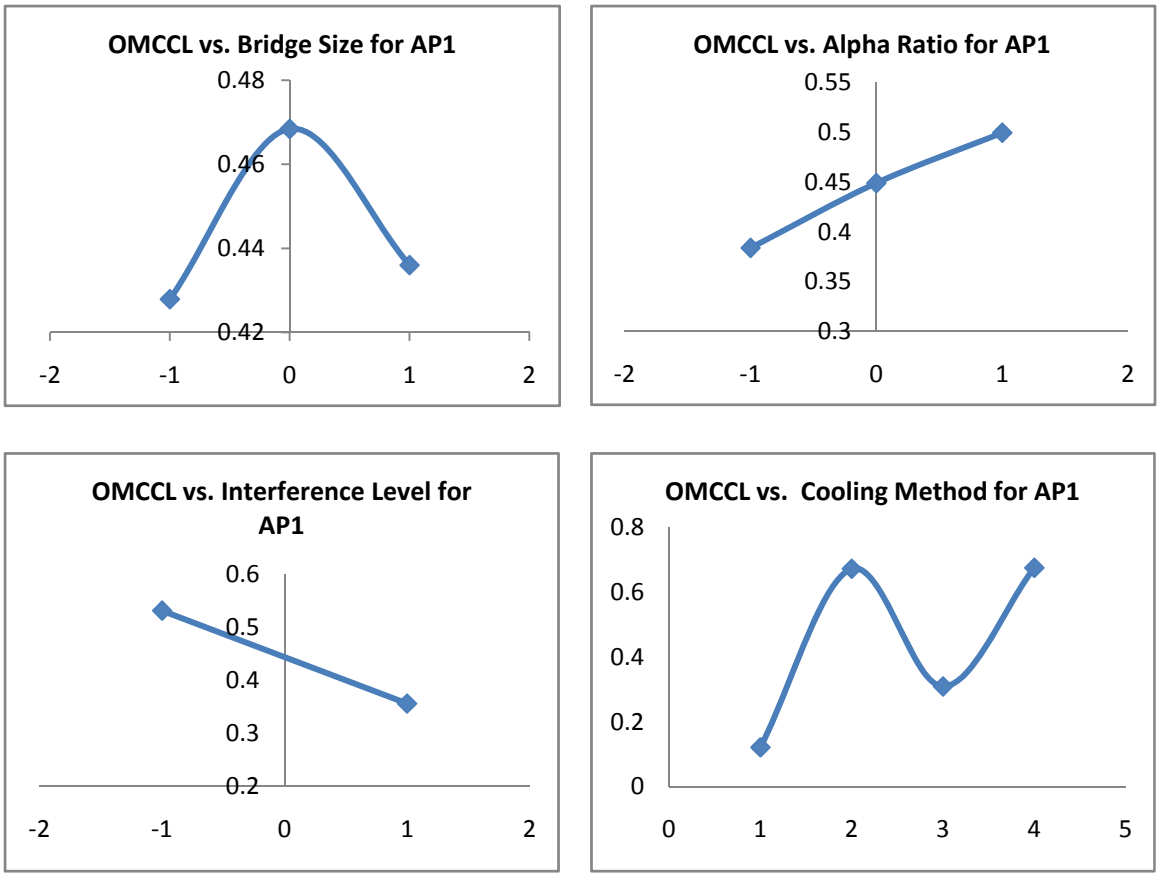

Figure 42 Individual factor interactions on OMCCL for AP1.

It can be seen that the OMCCL increases with the alpha ratio. A larger alpha ratio produces up to 30% larger OMCCL values. This differs somewhat from the work of Nguyen (2006) who predicted that the alpha ratio of 0.25 would produce the highest crack lengths for all bridges.

As expected for the interference level, higher interference produces up to 32% smaller OMCCL value. This factor cannot be controlled in a quantifiable way, but it can contribute significantly to failure. The upper and lower limits of this value are calculated as per FN2 fit specifications as given in Appendix A. The variation of the values for the interference should follow a normal distribution which means that the majority of the trials will not be run at a high level of radial interference.

The cooling method contributes the most to increasing or decreasing the OMCCL. This is expected as the percent contribution in the ANOVA analysis was largest for the cooling method. Cooling the components into liquid nitrogen provides the lowest OMCCL as this process induces the largest thermal shock. The second and fourth cooling methods provide an increase of 454% and 456% respectively to the OMCCL versus cooling method one. The use of cooling method three increases the OMCCL by 154%. The OMCCL for the second and fourth cooling method are almost the same.

This data is in good agreement with the work of Nguyen who predicted a similar trend in the OMCCL with respect to the cooling method. An increase of 262-406% in the OMCCL from cooling method one to cooling method four was observed [5]. This provides a more conservative estimate of the OMCCL versus the current work.

5.3.1.2 Factor Interactions

The factor interactions for the OMCCL will be presented and discussed in this section. Factor interactions are important to notice in a sensitivity analysis as they provide a very sound means of comparison from one change in factor input to the next. Conclusions are easier to draw from this information and allow for a clearer picture of how the OMCCL is affected.

As mentioned previously, the new addition to the sensitivity analysis is the bridge size (factor *A*). The interaction between bridge size and radial interference, bridge size and alpha ratio, and bridge size and cooling method are important additions to this work. Figure 43 shows the OMCCL versus all possible factors relative to bridge size.

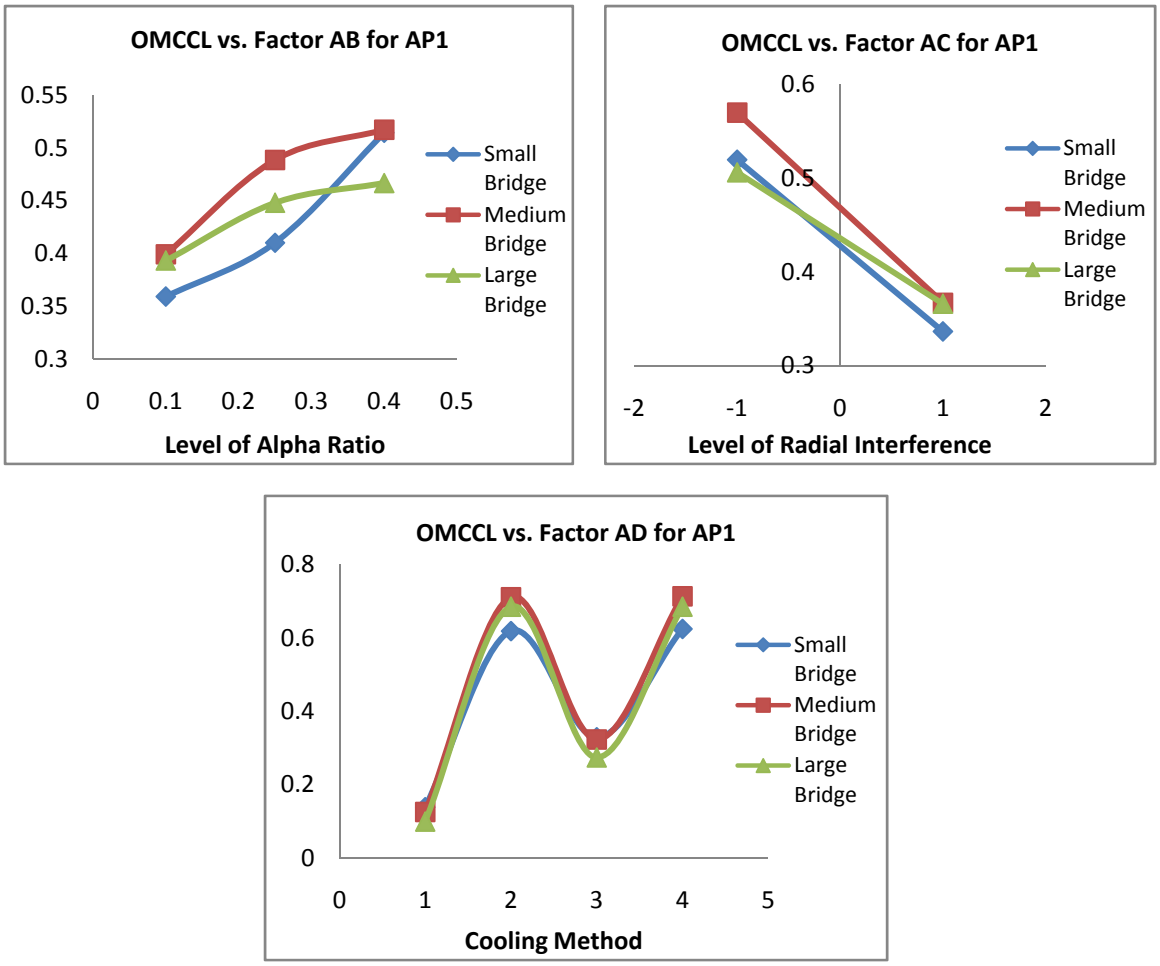

Figure 43 Factor interactions on OMCCL vs. bridge size for AP1.

It can be seen that as the alpha ratio increases relative to the bridge size, the critical crack lengths also increase. Using an alpha ratio of 0.4 on either a small or medium bridge produces an increase in the OMCCL of 43% and 29%, respectively versus using an alpha ratio of 0.1. Switching to a larger alpha ratio for a larger bridge only provides an 18% increase in the OMCCL.

Having a low radial interference in all bridges provides an increase in OMCCL versus a higher radial interference. However, the largest decreases in the OMCCL are observed in the small and medium bridges with both at 35%. A decrease of only 27% is observed in the large bridge geometry. It is important to note that the OMCCL at the

high interference level was larger for the large bridge versus the smaller bridge and almost as high as the medium size bridge.

Each bridge exhibits the same general trend in the OMCCL values relative to the cooling method. Cooling method one produces the lowest OMCCL values by far, but the medium bridge size gains the largest increases in the OMCCL value when the cooling method is changed, but not the largest percent increase. The largest percent increase is seen in the large bridge with an increase of 590% in the OMCCL from cooling method one to cooling method two or four. The smallest bridge has a percent increase of 346-350% in the OMCCL and the medium bridge has a percent increase of 466-468%. Again, it is important to notice that although the large bridge may have the most to gain from changing the cooling method, it still had the lowest OMCCL value and is still most likely to fail if liquid nitrogen is used to cool components. The medium size bridge exhibits the highest OMCCL values in all but the first cooling method.

Overall, the medium size bridge geometry yields the highest critical crack lengths. It cannot be completely determined that this bridge size or geometry will always produce the highest critical crack lengths, as the dimension scaling from one bridge to the next is not constant. As an example, the medium size bridge has a much larger flange size relative to the hub outer diameter than the other bridges. Perhaps this geometric attribute contributes more significantly to the critical crack length than the size of the geometry. Nevertheless, these results do provide some insight into how the size of bridge TH assemblies affects the OMCCL.

Other factor interactions provide additional insights. Figure 44 shows the OMCCL versus the remaining factor interactions—*BC*, *BD*, and *CD*. These interactions are not relative to bridge size.

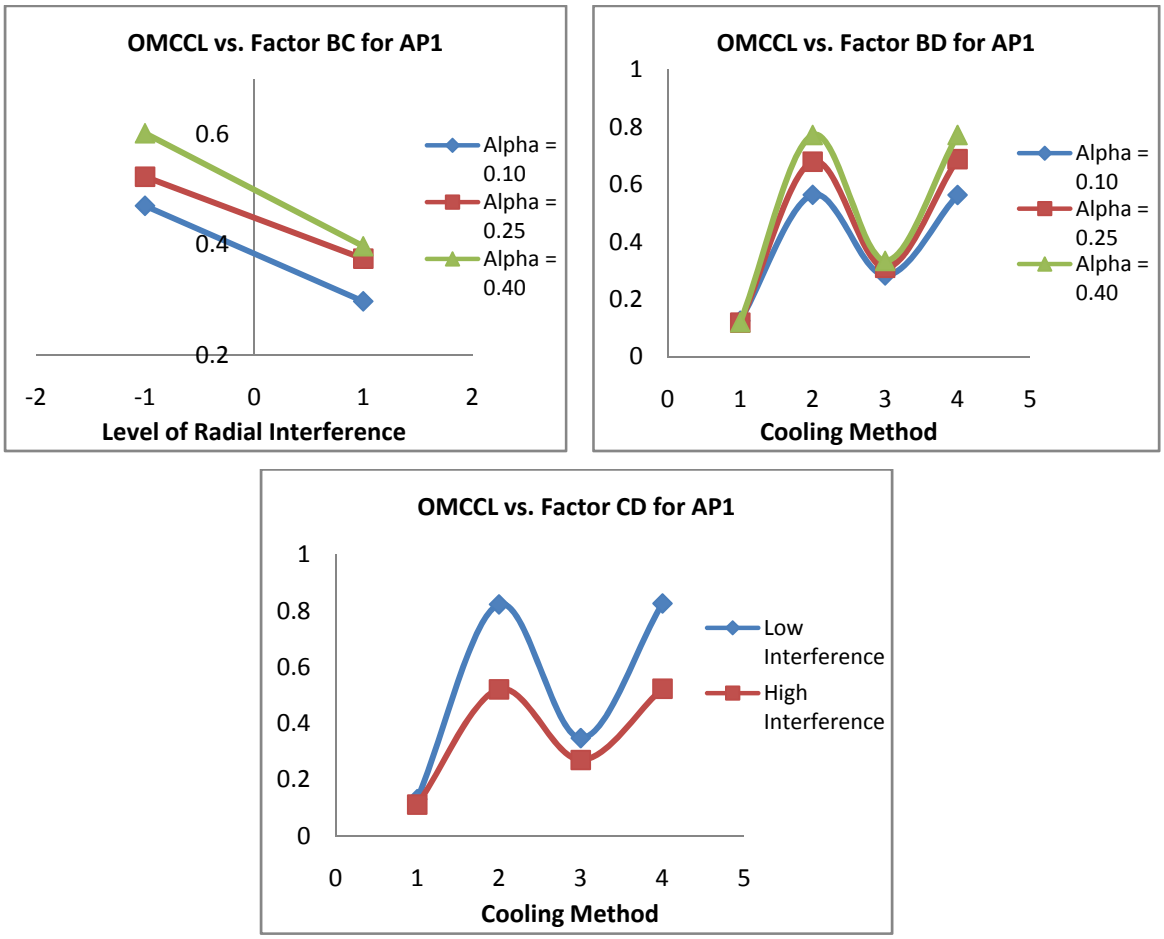

Figure 44 Factor interactions on OMCCL for AP1.

For the alpha ratio versus the radial interference level (factor *BC*), the largest percent decrease of 37% is observed in the OMCCL when the alpha ratio is 0.10. However, the largest values for the OMCCL are seen when the alpha ratio is 0.40. All alpha ratios show decreases in the crack lengths with an increase in radial interference which is expected.

For the alpha ratio versus the cooling method (factor *BD*), the largest percent increase in the OMCCL is 544% when the alpha ratio is 0.40. The largest values for the OMCCL are also observed in all cooling method except the first one. This reinforces the argument that the largest alpha ratio is the best to use. This is one area where this work differs from the work of Nguyen (2006) who predicted the largest OMCCL when alpha was 0.25.

For the radial interference versus the cooling method (factor *CD*), the largest OMCCL values come from low values of radial interference. This is expected and makes sense with the previous factors. It is important to note however, that this increase is most dramatic in cooling methods two and four with percent increases in OMCCL of about 57% for these cooling methods. The OMCCL only increases 17% from the low level of interference to the high level for cooling method one and 28% for cooling method three.

5.3.2 Results: AP1: OMSR

The results of AP1 for the OMSR were relatively consistent with the work of Nguyen (2006). The analysis had a percent contribution from the sum of the squares of the error of less than 3%. All values for OMSR for AP1 are given in Appendix B. Figure 45 shows the percent contribution of the five most significant factors or factor interactions for the OMSR.

As with the OMCCL, the cooling method (factor *D*) is the most significant factor relative to the OMSR. However, the percent contribution is less significant than in the analysis of the OMCCL with a percent contribution of only 55% versus 76% for the OMCCL. The radial interference (factor *C*) is also significant in to the output of the

OMSR with a percent contribution of 11%. Similar trends to the OMCCL percent contributions are seen with the exception that the bridge size (factor *A*) is now a significant factor with a percent contribution of almost 6%. The factor interactions for the cooling method versus the radial interference (factor *CD*) and alpha ratio versus cooling method (factor *BD*) have percent contributions of 6% and 4%, respectively.

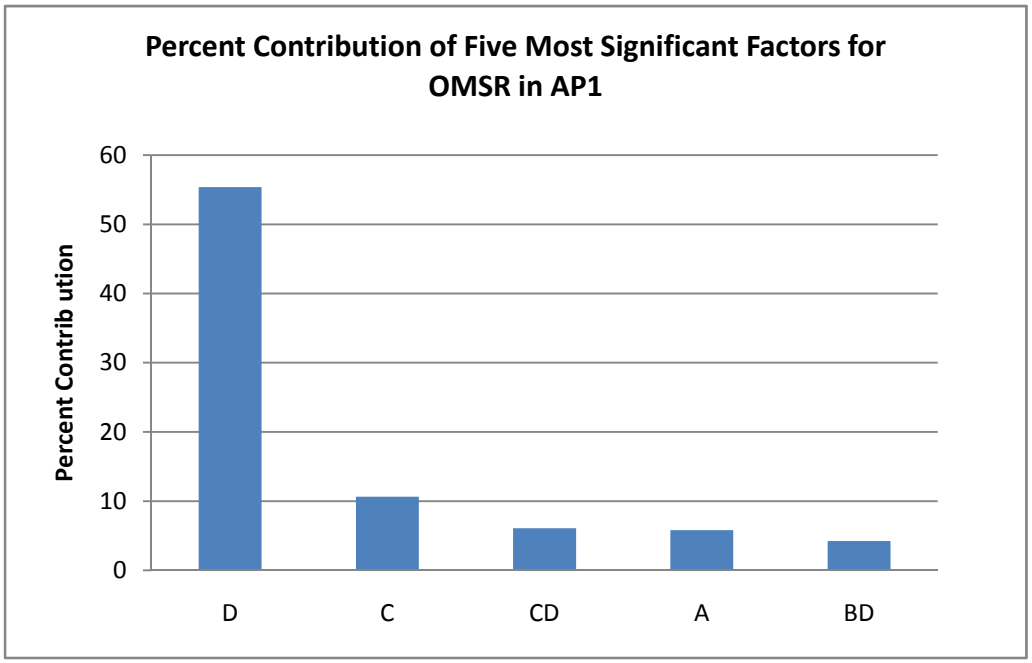

Figure 45 Percent contribution of five most significant factors for OMSR in AP1.

5.3.2.1 Individual Factors

The individual factor influence on the OMSR will be discussed in this section. Most of these factors behaved in the same way as in the analysis by Nguyen (2006) with a few exceptions. Figure 46 shows the OMSR versus the individual factor interactions.

The bridge size showed a slightly different trend for the OMSR versus the OMCCL with the largest bridge yielding the largest stress ratio. The percent increase in

the OMSR for the large bridge relative to the small bridge is 21% and 2% for the medium bridge size. The medium bridge size provided the largest values for the OMCCL.

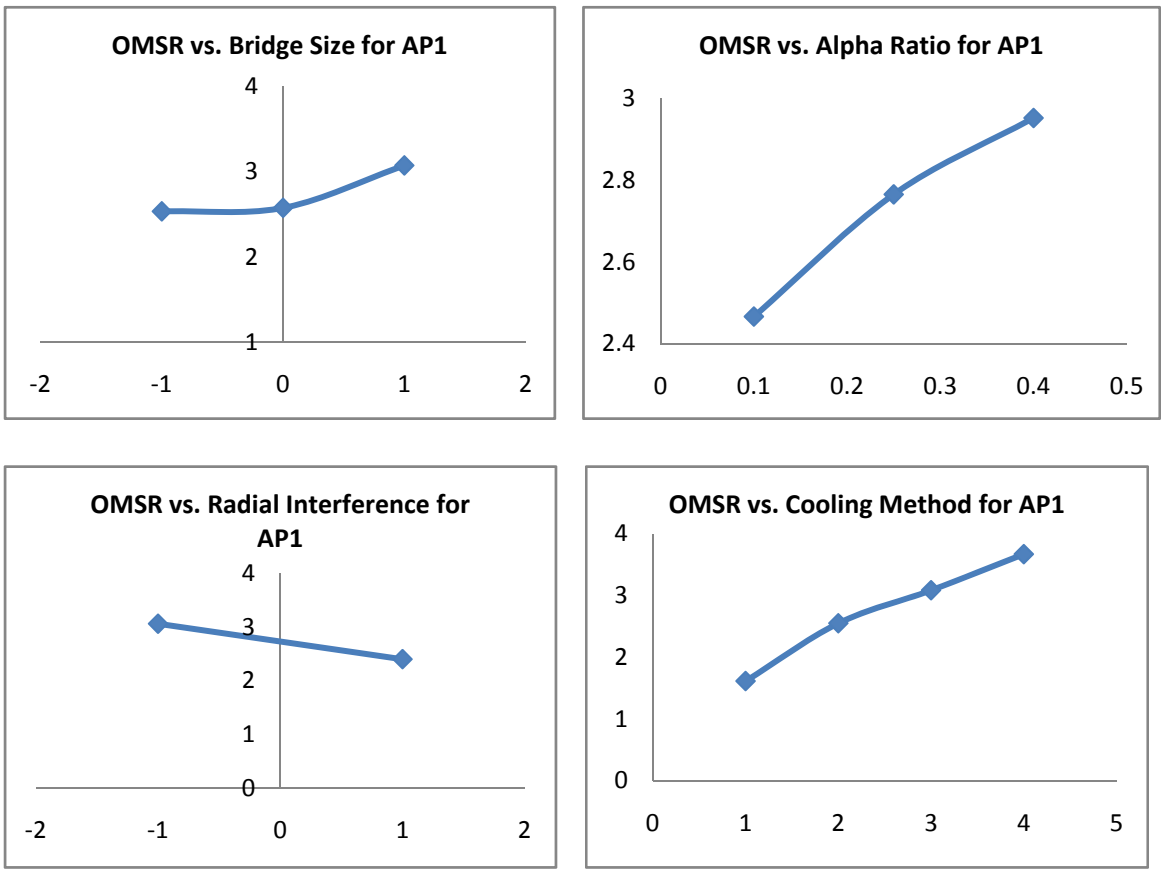

Figure 46 Individual factor interactions on OMSR for AP1.

The largest alpha ratio (factor *B*) provided the largest OMSR values which is a similar trend to the OMCCL. The percent increase in the OMSR relative to the lowest alpha value of 0.10 is 12% and 20% for alpha values of 0.25 and 0.40 respectively. This is slightly in contrast to the work of Nguyen who predicted that an alpha ratio of 0.25 would be produce the largest OMSR values. However, this does conform to the AASHTO recommendations regarding the use of hub assemblies with an alpha ratio of 0.40.

An expected and similar trend exists for the radial interference (factor *C*) whereby the OMSR decreases as the radial interference increases. The percent decrease in the OMSR is 21% which is less than the 32% decrease for the OMCCL, but is nevertheless significant. Again, the level of radial interference cannot be controlled but can be assumed to follow a normal distribution which suggests that the vast majority of TH assemblies will not be subject to high interference levels.

The cooling method is the most significant factor effect to the OMSR and displays similar trends to the work of Nguyen (2006). The percent increase in OMSR relative to the first cooling method is 58%, 91% and 127% for the second, third, and fourth cooling methods, respectively. This is slightly different than the OMCCL in which the values for the second and fourth cooling methods were virtually the same.

5.3.2.2 Factor Interactions

The factor interactions on the OMSR will be discussed in this section. These interactions provide meaningful insight into how the OMSR is affected with varying inputs. As with the analysis of the OMCCL, discussion of the bridge size versus alpha ratio (factor *AB*), bridge size versus radial interference (factor *AC*) and bridge size versus cooling method (factor *AD)* will be performed first. Figure 47 shows the OMSR versus all possible factors relative to bridge size.

The alpha ratio relative to bridge size has a slightly different effect on the OMSR versus the OMCCL. The large bridge has the largest OMSR values with the largest value for an alpha value of 0.25. Relative to an alpha value of 0.10, the percent increase in OMSR is 22% and 18% for alpha values of 0.25 and 0.40, respectively. This is in

contrast to the trends seen by the OMCCL where the medium size bridge had the largest crack values. It should be noted that the smallest bridge size consistently produces the smallest OMCCL and OMSR values for almost every alpha ratio. It should also be observed that the OMSR almost always increases with an increase in the alpha ratio.

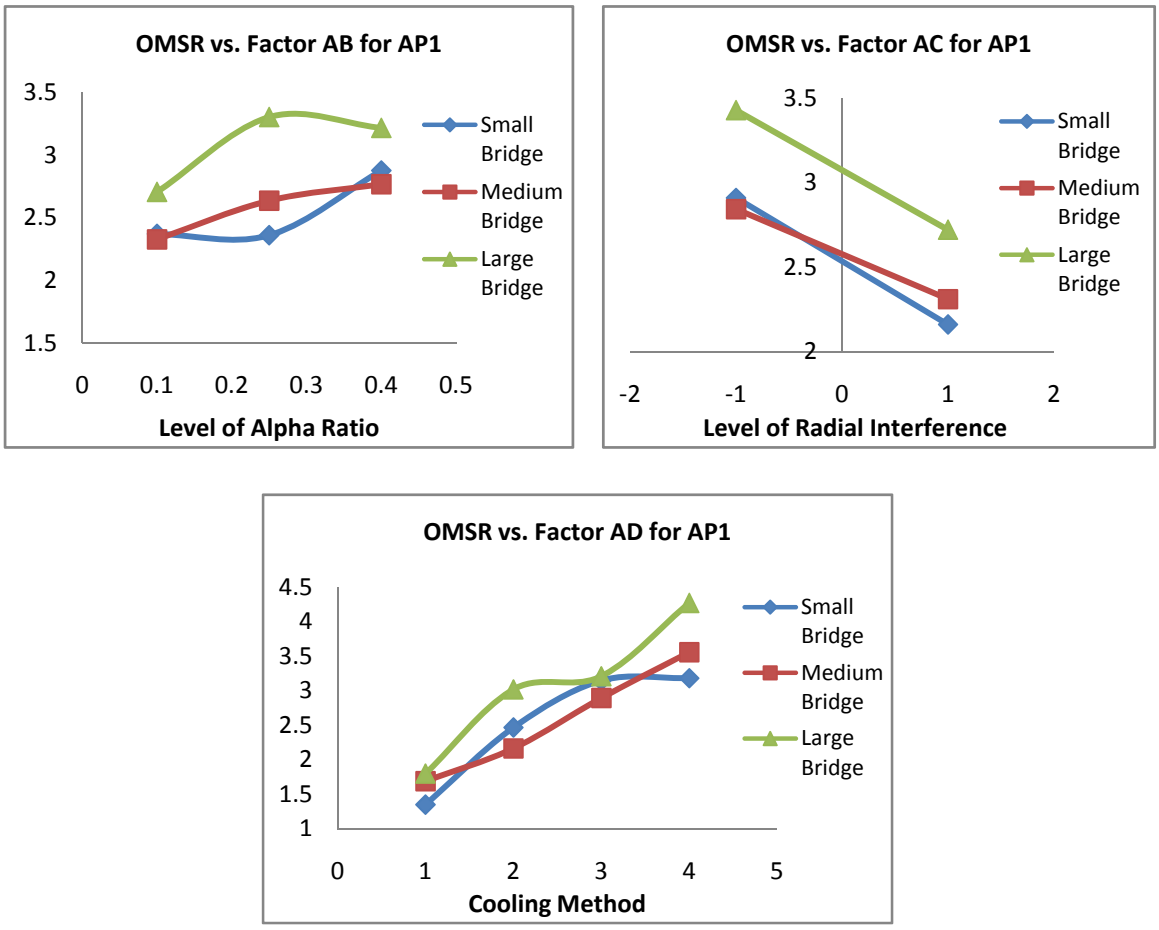

Figure 47 Factor interactions on OMSR vs. bridge size for AP1

The interaction of radial interference relative to bridge size on the OMSR has similar trends to the OMCCL but with exceptions. Again, it can be observed that the large bridge size has the largest OMSR values and a percent decrease of 33% from high to low interference levels. The percent decrease for the small and medium size bridges are 36% and 28%, respectively. The small bridge again yields the lowest OMSR of all

bridges for the high interference level, suggesting that the level of radial interference is more significant for smaller bridge geometries.

The interaction of the cooling method relative to the bridge size also shows interesting trends. The OMSR is largest for the large bridge geometry with a percent increase in the OMSR of the second, third, and fourth cooling methods relative to the first cooling method of 68%, 78%, and 137%, respectively. The small and medium bridges have percent increases in the OMSR of 136% and 111%, respectively. The first cooling method affects the small bridge geometry most significantly and produces the lowest OMSR for any bridge size.

The large bridge consistently produces the highest stress ratios for every factor interaction relative to the bridge size. This is somewhat in contrast to the trend observed in the OMCCL where the medium size bridge produced the highest crack lengths. Definitive conclusions are difficult to draw as stated previously due to the large variation in bridge geometry. The large bridge could have simply had more efficient dimensions to yield smaller Von Mises stresses and thus smaller OMSR values.

The other factor interactions also provide important insights. Figure 48 shows the OMSR versus the remaining factor interactions—*BC*, *BD*, and *CD*. As with the OMCCL, these interactions are not relative to bridge size.

For the alpha ratio versus the radial interference (factor *BC*), the trends in the data are identical to factor *BC* for the OMCCL. The large alpha ratio produces the largest OMSR values with a percent decrease from low radial interference to high radial interference of 20%. The smallest alpha value produces the largest percent decrease with a 26% decrease in the OMSR. The middle alpha value had a percent decrease of 19%.

This data suggests that larger alpha ratios are more resistant to failure via yielding and via crack propagation.

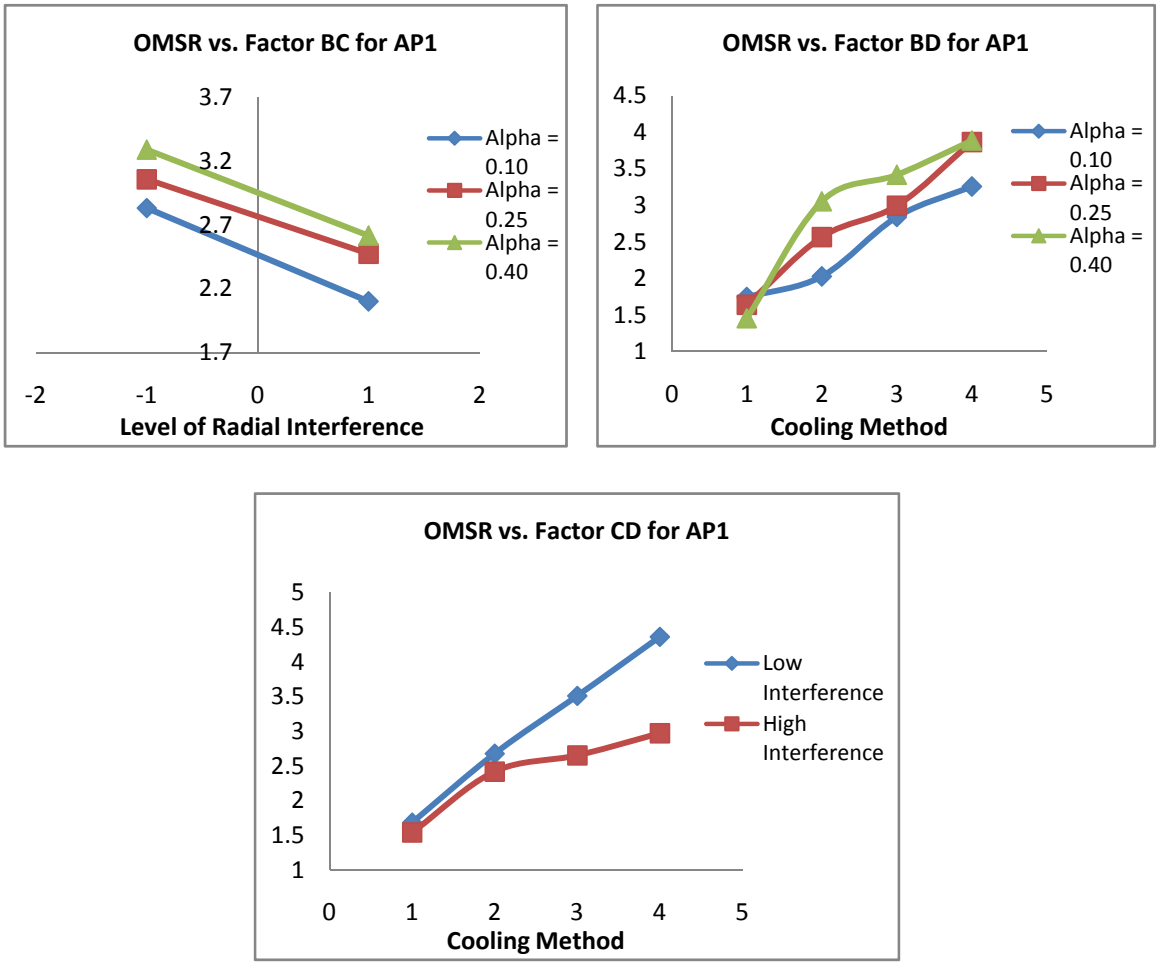

Figure 48 Factor interactions on OMSR for AP1.

For the alpha ratio versus the cooling method (factor *BD*), the trends in the data are similar to the individual factor for the cooling method. Although the largest alpha ratio produces the smallest OMSR, it also produces the largest OMSR for every other cooling method. The percent increase in OMSR for the alpha ratio relative to cooling method one are 87%, 136%, and 167% for alpha ratios of 0.10, 0.25, and 0.40, respectively.

The final interaction between the radial interference and the cooling method (factor *CD*) shows expected trends. The high radial interference level produces lower stress ratios for all trials but significantly higher OMSR values for the third and fourth cooling methods. Cooling method two produces a percent decrease in the OMSR of 10.7% from high to low interference, but cooling methods three and four produce 32% and 46% decreases, respectively.

5.3.3 Conclusions: AP1

For the first assembly procedure, some general conclusions and observations can be made.

1. With respect to bridge size, the medium size bridge (Christa MacAuliffe) consistently yields the largest OMCCL values with respect to all other factors. In addition, this bridge size also sees the second largest benefit from switching to the largest alpha ratio with a percent increase in OMCCL of 29% versus the smallest alpha ratio. This bridge size also sees the second largest increase in OMCCL relative to cooling method with a 466-468% gain. When considering the OMSR, the large bridge size shows the largest values for all factors. The largest bridge size also has the largest percent increase in the OMSR relative to cooling method (67-137%) and to an alpha ratio of 0.25 (22%), and it has the second smallest percent decrease relative to radial interference.
2. Increasing alpha ratios consistently increase the OMCCL and OMSR for every bridge size, with the largest OMCCL and OMSR values for all bridges (with the exception of the large bridge for OMSR) at an alpha ratio of 0.4. The medium

size bridge shows the largest percent increase in OMCCL from the smallest to largest alpha ratio with 43%. The largest alpha ratio produces the largest OMCCL and OMSR values and largest percent increase (544% and 167%) with respect to the cooling method. The largest alpha ratio also produces the largest OMCCL and OMSR values and second smallest percent decrease (34% and 20%) with respect to radial interference.

3. The uncontrollable radial interference factor not unexpectedly decreases the OMCCL and OMSR for every factor, but the medium bridge size has the highest OMCCL values for both the high and low levels of interference and the second highest OMSR values. The percent decrease in OMCCL from low to high levels of interference is 35% for the small and medium bridges, but only 27% for the large bridge geometry. With respect to the cooling method, increases in crack length of up to 57% can be seen from the high to low levels of interference for the OMCCL and 47% for the OMSR.
4. With respect to the cooling method, results are consistent with the work of Nguyen (2006). The percent increase in OMCCL and OMSR can be as much as 590% and 167% when changing cooling methods from one to two.

5.3.3.1 Recommendations: AP1

Based on these observations, the most successful combination of alpha ratio, cooling method and bridge size should be a medium size bridge and an alpha ratio of 0.4 using cooling method two. This bridge size consistently produced the largest OMCCL values and normally the second largest OMSR values. Although radial interference is a

random variable which cannot be predicted, the OMCCL was highest for the medium size bridge for both high and low levels of interference.

As mentioned previously, it is difficult to determine specifically whether bridge size or favorable variations in dimensions relative to each bridge were the real cause of larger OMCCL values for the medium size bridge. It is entirely possible that this specific bridge geometry was able to distribute loading or heat more effectively which allowed for larger crack lengths. A more complete analysis of bridge size would involve one unified set of dimensions with a scaling factor used to increase dimensions from one bridge size to the next.

5.4 Assembly Procedure 2

There are three main factors for the general factorial design for AP2—bridge size (factor *A*), AASHTO alpha ratio (factor *B*) and the cooling method (factor *D*). The set up of this sensitivity analysis is exactly the same as in AP1 with the exception that the radial interference is not a factor in the analysis. In AP2, the hub is shrink fit and inserted into the girder so no radial interference values are present in this process. Radial interference does exist between the girder and the hub as the hub reheats to a steady state temperature (hub-girder interface) but this interference produces compressive stresses that are not critical to the OMCCL and OMSR.

All alphabetical factor references (i.e. factor *D* is still cooling method) are kept the same to make comparisons easier. All factors are given in Table 4 with the exception of the radial interference. The total number of runs is given by the product of all the levels in each factor. For this analysis, 3 (bridge size) × 3 (AASHTO alpha ratio) × 4

(cooling method) = 36 runs. Just as in AP1, all trials involving refrigerated air as a cooling medium were omitted as it can be reasonably assumed that this cooling method will not produce low values of the OMCCL and OMSR.

The critical step for AP2 is thought to be the dipping of the hub in a cooling medium. The dipping of the trunnion may in fact be the critical process in this assembly procedure, but this will be addressed later.

5.4.1 Results: AP2: OMCCL

The results for the OMCCL in the second assembly procedure are discussed in this section. Some of the data resembles that of AP1, but in many cases the trends are very different. The analysis had a percent contribution from the sum of the squares of the error of less than 0.3%. All values for OMCCL for AP2 are given in Appendix B. Figure 49 shows the percent contribution of all factors and factor interactions for AP2.

As in the analysis of AP1, the cooling method has the largest percent contribution of 83% in the ANOVA analysis. The next closest factors are the alpha ratio (factor *B*) with 8% contribution and the bridge size (factor *A*) with 4% contribution. Factor interactions are not as significant as in AP1, but still are valid indicators of trends in the data.

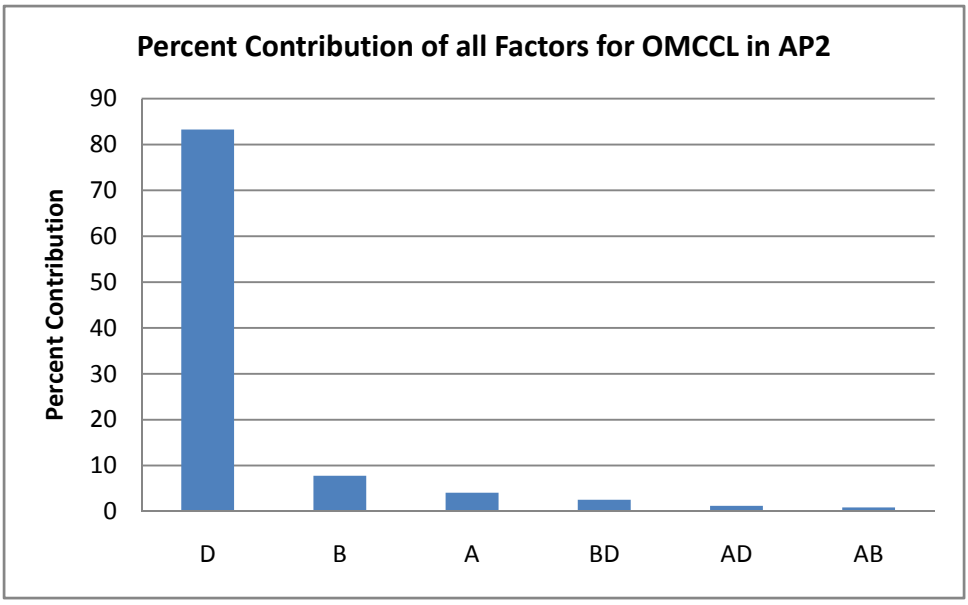

Figure 49 Percent contribution of all factors for OMCCL in AP2.

5.4.1.1 Individual Factors

The effect of individual factors on the OMCCL for AP2 is discussed in this section. Most of the trends in the data are not unexpected but provide an effective means of characterizing how each factor is affecting the OMCCL. Figure 50 shows OMCCL versus each individual factor for AP2.

It can be seen from Figure 50 that the largest bridge size produces the smallest critical crack lengths. This is in contrast to AP1 where the medium bridge size produced the largest crack lengths. The percent decrease in OMCCL from the small bridge to the large bridge is 30%. The percent decrease from the small bridge to the medium bridge is 16%. In general, it is still difficult to make definitive conclusions on these numbers as various bridge geometries may just be inherently more resistant to cracking than others.

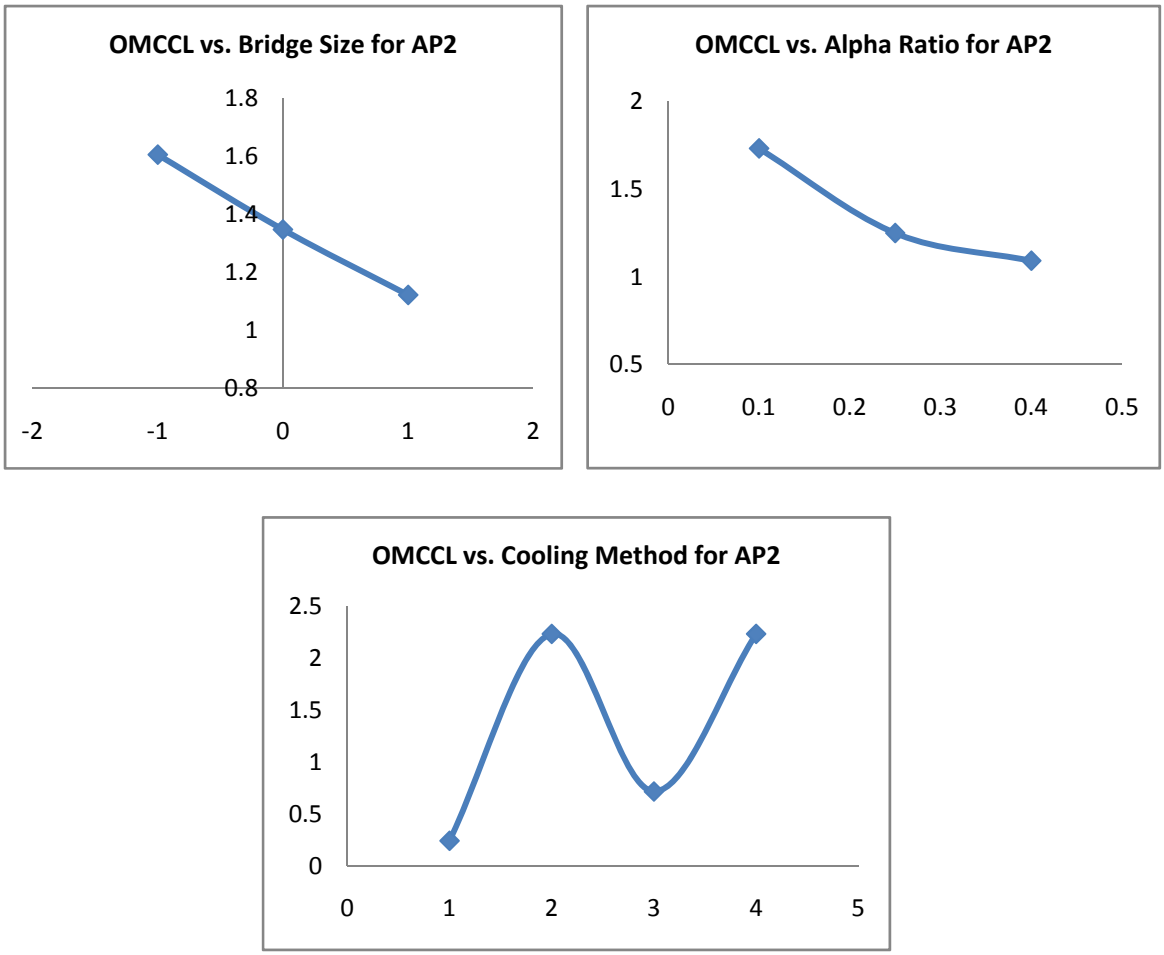

Figure 50 OMCCL vs. all factors for AP2.

The OMCCL decreases with an increase in alpha ratio, which is again in contrast to the data for AP1. For AP1, it was seen that the OMCCL increased with the increase in the alpha ratio. An explanation of this comes by realizing that larger thermal gradients will exist in hubs with larger alpha ratios as these hubs have larger radial thicknesses. The percent decrease in the OMCCL from an alpha value of 0.10 to 0.40 is 37%, but the percent decrease from for alpha values from 0.10 to 0.25 is only 28%. This data suggests that when using AP2, the smallest possible alpha ratio would be the best choice in terms of minimizing the OMCCL.

The second and fourth cooling methods provide the largest OMCCL values for AP2, which is exactly the same trend seen in the analysis of AP1. However, the percent increase in the OMCCL from cooling method one to cooling method two or four is even more significant in AP2 than it was in AP1. The total percent increase in OMCCL is 818% versus 454% for AP1. The percent increase in OMCCL for the third cooling method is 194% for AP2 versus only 154% for AP1. This data suggests that the OMCCL in AP2 has more to gain by switching cooling methods versus AP1. It is also important to note that the value of the mean OMCCL for cooling method one in AP2 is more than double the mean OMCCL for this cooling method in AP1.

5.4.1.2 Factor Interactions

The factor interactions on the OMCCL for AP2 will be discussed in this section. As in AP1, the main factor interactions involving the bridge size versus the alpha ratio (factor *AB*), and the bridge size versus the cooling method (factor *AD*) will be discussed first. Figure 51 shows the OMCCL versus all possible factors relative to bridge size.

For the interaction of alpha ratio relative to bridge size for the OMCCL, it can be seen that the small bridge size has the highest OMCCL values. All bridge sizes decrease with an increase in the alpha ratio however, which is in contrast to the data of AP1 where an increase in alpha ratio yielded larger critical crack lengths. Also, the medium size bridge had the highest OMCCL values in AP1 which is not the case in AP2. The percent decrease in the OMCCL from an alpha ratio of 0.10 to 0.40 is 42%, 35% and 28% for the small, medium and large bridges, respectively. This suggests that although the small

bridge has the smallest OMCCL values, it also most affected by increasing the alpha ratio.

For the interaction of cooling method relative to bridge size on the OMCCL, the small bridge again shows the largest critical crack lengths for all cooling methods and the largest bridge has the smallest critical crack lengths. However, the largest bridge size shows the largest percent increase in OMCCL from cooling method one to cooling method two/four with an 897% increase. The small and medium bridges show an increase in OMCCL from cooling method one to two/four of 778% and 806%, respectively. The percent increase is less profound from cooling method one to cooling method three with 205%, 183%, and 193% for the small, medium and large bridges respectively.

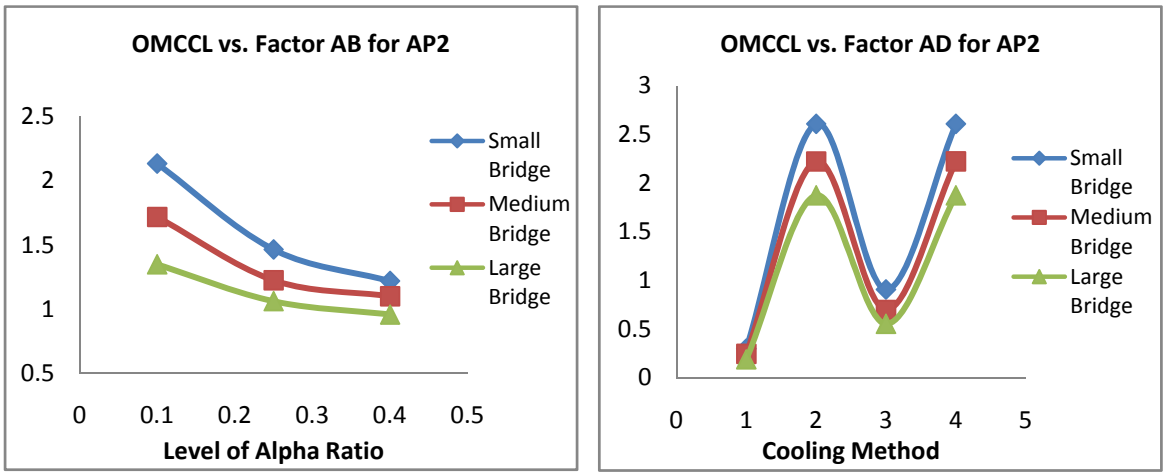

Figure 51 OMCCL vs. all factor interactions relative to bridge size for AP2.

The remaining factor interaction is also important to consider. Figure 52 shows the OMCCL versus the remaining factor interaction—*BD*. This interaction is not relative to bridge size.

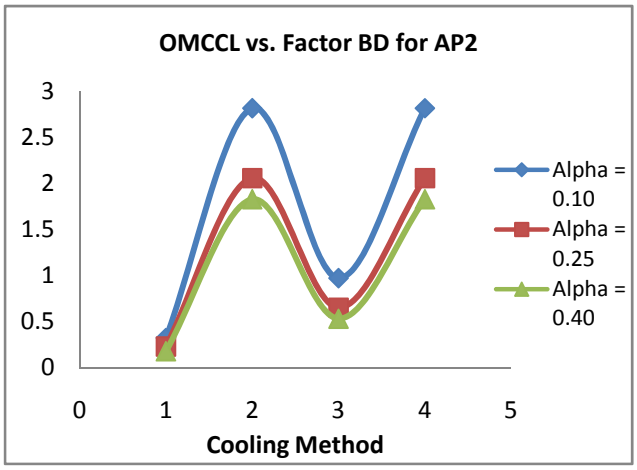

Figure 52 OMCCL vs. factor interaction *BD* for AP2.

For the factor interaction of alpha ratio versus cooling method, a similar trend is seen to previous factor interaction plots. The smallest alpha ratio yields the largest OMCCL values for all cooling methods and the largest bridge yields the smallest OMCCL values. This reinforces the use of lower alpha ratios when using AP2. The percent increase in OMCCL from cooling method one to two or four is 773%, 796%, and 927% for alpha ratios of 0.10, 0.25, and 0.40, respectively. It can be observed that the largest alpha ratio has the largest percent increase in the OMCCL relative to the cooling method so this alpha ratio has the most to gain from changing the cooling method.

5.4.2 Results: AP2: OMSR

The results for the OMSR in the second assembly procedure are discussed in this section. Some of the trends in the data resemble the trends for AP1, but in many cases they are different. The analysis had a percent contribution from the sum of the squares of the error of less than 1%. All values for OMSR for AP2 are given in Appendix B. Figure 53 shows the percent contribution of all factors and factor interactions of the ANOVA analysis on the OMSR in AP2.

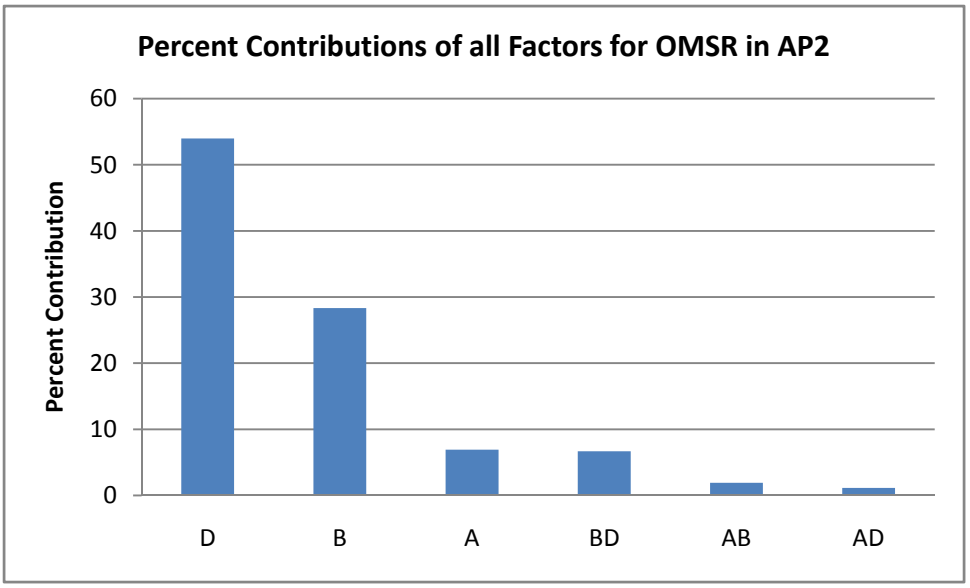

Figure 53 Percent contribution of all factors for OMSR in AP2.

As with the analysis of the OMCCL, the cooling method has the largest percent contribution of any factor with 54%. The percent contribution of the alpha ratio (factor *B*) and the bridge size (factor *A*) are 28% and 7% respectively suggesting that they affect the OMSR more than the OMCCL. The factor interaction between the alpha ratio and the cooling method (factor *BD*) is also important to consider with a percent contribution of 7%.

5.4.2.1 Individual Factors

The effect of individual factors on the OMSR for AP2 is discussed in this section. Many trends are similar to the analysis of the OMCCL. Figure 54 shows OMCCL versus all individual factors for AP2.

For the bridge size, it is clear that as bridge size increases the OMSR decreases. This is similar to the analysis of the OMCCL for AP2 but is directly opposite of the trend

observed in AP1. The percent decrease in OMSR for the medium and large bridge sizes relative to the small bridge size is 13% and 34%, respectively.

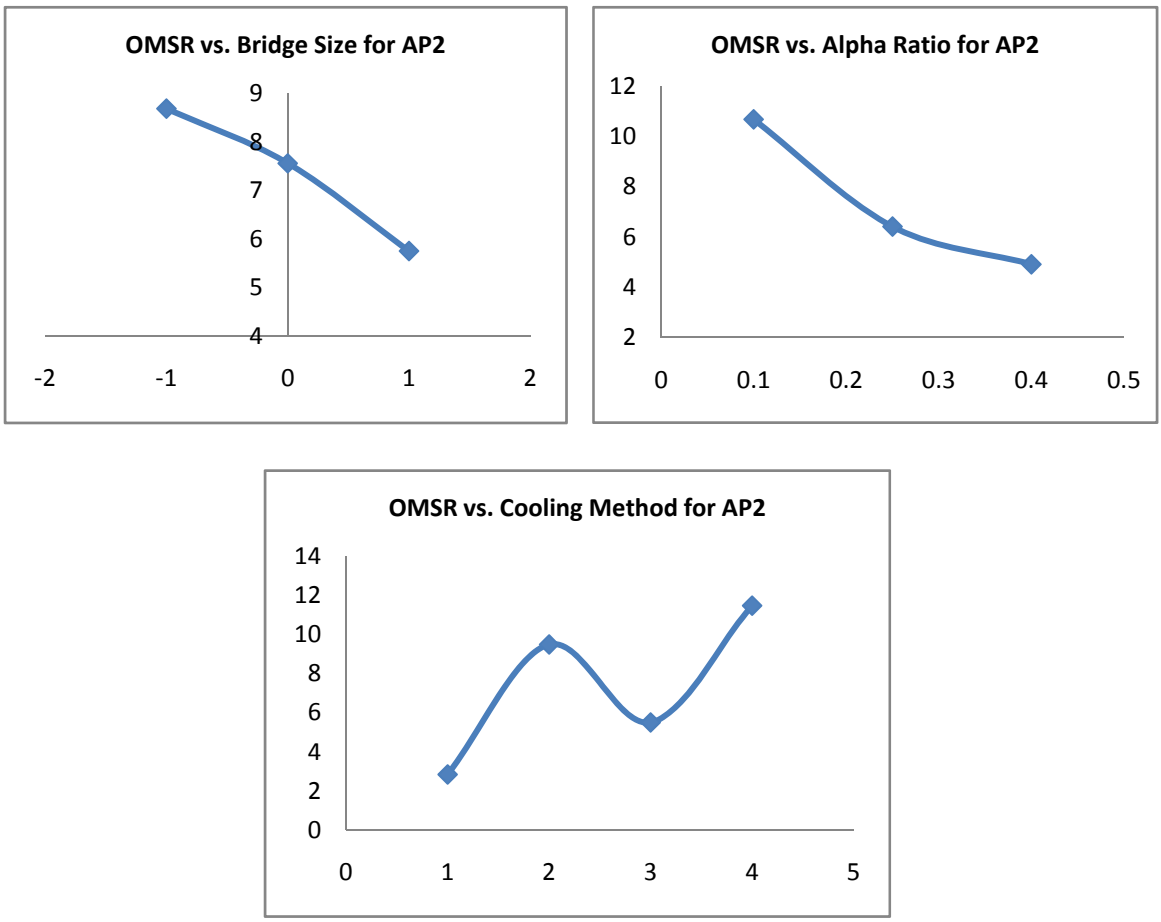

Figure 54 OMSR vs. individual factor interactions for AP2.

For the alpha ratio, the trend is exactly the same as the OMCCL for AP2 although the change is slightly more dramatic. Again, this is directly opposite of the trend observed in AP1 where the OMSR increased with an increase in the alpha ratio. The percent decrease in the OMSR for alpha values of 0.25 and 0.40 relative to an alpha value of 0.10 is 40% and 54%, respectively.

The cooling method shows similar trends to the OMCCL, with the exception that the OMSR for cooling method two is not the same for cooling method four. The percent

increase in OMSR for each cooling method relative to cooling method one is 234%, 93%, and 305%, respectively.

5.4.2.2 Factor Interactions

The factor interactions on the OMSR for AP2 will be discussed in this section. As in AP1, the main factor interactions involving the bridge size versus the alpha ratio (factor *AB*), and the bridge size versus the cooling method (factor *AD*) will be discussed first. Figure 55 shows the OMSR versus all possible factors relative to bridge size.

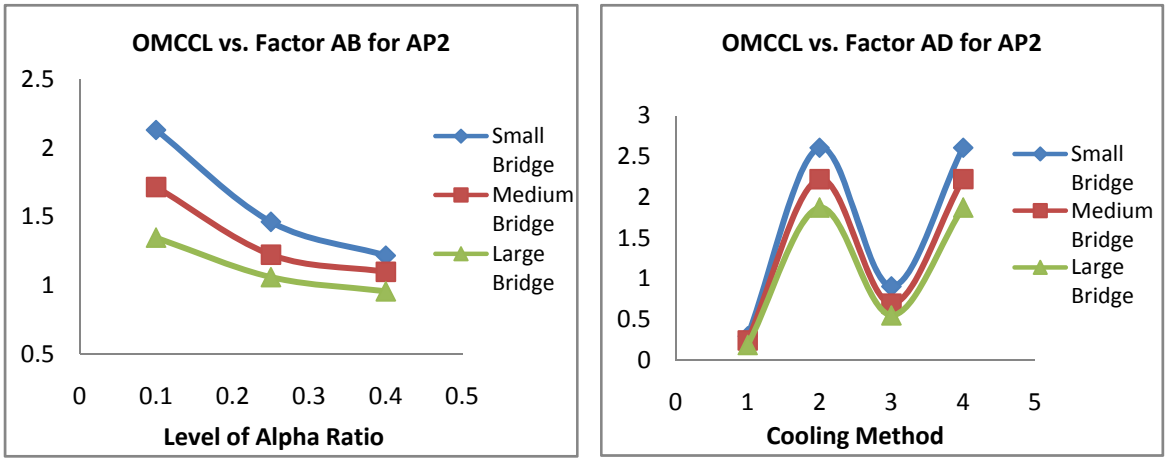

Figure 55 OMSR vs. factor interactions relative to bridge size for AP2.

For the interaction of alpha ratio relative to bridge size, it can be observed that the highest stress ratios come from the smallest bridge size which is consistent with the OMCCL. All bridge sizes show a decrease in the OMSR with an increase in the alpha ratio which is also consistent with the OMCCL. The small bridge geometry also yields the largest percent decrease in OMSR with an increase of the alpha ratio with a 58% decrease. The medium and large bridges show a percent decrease of 51% and 50%, respectively. The percent increase in the OMSR from the large bridge size to the small bridge size for an alpha value of 0.10 is 63%.

For the interaction of the cooling method relative to bridge size, the smallest bridge size has the highest OMSR values for every cooling method but not the largest percent increase relative to cooling method one. The percent increase in OMSR of the small, medium and large bridge from the first cooling method to the fourth cooling method are 285%, 308%, and 332%, respectively. This percent increase in OMSR for the second cooling method is 206%, 252% and 256% for the small, medium and large bridges, respectively.

The final factor interaction must also be considered. Figure 56 shows the OMSR versus the remaining factor interaction—*BD*. This interaction is not relative to bridge size.

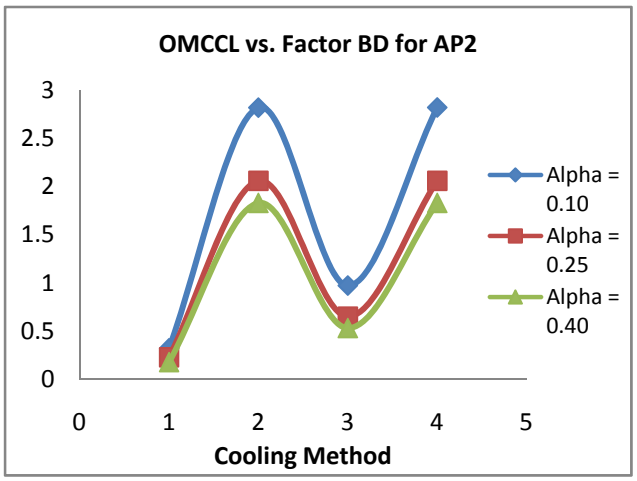

Figure 56 OMSR vs. factor interaction *BD* in AP2.

For the interaction between the alpha ratio and the cooling method, the smallest alpha ratio again has the highest OMSR values of any bridge which was the case with the OMCCL. The percent increase in the OMSR from cooling method one to cooling method four for alpha ratios of 0.10, 0.25, and 0.40 is 288%, 323% and 315%,

respectively. The percent increase in the OMSR from cooling method one to cooling method two for all alpha ratios is 257%, 210% and 216%, respectively.

5.4.3 Conclusions: AP2

For the second assembly procedure, some general conclusions and observations can be made.

1. With regards to bridge size, the mean OMCCL and OMSR decrease with an increase in bridge size. The percent decrease in OMCCL and OMSR from the smallest bridge size to the medium and large bridge size is 30% and 34%, respectively. The smallest bridge size has the largest OMCCL and OMSR values for every cooling method and every alpha ratio. The percent increase on OMCCL and OMSR from the large bridge to the small bridge can be as much as 58% and 62%, respectively for an alpha ratio of 0.10. This is in stark contrast to AP1 which showed the exact opposite trend.
2. With regards to the alpha ratio, the values of the OMCCL and OMSR decreased as the alpha ratio increased which is again in contrast to the data for AP1. The percent decrease in OMCCL (42%) and OMSR (58%) from the lowest alpha ratio to the highest was largest in the small bridge geometry and the smallest in the large bridge geometry. The smallest alpha ratio also produced the largest values in OMCCL and OMSR with respect to the cooling method with percent increases of 733% and 288%, respectively.
3. The cooling method produced similar trends to AP1 with the second and fourth cooling method producing the largest percent increases in the OMCCL and

OMSR. The percent increase from cooling method one to cooling method two can be as much as 927% for the OMCCL and 332% for the OMSR.

5.4.3.1 Recommendations: AP2

The best possible combination of bridge size, alpha ratio and cooling method for AP2 is a small bridge, an alpha ratio near 0.10, and the second cooling method. These factors consistently produced the highest OMCCL and OMSR values in the data collected.

It is particularly important to note the dramatic differences in the data for AP2 versus AP1. The small bridge size yields the highest OMCCL and OMSR values when AP2 is used, but the smallest values when AP1 is used. The other major difference to notice is the fact that the smallest alpha ratio produces the largest OMCCL and OMSR values for AP2, which was exactly the opposite case for AP1. These facts are of particular importance to bridge designers as they allow for additional insights into which assembly procedure to use relative to bridge size and alpha ratio.

5.5 Assembly Procedure 3

There are two main factors for the general factorial design for AP3—bridge size (factor *A*), and the cooling method (factor *D*). The set up of this sensitivity analysis is exactly the same as in AP2 with the exception that the alpha ratio is not a factor in the analysis. This is because the alpha ratio only changes the outer diameter of the hub—the inner diameter stays constant meaning the dimensions of the trunnion never change from one bridge to the next.

It was previously determined in Chapter 4 that neither step one nor step two of AP3 would yield critical stress ratios or critical crack lengths assuming that the girder dimensions are not overheated. Therefore, step three—dipping the trunnion in liquid nitrogen is assumed to be the critical step in the assembly procedure.

5.5.1 Results: AP3: OMCCL

The results for the OMCCL for AP3 are discussed in this section. The analysis had a percent contribution from the sum of the squares of the error of less than 5%. All values for OMCCL for AP3 are given in Appendix B. Figure 57 shows the percent contribution of all factors and factor interactions of the ANOVA analysis on the OMCCL in AP3.

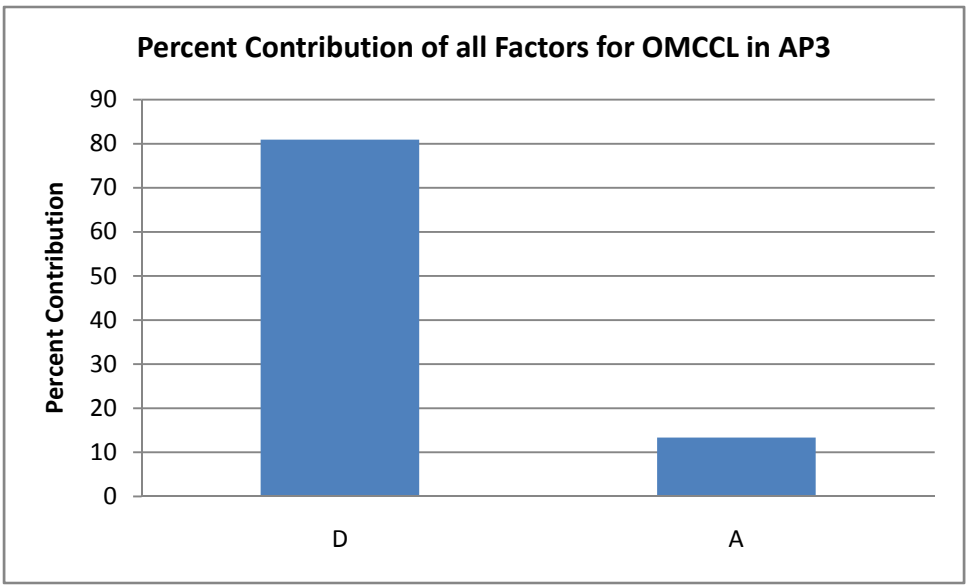

Figure 57 Percent contribution of all factors for OMCCL in AP3.

As with every other assembly procedure, the cooling method has the largest percent contribution to the overall ANOVA analysis with 81%. The bridge size also contributed 13% to the analysis.

5.5.1.1 Individual Factors

The effects of individual factors on the OMCCL for AP3 are discussed in this section. Most of the trends in the data are similar to other assembly procedures. Figure 58 shows OMCCL versus each individual factor for AP3.

For the bridge size, it can be observed that the OMCCL decreases with an increase in bridge size. The percent decrease from the small bridge to the medium and large bridges is 36% and 47%, respectively. This is in agreement with the previous analysis of AP2, but not with AP1 where it was seen that the medium bridge size had the largest OMCCL values.

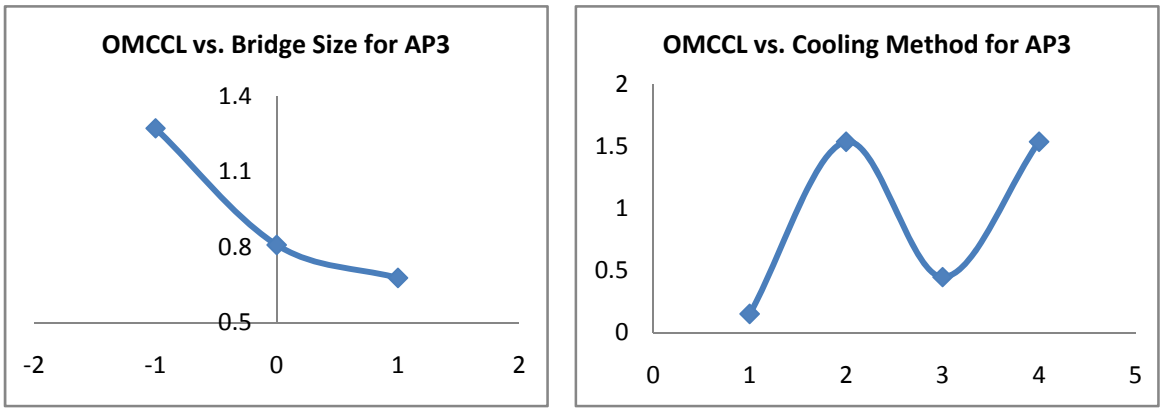

Figure 58 OMCCL vs. individual factor interactions for AP3.

For the cooling method factor, similar trends to AP1 and AP2 are seen in the OMCCL value. The percent increase in the OMCCL from the first cooling method to the second and fourth cooling method is 913%. The percent increase in the OMCCL relative to the third cooling method is 195%. The mean OMCCL value for the first cooling method is 0.1517 which is almost two times smaller than the mean OMCCL for AP2. This implies that the third step in AP2 may actually be the critical portion of the assembly procedure and not step one.

Although no formal factor interactions are present in this analysis, worthwhile observations can be still made for the OMCCL. Figure 59 shows the OMCCL versus the cooling method for all bridge sizes. It can be observed that the small bridge size has the highest OMCCL values for all cooling methods which is consistent with AP2 but not AP1. The percent increases in OMCCL for the small, medium and large bridge from cooling method one to cooling method two or four is 879%, 917% and 976%, respectively. This implies that although the largest bridge size has the lowest overall OMCCL value, it also has the most to gain from a change in the cooling methods.

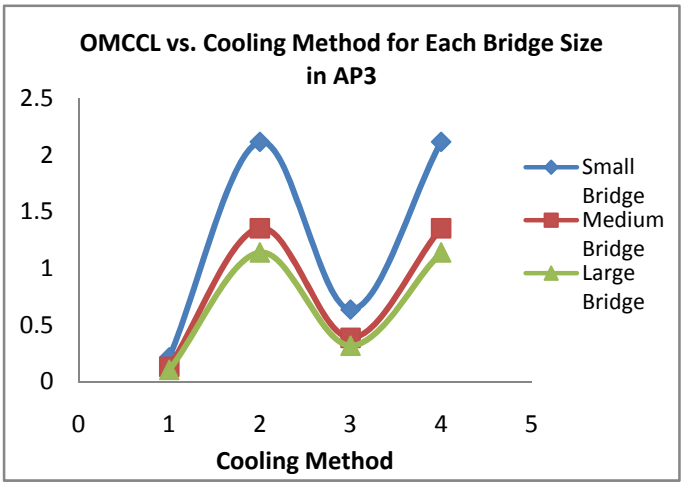

Figure 59 OMCCL vs. cooling method for all bridges in AP3.

5.5.2 Results: AP3: OMSR

The results for the OMSR for AP3 are discussed in this section. The analysis had a percent contribution from the sum of the squares of the error of less than 3%. All values for OMCCL for AP3 are given in Appendix B. Figure 60 shows the percent contribution of all factors in AP3. As with the OMCCL, the two level factor interaction is not included as an additional replicate would be required to adequately represent this factor.

As expected, the cooling method is again the most significant factor in the ANOVA analysis with a percent contribution of 91%. The bridge size is less significant with a percent contribution of 6%.

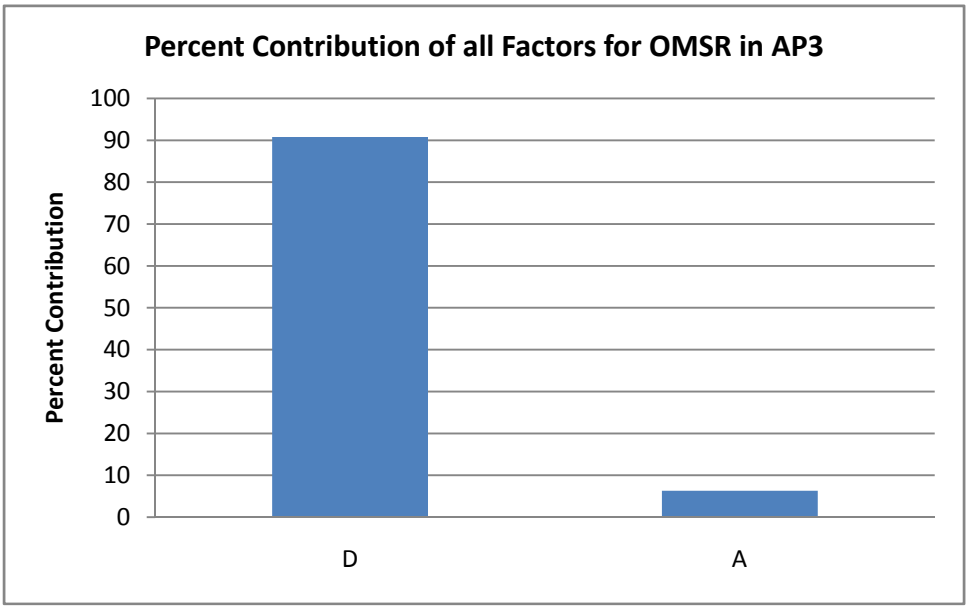

Figure 60 Percent contributions of all factors for OMSR in AP3.

5.5.2.1 Individual Factors

The effects of individual factors on the OMSR for AP3 are discussed in this section. Most of the trends in the data are similar to other assembly procedures. Figure 61 shows OMSR versus each individual factor for AP3.

Relative to the bridge size, the OMSR decreases with an increase in bridge size which is consistent with AP2 but not AP1. The largest OMSR value was observed in the large bridge size in AP1. The percent decrease in the OMSR from the small bridge size to the medium and large bridges is 16% and 25%, respectively.

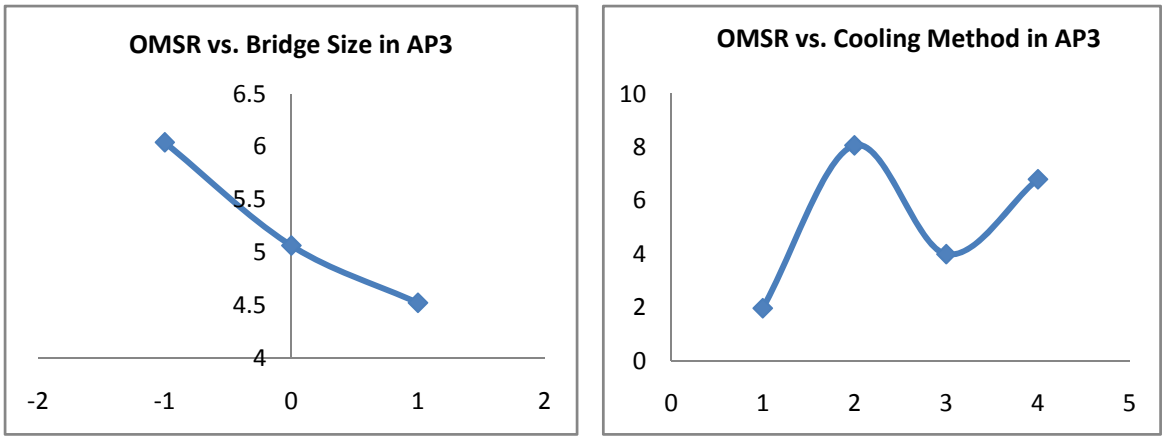

Figure 61 OMSR vs. individual factor interactions for AP3.

For the cooling method, the OMSR shows similar trends to other assembly procedures with the exception that cooling method four yields lower values than cooling method two. This is inconsistent with data from either AP1 or AP2 and could be somewhat of an anomaly. It is possible however, to obtain a lower stress ratio in this cooling process but the plausibility seems unlikely. The percent increase from the first cooling method to the second cooling method is 309%.

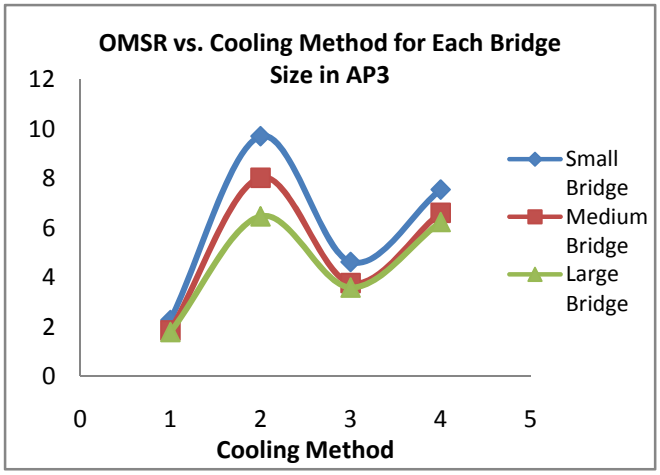

Figure 62 OMSR vs. cooling method for all bridges in AP3.

Figure 62 shows the OMSR versus the cooling method for all bridge sizes. Similar trends are seen to the general plot of the cooling method on the OMSR. The

small bridge size has the largest OMSR values for all cooling methods which is in agreement with the data for AP2 but not for AP1. The percent increase in OMSR from the first to the second cooling methods for the small, medium and large bridges is 326%, 333% and 261%, respectively.

5.5.3 Conclusions: AP3

For the third assembly procedure, some general conclusions and observations can be made.

1. With regards to bridge size, the OMCCL and OMSR decrease with an increase in bridge size which is consistent with AP2. The percent decrease in the OMCCL and OMSR from the small to the large bridge is 46% and 25%, respectively. The small bridge also has the highest OMCCL and OMSR values of any bridge. The percent increase in the OMCCL and OMSR between the large bridge and the small bridge can be as much as 103% and 50%, respectively.
2. The cooling method shows similar trends to AP2 with the exception that the fourth cooling method did not yield an OMSR value as high as cooling method two. This could be an anomaly in the data or the model, and is unlikely a realistic possibility.

5.5.3.1 Recommendations: AP3

A complete recommendation with regards to AP3 is more difficult to give simply on the basis that a considerable portion of the assembly procedure involves the heating of the girder. Variations in girder dimensions may cause larger stresses during the heating

process and a full sensitivity analysis on these parameters is necessary before a complete recommendation can be made.

Simply based on the analysis of this work, the best combination of bridge size and cooling method is the smallest bridge with the second cooling method. These factors consistently produced the highest OMCCL and OMSR values for AP3.

It should also be noted that cooling the trunnion in cooling method one actually produces a smaller OMCCL and OMSR value (0.1517, 1.973) than cooling the hub with this same cooling method in AP2 (0.2434, 2.839). This implies that the third step in AP2 is actually the most critical step, but this is not to say that failures in the hub could not take place. To test this theory, an experiment could be performed whereby the trunnion and hub from the same bridge size are dipped in a cooling medium (such as liquid nitrogen) and the OMCCL and OMSR are found for each component. If the OMCCL and OMSR are lower for the trunnion, then it can be assumed that step three is the critical step in AP2.

5.6 Final Recommendations

The choice of which assembly procedure to use is certainly a difficult decision to make as many other factors are important to consider in addition to the factors discussed in this work. Some of these factors include feasibility, cost, time, ease of implementation, and availability of resources. Certainly no company wants TH components to fail in any situation, but they also do not want the assembly process to take up an excessive amount of time, or cost dramatically more. AP3 is perhaps the best of all the methods with regards to minimizing the possibilities of failure via crack

propagation, but would also most likely be the most time consuming assembly procedure. In addition, if girder dimensions are radically different from one bridge to the next, it could be difficult to consistently generate enough clearance in the girder hole to allow for insertion of the hub. Further study of each girder dimension and optimal arrangement of the heating coils is necessary to fully understand the feasibility of assembly procedure three, as well as the exact time and cost needed to implement this method.

As previous studies and this study have shown, AP1 is perhaps the worst assembly procedure to use, although it is the most commonly used in practice. It consistently produces the smallest OMCCL and OMSR values for all bridges. One major insight of this work is that if the use of AP1 is absolutely necessary, a variation in the alpha ratio, or if possible, the bridge size (relative dimensions of the TH assembly) can yield higher OMCCL and OMSR values. This can help bridge designers implement the best alpha ratio if they know which assembly procedure is planned to be used. In practice, this dynamic is most likely just the opposite with the alpha ratio determined in an early stage of the design, and the assembly procedure chosen later. Nevertheless, it does provide valuable insight into the problem.

From the results of this work, and with additional considerations of time and cost, AP2 seems to be the best overall choice above all other assembly procedures. This method is relatively easy to implement and even if liquid nitrogen is used as a cooling medium, the OMCCL and OMSR values are consistently double the values seen in AP1. Also, the use of cooling method two for this assembly procedure would all but eliminate the likelihood for failure in AP2, and still be relatively easy to and cheap to implement.

As a reference, bridge designers should consider Table 5 which provides a means of comparison between bridge sizes, alpha ratios and the expected values of OMCCL and OMSR relative to these input conditions. For this table, AP3 is omitted as it cannot be reasonably determined at this stage that this assembly procedure is as viable as the others. Also, it is assumed in all cases that the second cooling method is used.

Table 5 Suggested use of AP1 and AP2 for all bridge sizes and alpha ratios.

Bridge Size	Alpha Ratio	AP1		Overall	AP2		Overall
		OMCCL	OMSR		OMCCL	OMSR	
Small	0.10	Poor	Good	Poor	Best	Best	Best
Small	0.25	Good	Poor		Good	Good	
Small	0.40	Best	Best		Poor	Poor	
Medium	0.10	Poor	Poor	Best	Best	Best	Good
Medium	0.25	Good	Good		Good	Good	
Medium	0.40	Best	Best		Poor	Poor	
Large	0.10	Poor	Poor	Good	Best	Best	Poor
Large	0.25	Good	Best		Good	Good	
Large	0.40	Best	Good		Poor	Poor	

REFERENCES

[1] G. Besterfield, A. K. Kaw and R. Crane, Parametric Finite Element Modeling and Full-Scale Testing of Trunnion-Hub-Girder Assemblies for Bascule Bridges, Mechanical Engineering Dept, University of South Florida, (2001).

[2] G. Besterfield, S. Nichani, A. K. Kaw, T. Eason, Full-Scale Testing of Procedure for Assembling Trunnion-Hub-Girder in Bascule Bridges, Journal of Bridge Engineering, ASCE, July/August (2003) 204-211.

[3] S. Nichani, Full Scale Testing of Trunnion-Hub-Girder Assembly of a Bascule Bridge, MS Thesis, Mechanical Engineering Dept, University of South Florida, (2001).

[4] C. Nguyen, A. K.Kaw, J. Paul, Sensitivity Analysis of Cooling Methods and Geometric Parameters in the Assembly Procedure of Bascule Bridge Fulcra, Journal of Strain Analysis 42 (2007) 337-349.

[5] C. Nguyen, A Design of Experiments Study of Procedure for Assembling Bascule Bridge Fulcrum, MS Thesis, Mechanical Engineering Dept, University of South Florida, 2006.

[6] P. Pedersen, On Shrink Fit Analysis and Design, Computational Mechanics 37 (2006) 121-130.

[7] C.E. Truman, J.D. Booker, Analysis of a shrink-fit failure on a gear hub/shaft assembly, Engineering Failure Analysis 14 (2007) 557-572.

[8] J. E. Shigley, and C. R.Mischke, Standard Handbook of Machine Design, (1986) (McGraw-Hill, New York).

[9] C. K. Chen, B. L. Kuo, Coupled Transient Thermoelastic Contact Problems for Axial Cracks in Hollow Cylinders, International Journal for Numerical Methods in Engineering 37 (1994) 2109-2123.

[10] H. F. Nied and F. Erdogan, Transient Thermal Stress Problem for a Circumferentially Cracked Hollow Cylinder, Journal of Thermal Stresses 6 (1983) 1-14.

[11] F. Delale and S. P. Kolluri, Fracture of Thick-Walled Cylinders Subjected to Transient Thermal Stresses, Journal of Thermal Stresses 8 (1985) 235-248.

[12] N. Noda and N. Sumi, Stress Intensity Factor for Transient Thermal Stress of a thin plate with a Griffith Crack, Journal of Thermal Stresses 8 (1985) 173-182.

[13] N. Noda, Y. Matsunaga and H. Nyuko, Stress Intensity Factor for Transient Thermal Stresses in an Infinite Elastic Body with an External Crack, Journal of Thermal Stresses 9 (1986) 119-131.

[14] R. Oliveira and X. R. Wu, Stress Intensity Factors for Axial Cracks in Hollow Cylinders Subjected to Thermal Shock, Engineering Fracture Mechanics, 27 (1987) 185-197.

[15] H. D. Greenberg and W. G. Clark Jr., A Fracture Mechanics Approach to the Development of Realistic Acceptance Standards for Heavy Walled Steel Castings, Metals Engineering Quarterly 9 (August 1969) 30-39.

[16] M. T. Denninger, Design Tools for Trunnion-Hub Assemblies for Bascule Bridges, MS Thesis, Mechanical Engineering Dept, University of South Florida (2000).

[17] B. Ratnam, Parametric Finite Element Modeling of Trunnion-Hub-Girder Assemblies for Bascule Bridges, MS Thesis, Mechanical Engineering Dept, University of South Florida, (2000).

[18] M. Berlin, Innovative Procedure to Install a Trunnion-Hub Assembly in a Bascule Bridge Girder, MS Thesis, Mechanical Engineering Dept, University of South Florida, (2004).

[19] N. O. Collier, Benefit of Staged Cooling in Shrink-Fitted Composite Cylinders, MS Thesis, Mechanical Engineering Dept, University of South Florida, (2004).

[20] J. Paul, Sensitivity Analysis of Design Parameter for Trunnion-Hub Assemblies of Bascule Bridges, MS Thesis, Mechanical Engineering Dept, University of South Florida, (2005).

[21] ANSYS release 10 documentation, 2006 (ANSYS, Inc., Canonburg, Pennsylvania).

[22] M. Berlin, Innovative Procedure to Install a Trunnion-Hub Assembly in a Bascule Bridge Girder, MS Thesis, Mechanical Engineering Dept, University of South Florida, (2004).

[23] S. Sen, B. Aksakal, Stress Analysis of Interference Fitted Shaft-hub System Under Transient Heat Transfer Conditions, Materials and Design 25 (2004) 407-417.

[24] A. Ozel, S. Temiz, M. D. Aydin, S. Sen, Stress Analysis of Shrink-Fitted Joints for Various fit forms via Finite Element Method, Materials and Design 26 (2005) 281-289.

[25] H. Y. Kim, C. Kim, W. B. Bae, Development of an Optimization Technique of a Warm Shrink Fitting Process for an Automotive Transmission Parts, International Journal of Automotive Technology 7 (2006) 847-852.

[26] M. F. Kanninen, C. H. Popelar, Advanced Fracture Mechanics, 1985 (Oxford University Press, Oxford).

[27] J. Chen, B. Young, B. Uy, Behavior of High Strength Structural Steel at Elevated Temperature, Journal of Structural Engineering, Vol. 132, No.12, 1948 (2006)

[28] D.C. Montgomery, Design and Analysis of Experiments, 2005 (John Wiley & Sons, Inc., Hoboken).

APPENDICES

Appendix A: Radial Interference Calculations

The radial interference calculations for AP2 and AP3 are given in this section. For radial interference calculations for AP1, refer to the work of Nguyen (2006). Each of these calculations is based on standard FN2 and FN3 fits for compound cylinders. These fits are based on the principle that there are upper and lower limits of which the diameter of the cylinder will vary. This limit L is given by

$$L = CD^{1/3}$$

where C is the coefficient based on the type of fit, and D is the nominal diameter.

Table 6 Radial interference calculations for AP2 and AP3.

	17th St.		*Christa MacAuliffe*		*Hallandale*	
Diameter	Inner	Outer	Inner	Outer	Inner	Outer
Hub	12.944	$17.76^{+0.0085785}_{+0.0070888}$	18	$32^{+0.0104387}_{+0.0086259}$	26	$35^{+0.0107553}_{+0.0088875}$
Girder	$17.76^{+0.0023664}_{+0.0000000}$	N/A	$32^{+0.0028795}_{+0.0000000}$	N/A	$35^{+0.0029669}_{+0.0000000}$	35
Radial Interference	0.0023612		0.0028732		0.0029603	
	0.0042892		0.0052194		0.0053777	

Appendix B: Results for All Trials

Table 7 Results of all factors and runs for AP1.

	Factors				*OMCCL*	*OMSR*
Run#	*A*	*B*	*C*	*D*		
1	Small	0.10	Low	1	0.171378	1.96821
2	Small	0.10	Low	2	0.656736	2.36279
3	Small	0.10	Low	3	0.368256	3.23675
4	Small	0.10	Low	4	0.632355	3.49085
5	Small	0.10	High	1	0.125617	1.53603
6	Small	0.10	High	2	0.343989	1.71520
7	Small	0.10	High	3	0.224895	2.42612
8	Small	0.10	High	4	0.349761	2.21680
9	Small	0.25	Low	1	0.147644	1.15514
10	Small	0.25	Low	2	0.632389	2.22346
11	Small	0.25	Low	3	0.381942	2.53480
12	Small	0.25	Low	4	0.686901	4.17824
13	Small	0.25	High	1	0.123034	1.22568
14	Small	0.25	High	2	0.511706	2.29657
15	Small	0.25	High	3	0.286359	2.59367
16	Small	0.25	High	4	0.51169	2.66640
17	Small	0.40	Low	1	0.140202	1.08220
18	Small	0.40	Low	2	1.01085	3.36496
19	Small	0.40	Low	3	0.393446	5.59170
20	Small	0.40	Low	4	1.01090	3.72024
21	Small	0.40	High	1	0.123927	1.12478
22	Small	0.40	High	2	0.557521	2.82585
23	Small	0.40	High	3	0.320685	2.48702
24	Small	0.40	High	4	0.557501	2.80600
25	Medium	0.10	Low	1	0.140825	1.82154
26	Medium	0.10	Low	2	0.740934	2.14792
27	Medium	0.10	Low	3	0.345482	3.06595
28	Medium	0.10	Low	4	0.740984	3.67050
29	Medium	0.10	High	1	0.113335	1.51778
30	Medium	0.10	High	2	0.426576	1.65131
31	Medium	0.10	High	3	0.244235	2.28825
32	Medium	0.10	High	4	0.44161	2.44268
33	Medium	0.25	Low	1	0.131905	1.76694
34	Medium	0.25	Low	2	0.934957	2.02025
35	Medium	0.25	Low	3	0.362139	3.28968
36	Medium	0.25	Low	4	0.934954	4.48894
37	Medium	0.25	High	1	0.115007	1.60484
38	Medium	0.25	High	2	0.571586	2.29657
39	Medium	0.25	High	3	0.287004	2.64410
40	Medium	0.25	High	4	0.57159	2.96925
41	Medium	0.40	Low	1	0.131862	1.75424
42	Medium	0.40	Low	2	0.99418	2.03646
43	Medium	0.40	Low	3	0.385054	3.38554
44	Medium	0.40	Low	4	0.994187	4.65406

Appendix B: (Continued)

Table 7 (Continued)

45	Medium	0.40	High	1	0.120026	1.66659
46	Medium	0.40	High	2	0.598974	2.82585
47	Medium	0.40	High	3	0.315257	2.69271
48	Medium	0.40	High	4	0.598964	3.11543
49	Large	0.10	Low	1	0.107727	1.94040
50	Large	0.10	Low	2	0.725257	2.38527
51	Large	0.10	Low	3	0.289819	3.35301
52	Large	0.10	Low	4	0.725287	4.54059
53	Large	0.10	High	1	0.0925162	1.67786
54	Large	0.10	High	2	0.489504	1.89676
55	Large	0.10	High	3	0.226509	2.66254
56	Large	0.10	High	4	0.489509	3.17595
57	Large	0.25	Low	1	0.100868	2.12261
58	Large	0.25	Low	2	0.836064	3.78779
59	Large	0.25	Low	3	0.292033	3.85162
60	Large	0.25	Low	4	0.836066	5.26670
61	Large	0.25	High	1	0.0916231	1.95628
62	Large	0.25	High	2	0.589695	2.76539
63	Large	0.25	High	3	0.248143	3.04198
64	Large	0.25	High	4	0.589698	3.62130
65	Large	0.40	Low	1	0.104841	1.53422
66	Large	0.40	Low	2	0.871811	3.77447
67	Large	0.40	Low	3	0.311159	3.30065
68	Large	0.40	Low	4	0.871845	5.26445
69	Large	0.40	High	1	0.0980649	1.56237
70	Large	0.40	High	2	0.599459	3.49705
71	Large	0.40	High	3	0.277051	3.04055
72	Large	0.40	High	4	0.599454	3.74265

Table 8 Results of all factors and runs for AP2.

	Factors			*OMCCL*	*OMSR*
Run #	*A*	*B*	*D*		
1	Small	0.10	1	0.41311	5.75306
2	Small	0.10	2	3.42358	17.0348
3	Small	0.10	3	1.27217	9.9372
4	Small	0.10	4	3.42358	19.9225
5	Small	0.25	1	0.281708	2.87981
6	Small	0.25	2	2.36862	7.80621
7	Small	0.25	3	0.834786	6.03943
8	Small	0.25	4	2.36860	12.7695
9	Small	0.40	1	0.196217	2.00563
10	Small	0.40	2	2.03216	7.79456
11	Small	0.40	3	0.610713	3.98946
12	Small	0.40	4	2.03217	8.2915
13	Medium	0.10	1	0.321192	3.7128
14	Medium	0.10	2	2.79805	15.9036

Appendix B: (Continued)

Table 8 (Continued)

15	Medium	0.10	3	0.948367	7.63227
16	Medium	0.10	4	2.80035	15.9218
17	Medium	0.25	1	0.229681	2.70923
18	Medium	0.25	2	2.02932	8.62792
19	Medium	0.25	3	0.608217	4.86749
20	Medium	0.25	4	2.02932	10.4779
21	Medium	0.40	1	0.184993	2.15097
22	Medium	0.40	2	1.84051	5.70655
23	Medium	0.40	3	0.532086	4.37467
24	Medium	0.40	4	1.84051	8.62993
25	Large	0.10	1	0.233909	2.91698
26	Large	0.10	2	2.23034	11.3833
27	Large	0.10	3	0.695341	5.78895
28	Large	0.10	4	2.23033	12.2212
29	Large	0.25	1	0.177095	1.87384
30	Large	0.25	2	1.77761	6.70802
31	Large	0.25	3	0.510143	3.81263
32	Large	0.25	4	1.77762	8.3658
33	Large	0.40	1	0.152358	1.54567
34	Large	0.40	2	1.61227	4.52628
35	Large	0.40	3	0.450255	3.09894
36	Large	0.40	4	1.61227	6.79578

Table 9 Results of all factors and runs for AP3.

	Factor		*OMCCL*	*OMSR*
Run #	*A*	*D*		
1	Small	1	0.215986	2.27541
2	Small	2	2.11604	9.71018
3	Small	3	0.637384	4.62549
4	Small	4	2.11604	7.55139
5	Medium	1	0.133206	1.85298
6	Medium	2	1.35498	8.03019
7	Medium	3	0.388873	3.77011
8	Medium	4	1.35498	6.61096
9	Large	1	0.105995	1.78998
10	Large	2	1.14116	6.47223
11	Large	3	0.319316	3.59102
12	Large	4	1.14116	6.24218